BEILSTEIN JOURNAL OF NANOTECHNOLOGY

Nanostructures for sensors, electronics, energy and environment

Edited by Nunzio Motta

Imprint

Beilstein Journal of Nanotechnology
www.bjnano.org
ISSN 2190-4286
Email: journals-support@beilstein-institut.de

The *Beilstein Journal of Nanotechnology* is published by the Beilstein-Institut zur Förderung der Chemischen Wissenschaften.

Beilstein-Institut zur Förderung der
Chemischen Wissenschaften
Trakehner Straße 7–9
60487 Frankfurt am Main
Germany
www.beilstein-institut.de

Beilstein Journal
of Nanotechnology

Nanostructures for sensors, electronics, energy and environment

Nunzio Motta

Editorial

Address:
School of Chemistry, Physics & Mechanical Engineering, Queensland University of Technology, Brisbane, 4001, Australia

Email:
Nunzio Motta - n.motta@qut.edu.au

Beilstein J. Nanotechnol. **2012,** *3,* 351–352.
doi:10.3762/bjnano.3.40

Received: 03 April 2012
Accepted: 27 April 2012
Published: 02 May 2012

This article is part of the Thematic Series "Nanostructures for sensors, electronics, energy and environment".

Editor-in-Chief: T. Schimmel

The areas of nanoscale science and technology are rapidly emerging, with a focus on the design, fabrication, and characterization of functional objects on the scale of several nanometers. The implications of the new advances in this field are expected to reach far and wide, spanning a variety of scientific and engineering disciplines. Nanoscale science is growing evermore important on a global scale and is widely seen as playing an integral part in the growth of future world economies.

We are all committed to leaving behind a better world for future generations, and nanotechnology can definitely help to improve our environment in several ways. The daunting energy crisis we are facing could be solved not only by new and improved ways of getting energy directly from the sun, but also by saving power thanks to advancements in electronics and sensors.

New, cheap dye-sensitized and polymer solar cells hold the promise of environmentally friendly and simple production methods, along with mechanical flexibility and low weight, matching the conditions for a widespread deployment of this technology. Their often-criticized scarce efficiency is rapidly growing, thanks to the discovery of new dyes and polymers, which are the fruit of teamwork between chemists, physicists and engineers, all working at the nanoscale.

Cheap sensors based on nanomaterials can make a fundamental contribution to the reduction of greenhouse gas emissions, allowing the creation of large sensor networks to monitor countries and cities, improving our quality of life. Nanowires and nano-platelets of metal oxides are at the forefront of the research to improve sensitivity and reduce the power consumption in gas sensors.

Nanoelectronics is the next step in the electronic roadmap, with many devices currently in production already containing components smaller than 100 nm. Molecules [1,2] and conducting polymers [3] are at the forefront of this research with the goal of reducing component size through the use of cheap and environmentally friendly production methods. This, and the coming steps that will eventually bring the individual circuit element close to the ultimate limit of the atomic level, are expected to deliver better devices with reduced power consumption. In this respect the present Thematic Series is an interesting follow-up to the series “Transport through molecular junctions” published in the Beilstein Journal of Nanotechnology in 2011 [1].

Many of these advances have been possible thanks to the discovery of new aggregation forms of materials at the nanoscale, such as fullerenes, nanotubes, graphene [4] and other carbon structures, or new organic–inorganic mixtures with unexpected properties, discussed also in the series “Organic–inorganic nanosystems” edited by Paul Ziemann [5].

Last but not least, we need to acknowledge that the ability to study these incredible aggregation forms of materials with atomic resolution is mainly due to the developments in scanning probe microscopy [6,7] that have occurred over the last 20 years. The Beilstein Journal of Nanotechnology recently hosted the series “Scanning probe microscopy and related methods” edited by Ernst Meyer [6] and “Noncontact atomic force microscopy” edited by Udo Schwarz [7] to which the interested reader is directed for more information.

Science always holds surprises, and I am delighted to present this Thematic Series, giving a quick glance at the science and application of nanostructures.

Nunzio Motta

Brisbane, April 2012

References

1. van Ruitenbeek, J. M. *Beilstein J. Nanotechnol.* **2011,** *2,* 691–692. doi:10.3762/bjnano.2.74
2. Glatzel, T.; Zimmerli, L.; Kawai, S.; Meyer, E.; Fendt, L.-A.; Diederich, F. *Beilstein J. Nanotechnol.* **2011,** *2,* 34–39. doi:10.3762/bjnano.2.4
3. Mena-Osteritz, E.; Urdanpilleta, M.; El-Hosseiny, E.; Koslowski, B.; Ziemann, P.; Bäuerle, P. *Beilstein J. Nanotechnol.* **2011,** *2,* 802–808. doi:10.3762/bjnano.2.88
4. Held, C.; Seyller, T.; Bennewitz, R. *Beilstein J. Nanotechnol.* **2012,** *3,* 179–185. doi:10.3762/bjnano.3.19
5. Ziemann, P. *Beilstein J. Nanotechnol.* **2011,** *2,* 363–364. doi:10.3762/bjnano.2.41
6. Meyer, E. *Beilstein J. Nanotechnol.* **2010,** *1,* 155–157. doi:10.3762/bjnano.1.18
7. Schwarz, U. D. *Beilstein J. Nanotechnol.* **2012,** *3,* 172–173. doi:10.3762/bjnano.3.17

License and Terms

Beilstein Journal
of Nanotechnology

Ultraviolet photodetection of flexible ZnO nanowire sheets in polydimethylsiloxane polymer

Jinzhang Liu*[1], Nunzio Motta[1] and Soonil Lee[2]

Letter

Address:
[1]School of Chemistry, Physics & Mechanical Engineering, Queensland University of Technology, Brisbane, 4001, Australia and
[2]Division of Energy Systems Research, Ajou University, Suwon, 443-749, Republic of Korea

Email:
Jinzhang Liu* - jinzhang.liu@qut.edu.au

* Corresponding author

Keywords:
permeable polymer; photoresponse; polydimethylsiloxane; UV photodetection; ZnO nanowires

Beilstein J. Nanotechnol. **2012,** *3,* 353–359.
doi:10.3762/bjnano.3.41

Received: 17 January 2012
Accepted: 28 March 2012
Published: 02 May 2012

This article is part of the Thematic Series "Nanostructures for sensors, electronics, energy and environment".

Associate Editor: P. Ziemann

Abstract

ZnO nanowires are normally exposed to an oxygen atmosphere to achieve high performance in UV photodetection. In this work we present results on a UV photodetector fabricated using a flexible ZnO nanowire sheet embedded in polydimethylsiloxane (PDMS), a gas-permeable polymer, showing reproducible UV photoresponse and enhanced photoconduction. PDMS coating results in a reduced response speed compared to that of a ZnO nanowire film in air. The rising speed is slightly reduced, while the decay time is prolonged by about a factor of four. We conclude that oxygen molecules diffusing in PDMS are responsible for the UV photoresponse.

Introduction

ZnO is a direct wide band gap semiconductor with a 3.37 eV gap and a high exciton binding energy of 60 meV at room temperature, which is promising for optoelectronic applications, including light-emitting diodes, laser diodes, and photodetectors for the ultraviolet (UV) spectral range [1,2]. ZnO nanostructures are particularly interesting as they bear superior properties compared to the bulk crystal. UV-light detection is one of the major applications of ZnO, and various UV photodetectors based on ZnO films or nanocrystals have been reported. It has been demonstrated that ZnO nanowires have high internal photoconduction gain and much stronger responsivity under UV-light illumination compared to the bulk film [3]. The UV photoresponse mechanism of ZnO nanowires is dominated by the adsorption and desorption of oxygen molecules [4]. In vacuum, ZnO nanowires show a prolonged UV photoresponse time and lowered responsivity [5]. So far, many UV photosensors have been made from ZnO one-dimensional nanostructures with various configurations, for sensing elements, such as single-nanowire devices [6], nanowire bridges [7], nanobelt network films [8], vertical nanowire arrays [9], and flexible nanowire sheets [10]. These nanostructures are normally exposed to air for measurement, neglecting the possible surface contamination caused by absorption of other molecules from the ambient atmosphere, which can degrade the UV-sensing performance of ZnO. For example, it has been demonstrated that the UV photoconduction of ZnO nanowires is degraded by the adsorption of water molecules in humid air [5,11]. Water molecules together with CO_2 in a moist atmosphere bring about a slow chemical reaction with ZnO to form amorphous $Zn(CO)_3$, which roughens the surface of the nanowires [12]. Therefore, for practical application the device encapsulation is essential to ensure a clean oxygen atmosphere around the nanowires. In this work we investigate the performance of polymer-embedded ZnO nanowires for UV photodetection, to avoid the need to use a gas cavity to load the nanowires, simplifying the device fabrication.

Recent experiments have demonstrated that coating ZnO nanobelts with UV-sensitive polymers enhances the UV photoconduction [13,14]. A thin layer (<100 nm) of such a polymer over ZnO nanocrystals produces excited states upon UV illumination. The excited states of the polymer molecules act as transition states facilitating electron hopping from the valence band of ZnO into the conduction band. However, the coating of such a polymer over ZnO nanowires must not be too thick because it would block the UV light. Moreover, carbon-based polymers undergo oxidation with ageing, and the degradation could be expedited by the absorption of UV light.

In this paper, we report results of experiments on UV photodetectors based on a thin sheet of ZnO nanowires embedded in polydimethylsiloxane (PDMS), which is an optically clear, UV-transparent silicone polymer that has been used in the fabrication of contact lenses, microfluidic devices, and stretchable displays. Due to its excellent gas permeability this polymer has been applied as a membrane for gas separation [15]. In our work, we combine free-standing thin-sheets of ZnO nanowires with the elastic material PDMS, suitable for developing bendable devices, which are of interest in current research.

Results and Discussion

ZnO nanowires were synthesized on a large scale by a modified carbothermal reduction method. Vaporized zinc and oxygen react at atmospheric pressure and result in a cotton-like product consisting of ZnO nanowires. The nanowires were processed into free-standing thin sheets, which can be cut by a blade into any shape [16]. The optical photograph in Figure 1a shows a strap-shaped nanowire sheet held by a tweezer. Scanning electron microscopy (SEM) observation reveals that these nanowires interdigitate to form a felt-like film (Figure 1b). Transmission electron microscopy (TEM) images of the nanowires are shown in Figure 1c and Figure 1d. The high-resolution TEM image in Figure 1d reveals that the nanowires grow along the [1] direction, as the distance between the (0001) planes is 0.52 nm. The nanowires are 20–60 nm in thickness and tens of microns in length. The high surface-to-volume ratio ensures a large surface adsorbance of gaseous molecules.

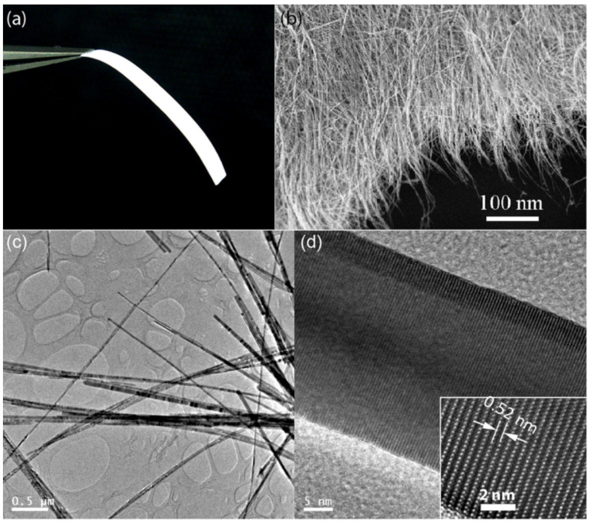

Figure 1: (a) An optical photograph of a strap-shaped ZnO nanowire film; (b) SEM image of the nanowire film; (c,d) TEM images of the nanowires.

Figure 2 shows the room-temperature photoluminescence (PL) spectrum of the ZnO nanowires, at the excitation wavelength of 325 nm. The insert is a PL excitation (PLE) spectrum taken for the emission at 570 nm. The PLE spectrum indicates that these nanowires absorb UV light with a wavelength below 378 nm, whereas they are transparent to visible light. In the PL spectrum the sharp peak at 379 nm is ascribed to the near-band-edge

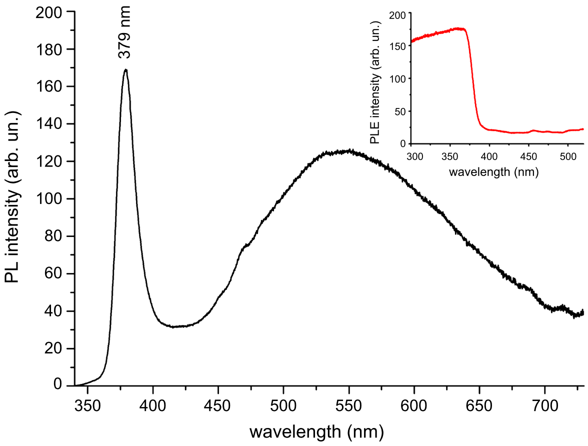

Figure 2: Room-temperature PL spectrum of the ZnO nanowire film. The insert is a PLE spectrum.

emission of ZnO. The broad emission band in the visible range is related to some crystal defects as luminescent centres. In our method, the nanowires were grown quickly by vapour-phase reaction at low temperature, below 200 °C, and crystal defects are expected. Oxygen vacancies and antisite oxygen give contributions to the green PL emission around 520 nm; zinc vacancies and interstitial oxygen contribute to the blue PL emission (450–470 nm) [17].

We made devices based on the strap-shaped nanowire sheets (width 2 mm). To make electrode contacts, silver paste made by mixing Ag nanopowder and the viscous PDMS liquid was painted onto a nanowire film strap at two ends, leaving a 10 mm gap between the two electrodes. The whole device, with a Ag–ZnO–Ag structure, was embedded in PDMS for measurement. The PDMS liquid wets the ZnO nanowires well, such that after curing the interspaces between nanowires were filled with PDMS polymer, making the paper-like nanowire sheet more translucent. For comparison, we made two devices without embedding in PDMS. For these two devices we deposited metal electrodes (Ti or Ag) onto the strap-shaped ZnO nanowire films (2 mm width) by e-beam evaporation through a shadow mask, in order to rule out the influence of PDMS on the UV-detection performance. The gap between two opposite electrodes is 10 mm, which is the same as that of the device in PDMS. If Ag–PDMS paste were applied onto the ZnO nanowire film, the liquid PDMS would slowly spread out of the agglomeration of Ag nanoparticles and infiltrate the nanowire film due to capillarity. Figure 3a shows the current–voltage (*I–V*) curves of the device in PDMS, measured under UV-light illumination (312 nm, 30 mW·cm^{-2}) and in the dark. The *I–V* curves of two other devices measured in air are plotted in Figure 3b. ZnO is naturally n-type with an electron affinity of 4.35 eV; the work functions of Ag and Ti are 4.26 eV and 4.33 eV, respectively. Under UV illumination Ti shows good ohmic contact on ZnO due to the extremely low barrier at the Ti/ZnO junction. The vacuum deposited Ag also shows nearly ohmic contact on ZnO (Figure 3b). However, for the contact of Ag paste on ZnO, the *I–V* curves measured under UV illumination and in the dark show rectifying features. Presumably, the Ag nanoparticles that we used to make the Ag–PDMS paste were spontaneously oxidized due to ageing. The surface Ag_2O layer, a narrow bandgap semiconductor, added an extra barrier for electrons flowing between Ag nanoparticles and ZnO nanowires, resulting in the nonlinear *I–V* curves in Figure 3a. The *I–V* curve of the device in PDMS measured in the dark, plotted in the insert in Figure 3a, shows that at a forward bias of 8 V the current is only 0.11 µA, whereas under UV light illumination the current reaches 405 µA at 8 V, ~3650 times larger. However, for the two devices measured in air, the current values at 8 V are around 85 µA for the device with Ti electrodes, and 78 µA for the device with Ag electrodes. Previously, we studied the UV photoconduction of ZnO nanowire films with different PL properties, i.e., defect contents. The UV photocurrent of those ZnO nanowire films (2 mm wide and 10 mm long) with vacuum deposited Ag electrodes was in the range of 13–90 µA at 8 V when measured in air [10]. In this work, the UV photocurrent of the device with Ag paste electrodes, embedded in PDMS, exceeds 400 µA at 8 V. Even at a reverse bias of −8 V, the current is 160 µA, much higher than that of the device without PDMS. In the dark, the current values of the device in PDMS are 110 nA at 8 V and 18 nA at −8 V. However, the dark current of the ZnO nanowire films exposed to air is extremely low, about 0.1 nA at 8 V (see the insert in Figure 3b), indicating considerable adsorbance of oxygen on the nanowire surfaces. Hence, both the UV photoconduction and dark

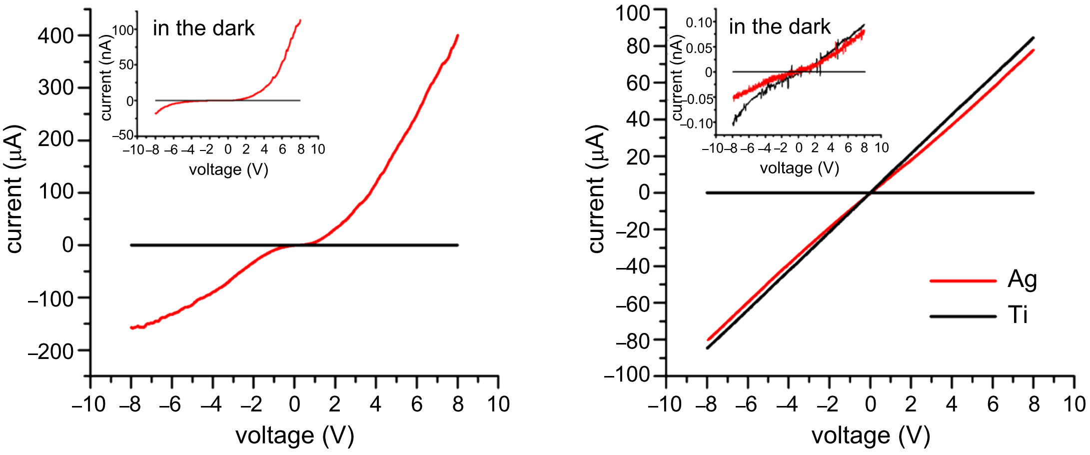

Figure 3: *I–V* curves of ZnO nanowire films under UV illumination and in the dark. (a) The device in PDMS with Ag–PDMS paste electrodes; (b) two devices in air, with vacuum-deposited metal electrodes (Ti or Ag).

conduction of the nanowire film can be enhanced by PDMS coating. The responsivity of the device, defined as the photocurrent per unit of incident optical power, is determined by the UV photoconductivity of the ZnO nanowires. From the *I*–*V* curves we can deduce that the PDMS coating over ZnO nanowires results in an approximately fivefold enhancement in the responsivity of the device.

Figure 4 shows the UV-photoresponse characteristics of two devices based on ZnO-nanowire sheets with the same dimensions. The device with vacuum-deposited Ti electrodes was exposed to air, and the other one with Ag paste electrodes was embedded in PDMS. Both were measured at 8 V with the UV light switched on and off periodically. Figure 4a and Figure 4b show the UV photoresponse characteristics of the devices in air and in PDMS, respectively. The current–time curves depicting the UV photoresponse are further plotted in Figure 4c and Figure 4d on a logarithmic scale. The maximum photocurrent of the device in air is 86 μA, while that of the device in PDMS reaches 476 μA. The PDMS coating over ZnO nanowires leads to an enhancement of the UV photosensitivity and prolongs the decay time. The rise of the photocurrent and the dark current decay of the two devices are compared in Figure 4e and Figure 4f, respectively, with the current normalized to the maximum. Upon the switching on of the UV light, the current through the nanowire film in PDMS rises fast with a speed equivalent to that in air. Within one second the current reaches half of the maximum seen upon UV illumination. We define the

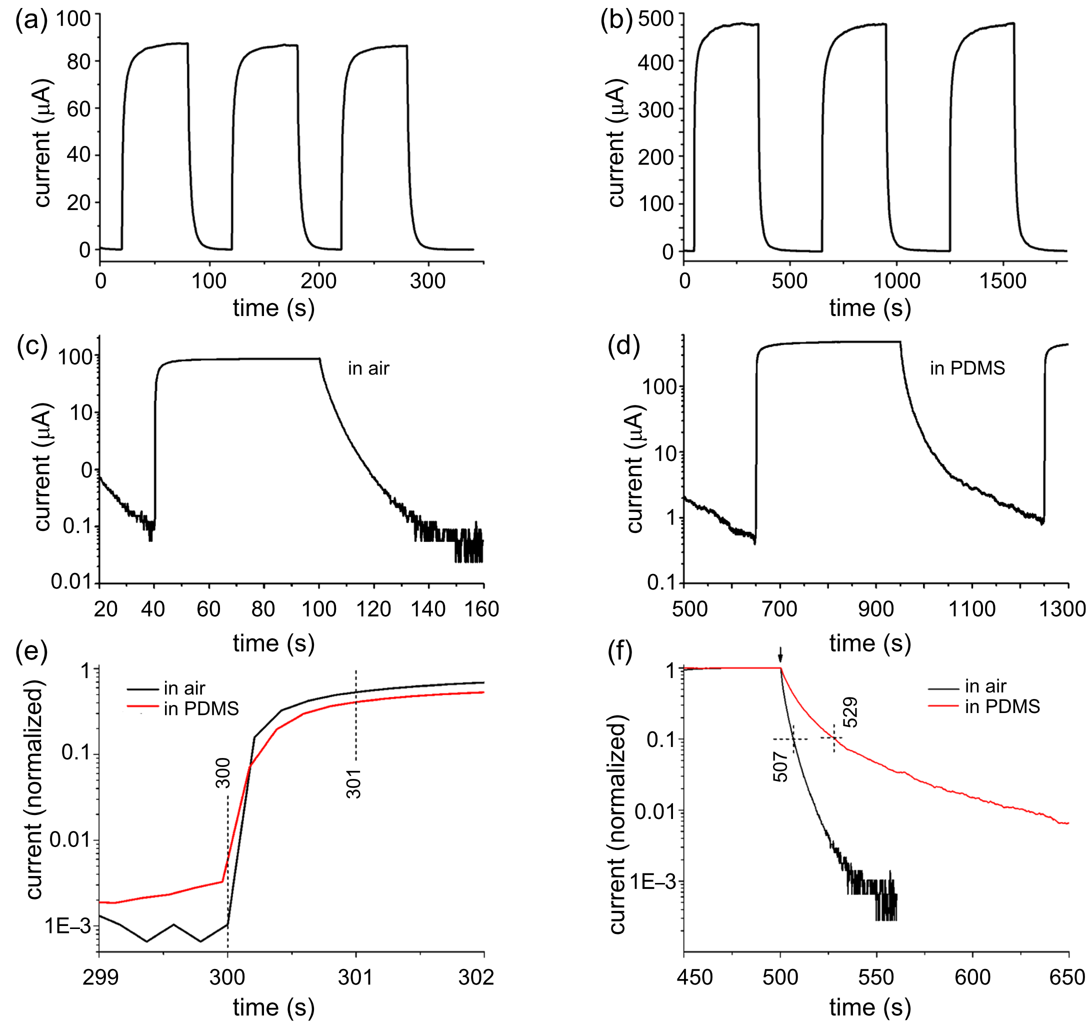

Figure 4: (a,b) UV photoresponse characteristics of ZnO nanowire sheets in air and in PDMS, respectively. The electrode of the device in air is vacuum-deposited Ti, and that of the device in PDMS is Ag–PDMS paste. The bias was set at 8 V for both devices; (c,d) UV photoresponse characteristics of the two devices with the current on a logarithmic scale; (e and f) comparison of the UV-photocurrent rising and dark-current decay of the nanowire films in air and PDMS, respectively, with the current normalized by the maximum.

dark current decay time as the time taken for the current to decay to 10% of the peak value. For the nanowire film in air the decay time is about 7 s, as shown in Figure 4f, whereas for that in PDMS the decay time is 29 s, i.e., about four times longer. Previous reports on ZnO nanowires that had gone through a lithography process involving polymers for making the electrodes [18-22], demonstrate a slow UV photoresponse compared to those that had never been in contact with polymers [7,9,10]. Surface contaminations from photoresist or electron-beam-resist polymers are probably responsible for the reduced response speed. The photoresponse speed of our ZnO nanowire film in PDMS is equivalent or even faster than for those contaminated by polymers from lithography processes, suggesting that ZnO nanowires in PDMS may be adequate for applications that do not require particularly high speeds.

The photoresponse of ZnO in air is known to be governed by the adsorption (in the dark) and desorption (under UV illumination) of oxygen molecules. In the dark, oxygen molecules adsorbed on the surface of ZnO nanowires capture free electrons of the n-type semiconductor: $O_2(g) + e^- \rightarrow O_2^-(ad)$. This produces a depletion layer near the nanowire surface, resulting in an upward band bending near the surface. Due to the large surface-to-volume ratio, the adsorption of O_2 significantly reduces the conductivity of the nanowires. UV-light illumination with a photon energy higher than E_g generates electron–hole pairs in the ZnO. Holes migrate to the surface along the potential slope created by the band bending and recombine with O_2-trapped electrons, thus releasing oxygen from the surface: $O_2^-(ad) + h^+ \rightarrow O_2(g)$. The heavily populated electrons in the conduction band enhance the conductivity of the ZnO nanowires.

The UV photoresponse of ZnO nanowires in PDMS can be explained with the help of Figure 5. After polymerization, the PDMS molecule chains of $CH_3[Si(CH_3)_2O]_nSi(CH_3)_3$, where n is the number of repeating monomer $[SiO(CH_3)_3]$ units, form a network polymer structure that is highly permeable. PDMS has a high oxygen permeability due to the large free volume from the flexibility of the siloxane (–SiO–) linkages; the oxygen concentration in PDMS has been reported as 2 mM [23]. The diffusion coefficient of oxygen in PDMS is reported as 3.55×10^{-5} $cm^2 \cdot s^{-1}$ [24]. Therefore, entangled PDMS molecule chains and dissociated oxygen molecules surround the ZnO nanowires, as illustrated in Figure 5a. The interaction between ZnO and the cross-linked PDMS is believed to be of the van der Waals type. Charge interaction between the two materials is unlikely to occur, based on the fact that the PL properties of ZnO nanowires in air and embedded in PDMS are very similar. In the dark the current of the nanowire film in PDMS reached 110 nA at 8 V as shown in Figure 3a, whereas the dark current of such a nanowire film exposed to air was only 0.1 nA at 8 V, as reported in our previous work [10]. This means that the nanowires in PDMS have a smaller surface available for the absorbtion of oxygen molecules. In fact, when a ZnO nanowire is embedded in cross-linked PDMS, it is conceivable that only the nanowire surface areas that are not in contact with PDMS adsorb oxygen molecules diffusing through the rubbery polymer (Figure 5b). Upon UV illumination the holes in the valence band combine with O_2-trapped electrons, releasing the surface O_2 and enhancing the photoconduction (Figure 5c). The desorbed O_2 diffuse into PDMS molecule networks, and are slowly re-adsorbed onto the ZnO nanowires after the UV light is switched off. PDMS molecule chains hamper the migration of oxygen molecules towards the ZnO nanowire surface, leading to the slow decay of the dark current. It is worth mentioning that the UV photoresponse speed of ZnO nanowires in an oxygen atmosphere is also dependent on the gas pressure, i.e., oxygen concentration: The lower the pressure the slower the UV photoresponse speed [4]. A number of silicone and polysulphone polymers have been studied for gas separation membranes [25,26]. Hence, we speculate that ZnO nanowires embedded in a gas-permeable polymer with higher oxygen permeability would have a faster UV photoresponse. The UV penetration depth in ZnO is less than 100 nm, whereas the thickness of the nanowire film is several micrometers, indicating that the contribution to the photoconduction of a nanowire sheet comes mostly from the top layers. With PDMS (refractive index ≈ 1.5) filling the interspaces between nanowires, the paper-like ZnO nanowire film becomes more translucent to the

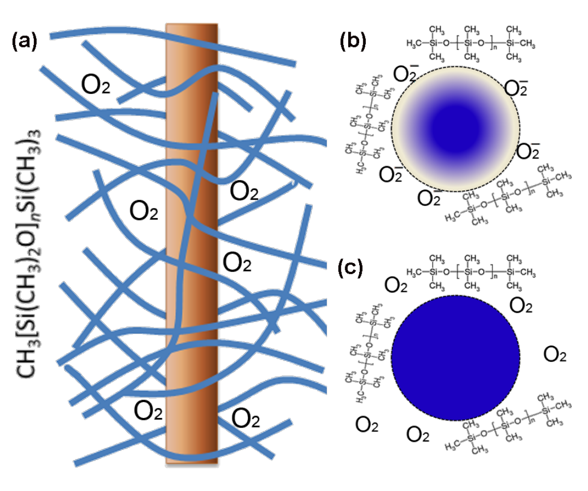

Figure 5: (a) Illustration of a ZnO nanowire in cross-linked PDMS. The blue lines represent PDMS molecule chains; (b) Illustration of a nanowire in PDMS without UV illumination, with oxygen adsorbed on parts of the surface. The colour gradient across the cross-section indicates a depletion layer near the surface; (c) Under UV illumination the oxygen molecules desorb from ZnO and diffuse into the molecule network.

naked eye, facilitating UV-light scattering to a deeper level in the nanowire sheet. Therefore more nanowires will receive UV photons, leading to the enhanced responsivity of the nanowire sheet in PDMS.

Conclusion

In summary, we demonstrated that ZnO nanowires embedded in PDMS polymer show great promise for UV detection. Our device based on a free-standing nanowire sheet in PDMS is bendable and facile to fabricate. The rubbery PDMS, which is gas permeable, not only provides protection to ZnO nanowires but also enables them to adsorb oxygen molecules diffusing through the polymer. Hence the UV-photoresponse mechanism of the nanowires in PDMS is analogous to that of nanowires exposed to an oxygen atmosphere. The PDMS coating over ZnO nanowires leads to an enhancement of responsivity, but at the expense of speed compared to the same uncoated nanowires. However, the response speed of the ZnO nanowire film in PDMS is still acceptable and in the range previously reported for ZnO nanowire films exposed to air. Our study opens a way for making robust UV photosensors incorporating ZnO nanowires embedded in gas-permeable polymers.

Experimental

The ZnO nanowires were synthesized within a horizontal tube furnace (inner diameter 5 cm) at atmospheric pressure without the use of any catalyst. Mixtures of ZnO and graphite powders (2–3 g), at a weight ratio of 1:1, were heated to 1100–1200 °C, and the vaporized growth species were transported by a gas flow that consisted of 1000 sccm N_2 and 30 sccm O_2. Cotton-like white products were deposited in the low-temperature (between ca. 200 °C and room temperature) region. We placed a curved aluminium foil against the inner wall of the quartz tube for collection of the nanowire product [17]. Thin sheets of ZnO nanowires were fabricated by a simple filtration method. First, a ZnO-nanowire suspension, with a concentration of 1 $\text{mg}\cdot\text{mL}^{-1}$, was prepared by ultrasonic dispersion of the nanowires in isopropanol. Subsequently, the ZnO-nanowire suspension was vacuum filtered through a porous anode aluminum oxide (AAO) membrane, diameter of 4.3 cm and pore size of 200 nm, purchased from Whatman Co. Then the network film of ZnO nanowires on an AAO membrane was dried in air at 100 °C for 1 h. Finally, the thin sheet of ZnO nanowires was detached from the membrane filter.

PDMS polymer was prepared by mixing the viscous PDMS liquid (Sylgard 184) and the cross-linking agent at a mass ratio of 10:1. The mixed PDMS was poured into a polystyrene Petri dish and dried in vacuum for 5 h to form a rubbery PDMS film. The PDMS liquid was also used for making the silver paste by blending with Ag nanopowder (diameter ca. 100 nm). The device fabrication process is illustrated in Figure 6. First, a poly(ethylene terephthalate) (PET) film is placed onto a PDMS layer. Onto the PET film a strap-shaped ZnO nanowire film is laid down and then silver paste is painted at the two ends. At each end a thin copper wire is in contact with the silver paste. We wait for 5 h until the PDMS blended with Ag nanoparticles is cured. Afterwards, we put the device into a plastic Petri dish and pour PDMS liquid onto the nanowire film to thoroughly seal the device, followed by a vacuum drying process for cross-linking of the polymer. The thickness of the PDMS layer above the ZnO nanowire film can be controlled by adjusting the volume of PDMS liquid in the Petri dish. In this work the thickness of the PDMS layer above the ZnO nanowire film was about 2 mm.

For the devices to be measured in air, we deposited 100 nm thick metal electrodes (Ti or Ag) onto the strap-shaped ZnO nanowire sheets (width 2 mm) by e-beam evaporation through a shadow mask. The electrode area was 3 mm long and 2 mm wide, as defined by the hollow pattern in the shadow mask. The gap between two opposite electrodes was 10 mm.

Acknowledgements

We thank the QUT Vice-Chancellor's Research Fellowship for financially supporting this research. This work was also partially supported by the NIRAP program "Solar Powered Nanosensors" of the Queensland Government and the National Research Foundation of Korea through the Priority Research Centers Program (KRF-2011-0030745)

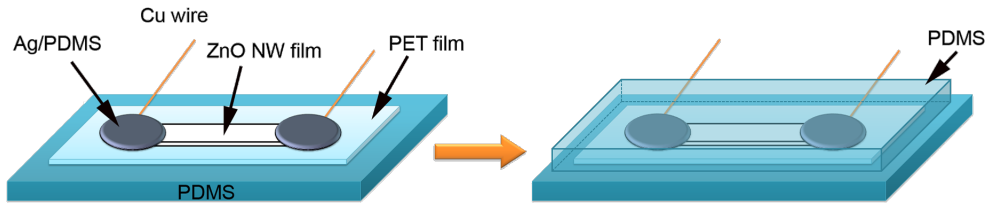

Figure 6: Illustration for the device fabrication process.

References

1. Özgür, Ü.; Alivov, Y. I.; Liu, C.; Teke, A.; Reshchikov, M. A.; Doğan, S.; Avrutin, V.; Cho, S.-J.; Morkoç, H. *J. Appl. Phys.* **2005,** *98,* 041301. doi:10.1063/1.1992666
2. Willander, M.; Nur, O.; Zhao, Q. X.; Yang, L. L.; Lorenz, M.; Cao, B. Q.; Zúñiga Pérez, J.; Czekalla, C.; Zimmermann, G.; Grundmann, M.; Bakin, A.; Behrends, A.; Al-Suleiman, M.; El-Shaer, A.; Che Mofor, A.; Postels, B.; Waag, A.; Boukos, N.; Travlos, A.; Kwack, H. S.; Guinard, J.; Le Si Dang, D. *Nanotechnology* **2009,** *20,* 332001. doi:10.1088/0957-4484/20/33/332001
3. Soci, C.; Zhang, A.; Xiang, B.; Dayeh, S. A.; Aplin, D. P. R.; Park, J.; Bao, X. Y.; Lo, Y. H.; Wang, D. *Nano Lett.* **2007,** *7,* 1003. doi:10.1021/nl070111x
4. Li, Q. H.; Gao, T.; Wang, Y. G.; Wang, T. H. *Appl. Phys. Lett.* **2005,** *86,* 123117. doi:10.1063/1.1883711
5. Ahn, S. E.; Ji, H. J.; Kim, K.; Kim, G. T.; Bae, C. H.; Park, S. M.; Kim, Y.-K.; Ha, J. S. *Appl. Phys. Lett.* **2007,** *90,* 153106. doi:10.1063/1.2721289
6. Kind, H.; Yan, H.; Messer, B.; Law, M.; Yang, P. *Adv. Mater.* **2002,** *14,* 158–160. doi:10.1002/1521-4095(20020116)14:2<158::AID-ADMA158>3.0.CO;2-W
7. Li, Y.; Valle, F. D.; Simonnet, M.; Yamada, I.; Delaunay, J.-J. *Nanotechnology* **2009,** *20,* 045501. doi:10.1088/0957-4484/20/4/045501
8. Zheng, X. J.; Yang, B.; Zhang, T.; Jiang, C. B.; Mao, S. X.; Chen, Y. Q.; Yuan, B. *Appl. Phys. Lett.* **2009,** *95,* 221106. doi:10.1063/1.3258462
9. Hsu, C.-L.; Chang, S.-J.; Lin, Y.-R.; Li, P.-C.; Lin, T.-S.; Tsai, S.-Y.; Lu, T.-H.; Chen, I.-C. *Chem. Phys. Lett.* **2005,** *416,* 75. doi:10.1016/j.cplett.2005.09.066
10. Liu, J.; Park, J.; Park, K. H.; Ahn, Y.; Park, J.-Y.; Koh, K. H.; Lee, S. *Nanotechnology* **2010,** *21,* 485504. doi:10.1088/0957-4484/21/48/485504
11. Li, Y.; Valle, F. D.; Simmonnet, M.; Yamada, I.; Delaunay, J.-J. *Appl. Phys. Lett.* **2009,** *94,* 023110. doi:10.1063/1.3073042
12. Pan, Z.; Tao, J.; Zhu, Y.; Huang, J.-F.; Paranthaman, M. P. *Chem. Mater.* **2010,** *22,* 149. doi:10.1021/cm902734e
13. Lao, C. S.; Park, M.-C.; Kuang, Q.; Deng, Y.; Sood, A. K.; Polla, D. L.; Wang, Z. L. *J. Am. Chem. Soc.* **2007,** *129,* 12096. doi:10.1021/ja075249w
14. He, J. H.; Lin, Y. H.; McConney, M. E.; Tsukruk, V. V.; Wang, Z. L. J.; Bao, G. *Appl. Phys. Lett.* **2007,** *102,* 084303. doi:10.1063/1.2798390
15. Stern, S. A. *J. Membr. Sci.* **1994,** *19,* 1. doi:10.1016/0376-7388(94)00141-3
16. Liu, J.; Ahn, Y. H.; Park, J.-Y.; Koh, K. H.; Lee, S. *Nanotechnology* **2009,** *20,* 445203. doi:10.1088/0957-4484/20/44/445203
17. Liu, J.; Lee, S.; Ahn, Y. H.; Park, J.-Y.; Koh, K. H. *J. Phys. D: Appl. Phys.* **2009,** *42,* 095401. doi:10.1088/0022-3727/42/9/095401
18. Bai, S.; Wu, W.; Qin, Y.; Cui, N.; Bayerl, D. J.; Wang, X. *Adv. Funct. Mater.* **2011,** *21,* 4464. doi:10.1002/adfm.201101319
19. Park, J. Y.; Song, D. E.; Kim, S. S. *Nanotechnology* **2008,** *19,* 105503. doi:10.1088/0957-4484/19/10/105503
20. Suehiro, J.; Nakagawa, N.; Hidaka, S.-i.; Ueda, M.; Imasaka, K.; Higashihata, M.; Okada, T.; Hara, M. *Nanotechnology* **2006,** *17,* 2567. doi:10.1088/0957-4484/17/10/021
21. Lupan, O.; Chai, G.; Chow, L.; Emelchenko, G. A.; Heinrich, H.; Ursaki, V. V.; Gruzintsev, A. N.; Tiginyanu, I. M.; Redkin, A. N. *Phys. Status Solidi A* **2010,** *207,* 1735. doi:10.1002/pssa.200983706
22. Park, J. Y.; Yun, Y. S.; Hong, Y. S.; Oh, H.; Kim, J.-J.; Kim, S. S. *Appl. Phys. Lett.* **2005,** *87,* 123108. doi:10.1063/1.2053365
23. Kamiya, Y.; Naito, Y.; Hirose, T.; Mizoguchi, K. *J. Polym. Sci., Part B: Polym. Lett.* **1990,** *28,* 1297. doi:10.1002/polb.1990.090280808
24. Cox, M. E.; Dunn, B. *J. Polym. Sci., Part A: Polym. Chem.* **1986,** *24,* 621. doi:10.1002/pola.1986.080240405
25. Ettouney, H.; Majeed, U. *J. Membr. Sci.* **1997,** *135,* 251. doi:10.1016/S0376-7388(97)00150-6
26. Yampolskii, Y. P.; Motyakin, M. V.; Wasserman, A. M.; Masuda, T.; Teraguchi, M.; Khotimskii, V. S.; Freeman, B. D. *Polymer* **1999,** *40,* 1745. doi:10.1016/S0032-3861(98)00395-4

License and Terms

The definitive version of this article is the electronic one which can be found at:
doi:10.3762/bjnano.3.41

Beilstein Journal
of Nanotechnology

Structural, electronic and photovoltaic characterization of multiwalled carbon nanotubes grown directly on stainless steel

Luca Camilli*[1], Manuela Scarselli[1], Silvano Del Gobbo[1], Paola Castrucci[1],
Eric Gautron[2] and Maurizio De Crescenzi[1]

Full Research Paper

Address:
[1]Dipartimento di Fisica, Università di Roma Tor Vergata, 00133 Roma, Italy and [2]Institut des Matériaux Jean Rouxel, CNRS-UMR 6502, 44322 Nantes Cedex 3, France

Email:
Luca Camilli* - camilli@roma2.infn.it.

* Corresponding author

Keywords:
carbon nanotubes; electronic properties; heterojunction; photovoltaic; stainless steel

Beilstein J. Nanotechnol. **2012,** *3,* 360–367.
doi:10.3762/bjnano.3.42

Received: 18 January 2012
Accepted: 29 March 2012
Published: 02 May 2012

This article is part of the Thematic Series "Nanostructures for sensors, electronics, energy and environment".

Guest Editor: N. Motta

Abstract

We have taken advantage of the native surface roughness and the iron content of AISI-316 stainless steel to grow multiwalled carbon nanotubes (MWCNTs) by chemical vapour deposition without the addition of an external catalyst. The structural and electronic properties of the synthesized carbon nanostructures have been investigated by a range of electron microscopy and spectroscopy techniques. The results show the good quality and the high graphitization degree of the synthesized MWCNTs. Through energy-loss spectroscopy we found that the electronic properties of these nanostructures are markedly different from those of highly oriented pyrolytic graphite (HOPG). Notably, a broadening of the π-plasmon peak in the case of MWCNTs is evident. In addition, a photocurrent was measured when MWCNTs were airbrushed onto a silicon substrate. External quantum efficiency (EQE) and photocurrent values were reported both in planar and in top-down geometry of the device. Marked differences in the line shapes and intensities were found for the two configurations, suggesting that two different mechanisms of photocurrent generation and charge collection are in operation. From this comparison, we are able to conclude that the silicon substrate plays an important role in the production of electron–hole pairs.

Introduction

Carbon nanotubes (CNTs) possess unique electronic, mechanical and optical properties that make them interesting for fundamental studies as well as practical applications [1]. Among the various synthesis techniques, chemical vapour deposition is preferred in the field of electronics, since it allows for the direct growth of CNTs on substrates [2]. CNTs are generally synthesized on Si or Si/SiO$_2$ substrates; however, in some types of applications, such as in field-emission devices, the use of conductive substrates is particularly mandatory [3]. In particular, stainless steel (SS) is one of the most attractive conductive substrates, due to its low price and good processability. Recently, several efforts have been made to grow CNTs on SS substrates with [4,5] or without [6,7] the addition of an external catalyst. In particular, we have shown that the growth of high quality multiwalled CNTs on SS in the absence of an external catalyst is possible because the nanoscale roughness and the metallic nature of the substrate surface both act as an efficient catalyst/template in the synthesis of tubular nanostructures [7]. Here we first investigate the electronic properties of CNTs with the aim to compare them to those of graphite. As is well known, multiwalled CNTs, conversely to single-walled ones, should have a structure very similar to that of graphite, due to the great number of walls and the reduced radius of curvature. Despite this, we find that the CNT electronic properties obtained by energy-loss spectroscopy (ELS) in the loss region up to 30 eV from the elastic peak are quite different to those of graphite. In particular, a broadening of the π-plasmon of CNTs is found, which can be ascribed to the presence of several structures that are completely absent in HOPG and probably due to transitions among Van Hove singularities.

Here we also show that MWCNTs exhibit an interesting photovoltaic activity when they are deposited on a crystalline silicon substrate by the airbrush method. We recall that, while several efforts have been devoted to the build-up of photovoltaic devices based on a SWCNT–Si heterojunction, achieving a surprising efficiency of up to 11% [8], just a few works reported the ability of MWCNTs to serve as an energy-conversion material [9,10]. In this paper, we build up a simple photovoltaic device based on MWCNT–Si Schottky heterojunction. Photovoltaic measurements for the in-plane and top-down geometries of the device were performed. In particular, we find that the top-down geometry gives a photocurrent intensity and an external quantum efficiency (EQE) value much higher than those measured in the in-plane configuration.

Results and Discussion

In Figure 1 the chemical vapour deposition chamber used to grow the CNTs is displayed. The stainless-steel substrate is mounted on a sample holder and heated up to 730 °C in acetylene atmosphere to synthesize CNTs (see the Experimental section for more details).

Figure 1: (a) Photograph of the chemical vapour deposition chamber used to synthesize MWCNTs. The reactor comprises an UHV chamber, pumped by an ion pump and equipped with a manipulator capable of reaching temperatures of about 800–900 °C. Acetylene and argon fluxes, introduced in the chamber through the gas line highlighted by the arrow, are adjusted by means of two suitable valves. (b) Schematics showing the CVD process: The stainless-steel substrate is mounted on a heatable molybdenum sample holder. After a temperature of 750 °C has been achieved, acetylene gas (200 sccm) is inserted through a nozzle in the chamber under an Ar atmosphere.

Figure 2 shows a scanning electron microscopy image of the produced CNTs. They appear to be randomly oriented and no traces of other carbonaceous materials were detected in the scanned area. In general, only a very few traces of impurities were found in other spots of the sample. Transmission electron microscopy reveals that the CNTs are multiwalled in nature, with an average number of walls of about 20, as illustrated in Figure 3a and Figure 3b. The high graphitization degree of the synthesized nanostructures is evidenced in the inset of Figure 3b, in which the reported Fast Fourier Transform of the TEM image consists of two single points located at 0.35 nm from the centre.

In Figure 4 we report the carbon core-valence-valence (CVV) Auger features for HOPG and a MWCNT film. The Auger

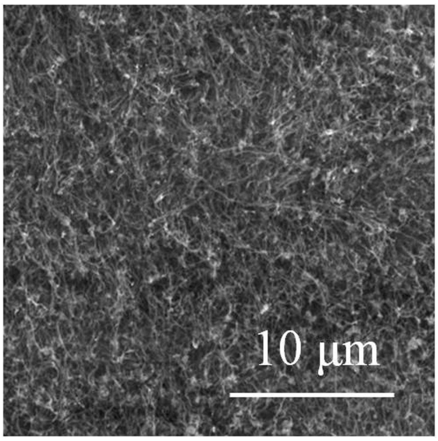

Figure 2: SEM image of the MWCNTs after growth on a stainless-steel substrate. The MWCNTs are randomly oriented, and no traces of other carbonaceous materials were detected in the large scanned area.

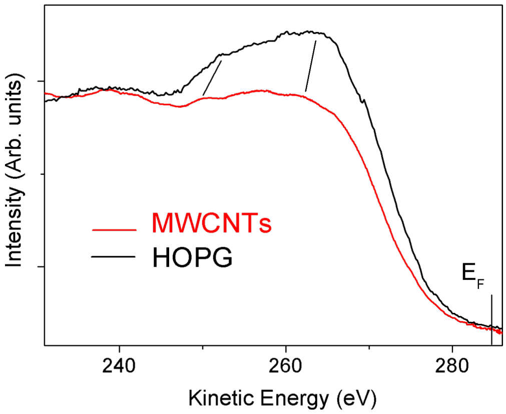

Figure 4: Core-valence-valence (CVV) Auger spectra of MWCNTs (red curve) and HOPG (black curve). An electron gun with a primary beam energy of 1500 eV was used as the exciting source. In the case of the MWCNT sample, the Auger peak is shifted towards lower kinetic energy with respect to HOPG. The Fermi level is at 284.4 eV.

spectra were acquired using an electron gun as the exciting source with a primary beam energy of 1500 eV. Bearing in mind that the Auger spectrum is a self-convolution of the filled valence states below the Fermi level, the two experimental spectra reported in Figure 4 show some significant differences, meaning that the filled states of the two materials are intrinsically dissimilar. The shift of the peaks is highlighted by thick markers. Similar results have already been reported [11], in which the Auger line shape of HOPG was compared to that of SWCNTs.

Figure 5 reports the ELS analysis performed, in reflection geometry, on both MWCNT and HOPG samples. We used an electron gun as the excitation source, with a primary beam energy of 300 eV. This value has been chosen to single out the contribution coming from the first layers of the MWCNT film only. The HOPG and MWCNT spectra both exhibit two characteristic features due to the π- and σ+π-plasmons [12], although in the case of the MWCNT structures these are shifted towards lower energy with respect to those of graphite (located at 6.5 and 26 eV), indicating a marked difference in the electronic properties.

Experimental evidence has shown that these plasmons exhibit an increase energetic downshift as the number of walls in the individual MWCNT being probed is reduced [13]. On the other hand, based on theoretical calculations, this effect is predicted to become greater as the number of intertube or intratube interactions decreases in bundles of SWCNTs and MWCNTs, respectively [14-16]. This finding is also in good agreement with

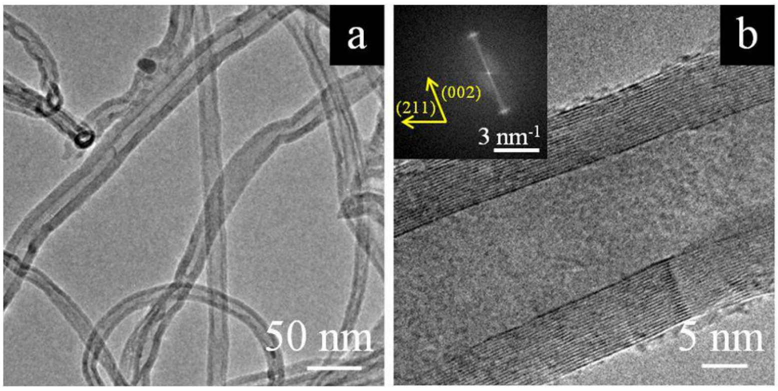

Figure 3: (a) Low-resolution TEM image assessing the multiwalled nature of the carbon nanotubes synthesized on SS. (b) High-resolution TEM picture of a single MWCNT with 19 walls. The inset displays the Fast Fourier Transform of the TEM image reported in (b). The two spots, at a semi-distance of 0.35 nm, represent the parallel walls.

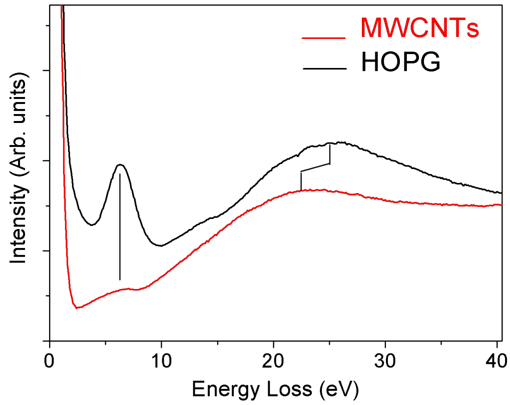

Figure 5: Energy-loss spectra of MWCNTs (red curve) and HOPG (black curve). In the case of MWCNTs, the σ+π-plasmon is shifted towards lower energy with respect to that of HOPG, located at about 26 eV, as indicated by the tick marker. The π-plasmon turns out to be sharp in HOPG (centred at 6.5 eV), whereas it is broader in MWCNTs.

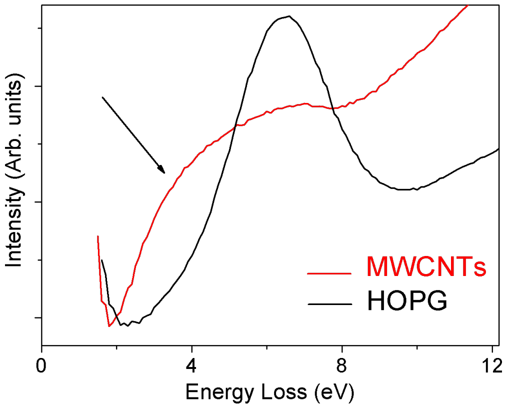

Figure 6: Comparison of the π-plasmon peak (0–12 eV) for MWCNTs (red curve) and HOPG (black curve). It is worth noting that in the case of MWCNTs we find electronic structures also at 2.0–4.5 eV, while in HOPG they are completely absent. These features contribute to the π-plasmon, giving rise to a very broad peak. Transitions between Van Hove singularities are thought to be responsible for these additional features.

our previous results, in which we reported ELS data collected in transmission on an isolated MWCNT [9]. In addition, it is highlighted in Figure 6 that the π-plasmon of HOPG shows a sharp peak, while the same plasmon feature in the case of MWCNTs is much broader, appearing as a shoulder that spreads over 2–4 eV in energy loss. The latter case is the result of the additional contribution coming from electronic transitions completely absent in graphite and due to the quasi-one-dimensionality of the CNTs. In the case of SWCNTs, excitations between localized electronic states related to Van Hove singularities have been invoked as an interpretation for such transitions [15]. These electronic transitions create electron–hole pairs upon illumination and, thus, have been considered to be responsible for the generation of photocurrent in SWCNTs. Since in the electronic density of states of MWCNTs such a singularity is still present [9], we think that the experimentally measured shoulder should have the same origin. Shyu and Lin report a complete calculation of these energy-loss features, dependent on the number of walls in the nanotube structure [14].

Figure 7 shows a 10 × 10 μm^2 atomic force microscopy (AFM) image of the as-exfoliated HOPG sample used for spectroscopic characterization. Figure 8 shows the scheme of the two different architectures used to build and test the photovoltaic device. In the in-plane configuration the T1 switch is on while T2 is off; the situation is reversed in the top-down configuration.

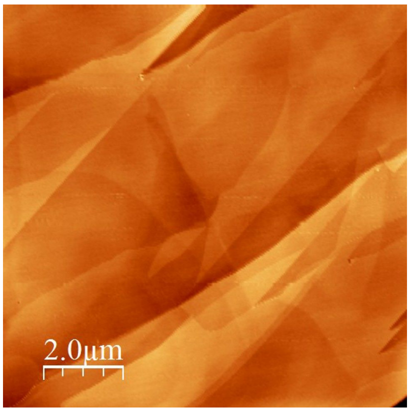

Figure 7: AFM 10 × 10 μm^2 topography image of the as-exfoliated HOPG sample. The surface appears clean and several steps can be observed.

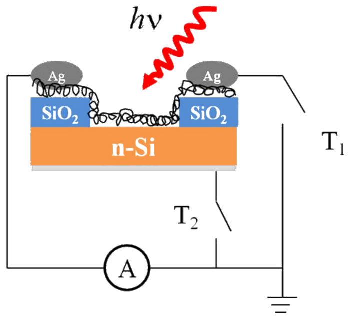

Figure 8: Scheme of the photovoltaic device. The Schottky junction between the Si and the MWCNT film is the photoactive junction. Steps of SiO$_2$ (300 nm) are used to avoid a short-circuit forming between the silver paint (top electrode) and the silicon substrate. The back contact is made of aluminium. In the in-plane geometry, the switch T1 is on and T2 is off; and vice versa in the top-down configuration. As a result, the photocurrent is collected at the MWCNT film in the former case, and at the MWCNTs and Si (back contact) in the latter.

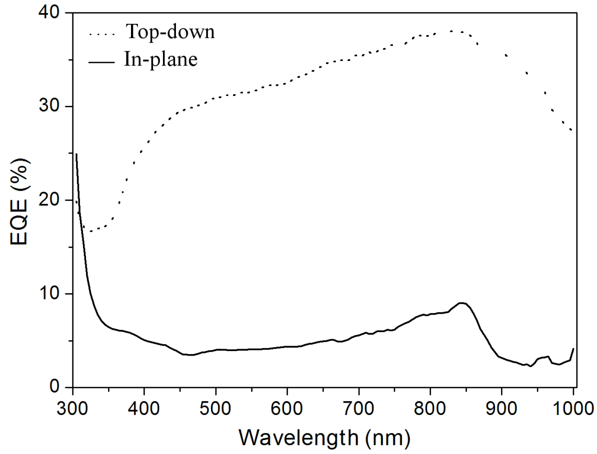

Figure 9: External quantum efficiency (EQE) spectra obtained in the top-down (dotted curve) and in-plane (filled curve) geometries of the device. The maximum value achieved in the case of the top-down configuration is 37% (at 850 nm), while in the planar one it is 10% (at 850 nm). The two line shapes are very different: in the top-down setup the EQE curve is very similar to that of a commercial p–n silicon solar cell, with a low absorption at ultraviolet wavelengths, whereas in the in-plane case, there is a rise that is characteristic of MWCNT absorption.

Figure 9 displays the photoresponse of our device, for both configurations, acquired at null applied voltage and with the light spot (1 × 2 mm^2) impinging on the MWCNT film. As one can see, the maximum value of EQE achieved in the case of the vertical setup (top-down geometry) is 37%, which is much higher than the 10% obtained in case of the in-plane geometry. Moreover, the EQE line shape is very different in the two cases. While, in top-down geometry, the EQE response clearly resembles the behaviour of a commercial p–n silicon solar cell; in the in-plane architecture there is a further contribution at ultraviolet wavelengths, following the MWCNT optical absorbance. We can assess that in both cases the EQE spectrum is a sum of two contributions, one coming from the MWCNTs and the other from the Si beneath. However, the contribution of the Si is strongly enhanced in the top-down setup, while in the in-plane one the electron–hole pairs generated by Si recombine before reaching the electrodes.

Strong differences between the two architectures are also evident when we compare the current–voltage curves collected. As reported in Figure 10a and Figure 10b, the open-circuit voltage (V_{oc}) and the short-circuit density current (J_{sc}) in the in-plane configuration are markedly lower than those collected in the top-down geometry. The lower value of J_{sc} can be justified by the fact that the MWCNTs have essentially a metallic character, thus showing a scarce photovoltaic effect. On the contrary, in the top-down architecture, the main contribution to the photocurrent comes from Si, thus giving a J_{sc} value 10^2 times higher. This particular behaviour can be understood if we consider the position of the electrodes through which the current is collected. In the in-plane geometry, the electrodes are in contact only with the CNT film (and the thick silicon oxide underneath), thus collecting carriers coming mainly from the nanostructures, since the majority of the carriers from the Si recombine during the percolation into the CNT film. On the other hand, in the top-down geometry, we have the two top electrodes contacting the CNT film, while the bottom one is in touch with the silicon substrate. In this way we can collect directly the carriers coming both from the CNTs (top electrodes) and from the Si (bottom).

We notice also that in case of top-down setup the *J–V* curve line shape shows a double-diode-like behaviour. This effect is probably due to the presence of a second Schottky junction at the interface between Si and Al at the back of the device, meaning that this contact is not ohmic.

Concerning the solar conversion efficiency, we obtain 0.17% in the top-down setup. This value is in accordance with recently published data obtained for a solar cell based on a MWCNT/Si heterojunction [17]. However, the nearly linear behaviour of the *J–V* characteristic in the fourth quadrant under illumination suggests that parasitic resistances are present in the device. For this reason, we think that the performance of our device can be improved by adjustment of different parameters, such as (a) the quality of the contact between the CNTs and the metallic top electrodes; (b) making an ohmic contact at the back of the silicon substrate; and (c) producing a MWCNT film of suitable thickness, thus allowing the photons to reach the heterojunction with the Si substrate.

Conclusion

In this paper we have shown a facile method to grow CNTs by chemical vapour deposition directly on SS sheet, without the addition of an external catalyst. This implies that there is no need for a additional post-growth purification process. We have highlighted the differences in the electronic properties between MWCNTs and HOPG. In particular, by comparing the ELS spectra we evidenced the presence of electronic structures close to the π-plasmon, which can be assigned to transitions between Van Hove singularities and which explains the ability of CNTs to create electron–hole pairs (excitons) under illumination by light. These features are completely absent in HOPG, for which the π-plasmon peak has a sharp characteristic, and are due to the quasi-one-dimensionality of the CNTs. We have exploited the photovoltaic activity of MWCNTs in a device made of MWCNTs airbrushed onto a Si substrate. We evidenced the formation of a Schottky junction at the interface. EQE spectra and *J–V* characteristics were acquired with two different geometries

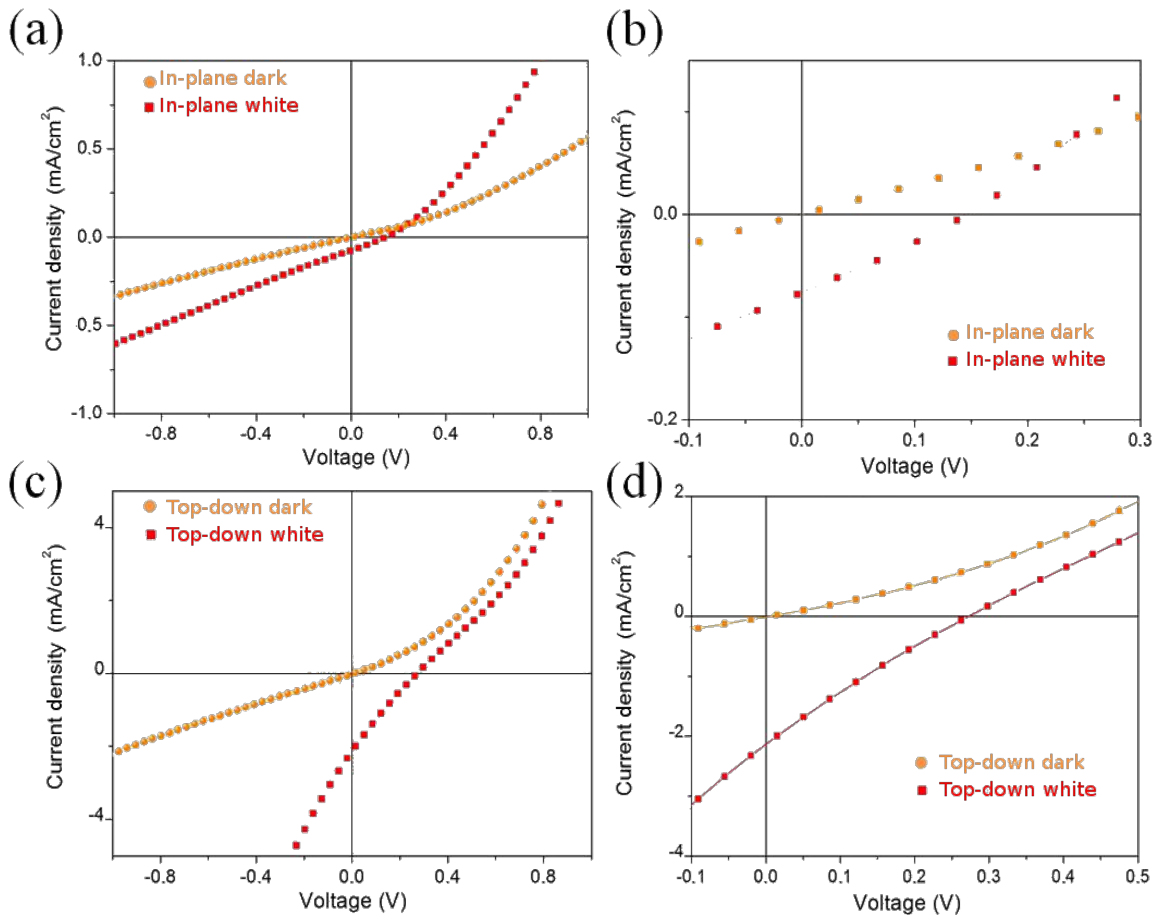

Figure 10: *J*–*V* characteristics acquired in the dark and under illumination by white light. (a) In the in-plane geometry: V_{oc} = 0.2 V, J_{sc} = 0.09 mA/cm^2. In the third and fourth quadrant the *J*–*V* curve is almost linear. This could be due to the presence of parasitic resistances, which lower the performance of the device. An inhomogeneous MWCNT film, in which all the MWCNTs are not in good contact with each other, could be the cause of such a high resistance. (b) Detail of (a) in the most meaningful zone, i.e., in the fourth quadrant of the *J*–*V* characteristic. (c) Top-down geometry: V_{oc} = 0.25 V, J_{sc} = 2.2 mA/cm^2. Under illumination, the *J*–*V* curve line shape exhibits the behaviour of a double diode: beyond the MWCNT–Si Schottky junction, the second one is formed at the back contact between Si and Al, i.e., a hint of a non-ohmic contact. (d) Detail of (c) in the most meaningful zone, i.e., in the fourth quadrant of the *J*–*V* characteristic.

(in-plane and top-down) to study the role played by the excitons generated in the MWCNTs. In the in-plane configuration the main contribution to the photocurrent comes from the MWCNTs, while in the top-down setup the role of silicon dominates, because the excitons generated in the depletion layer are collected before reaching the electrode and recombine. Further improvements should be devoted to enhance the efficiency of the device by improving the quality of the metallic contact, to avoid parasitic additional resistances.

Experimental

A sheet of AISI 316-SS (30 × 40 mm^2, from Goodfellow Cambridge Ltd.) was placed on a molybdenum sample holder, acting as a resistive heater, and inserted into the chemical vapour deposition chamber (see Figure 1). After air was removed by a rotary pump, argon gas (12 torr) was inserted. When the desired temperature was reached (750 °C) acetylene gas was introduced (200 sccm) into the chamber to start the CNT growth. After 10 min, the acetylene flow was stopped and argon (500 sccm) was inserted again for 5 min to stop the reaction, while the chamber was pumped off. More details are reported elsewhere [7]. AFM (VEECO multiprobe) characterization was performed in air by using a nonconductive Si tip in tapping mode. After the synthesis process, a piece of SS substrate covered by the as-grown MWCNTs was inserted into an ultrahigh vacuum chamber (base pressure 10^{-10} torr) for Auger and electron energy-loss measurements. An electron gun as excitation source and a semi-imaging electron analyzer MAC2 (Riber Instruments) operating in the constant-pass-energy mode (with a total energy resolution of 1.1 eV) were used. The HOPG sample was exfoliated before introduction to the analysis chamber.

In order to detach the MWCNTs from the steel substrate after the growth, the sample was sonicated in isopropyl alcohol. The obtained solution was then airbrushed on a patterned n-Si/SiO_2 substrate (Figure 11). The SiO_2 steps are needed to prevent a short circuit between the top electrodes and the Si underneath (see Figure 8 and Figure 10). The airbrushed MWCNTs form a quasi-continuous film, which creates the photoactive Schottky heterojunction with the Si. The top electrodes were made of silver paint, while the rear contact was sputtered aluminium. The photocurrent spectra were measured by using an optical setup comprising a xenon lamp equipped with a monochromator, focusing and collecting optics, a reflecting chopper and lock-in electronics. The light spot size was 1 × 2 mm^2. The photocurrent density, $I(\lambda)$, was measured under illumination as a function of the incident photon wavelength, λ. The incident photon power density was monitored with a calibrated silicon photodiode and data were collected by a lock-in technique. The external quantum efficiency (EQE) is defined as the fraction of the incident photons, N_{ph}, converted into photocurrent, i.e., the number of the generated electron–hole pairs, N_{e-h}, multiplied by the electronic charge, e. The number of the incident photons is then evaluated in terms of the power density of the Xe lamp, $P(\lambda)$, since $N_{ph} = \lambda P(\lambda)/hc$. Therefore, it results that EQE (%) = electrons/photons = 100 $hcI(\lambda)/e\lambda P(\lambda)$. $I(\lambda)$ was measured by modulating the light by an optical chopper and recovering the amplified current signal (converted to voltage) with a lock-in amplifier locked to the chopper frequency. The lamp power $P(\lambda)$ was measured simultaneously in a similar way, by a calibrated Si photodiode; h is the Planck constant, c is the speed of light in vacuum and e the electron charge. A Keithley 2602A source meter was used to record the J–V curves both in the dark and under white-light illumination.

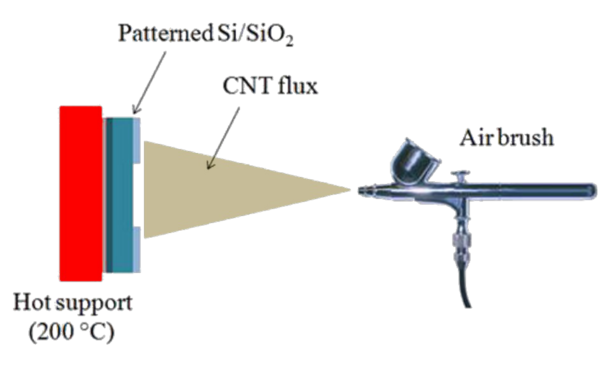

Figure 11: Schematic depiction of the airbrush deposition process. A solution of MWCNTs in isopropyl alcohol was airbrushed onto a Si/SiO_2 sample. The SiO_2 steps avoid the formation of a short circuit between the top electrodes and the Si. The Si window was 5 × 5 mm^2. During airbrushing, the device was mounted on a heatable holder (~200 °C) in order to allow an instantaneous evaporation of the solvent, thus avoiding the formation of droplets.

Acknowledgements

This work was supported by the Air Force Office of Scientific Research Material Command, USAF, under grant no. FA8655-11-1-306 and by the Queensland Government smart futures fund National and International Research Alliances Program (NIRAP): solar powered nano-sensors for data acquisition and surveying in remote areas.

References

1. Baughman, R. H.; Zakhidov, A. A.; de Heer, W. A. *Science* **2002,** *297,* 787–792. doi:10.1126/science.1060928
2. Graham, A. P.; Duesberg, G. S.; Hoenlein, W.; Kreupl, F.; Liebau, M.; Martin, R.; Rajasekharan, B.; Pamler, W.; Seidel, R.; Steinhoegl, W.; Unger, E. *Appl. Phys. A: Mater. Sci. Process.* **2005,** *80,* 1141–1151. doi:10.1007/s00339-004-3151-7
3. Hiraoka, T.; Yamada, T.; Hata, K.; Futaba, D. N.; Kurachi, H.; Uemura, S.; Yumura, M.; Iijima, S. *J. Am. Chem. Soc.* **2006,** *128,* 13338–13339. doi:10.1021/ja0643772
4. Kim, B.; Chung, H.; Chu, K. S.; Yoon, H. G.; Lee, C. J.; Kim, W. *Synth. Met.* **2010,** *160,* 584–587. doi:10.1016/j.synthmet.2009.12.008
5. Duy, D. Q.; Kim, H. S.; Yoon, D. M.; Lee, K. J.; Ha, J. W.; Hwang, Y. G.; Lee, C. H.; Cong, B. T. *Appl. Surf. Sci.* **2009,** *256,* 1065–1068. doi:10.1016/j.apsusc.2009.05.106
6. Baddour, C. E.; Fadlallah, F.; Nasuhoglu, D.; Mitra, R.; Vandsburger, L.; Meunier, J. L. *Carbon* **2009,** *47,* 313–318. doi:10.1016/j.carbon.2008.10.038
7. Camilli, L.; Scarselli, M.; Del Gobbo, S.; Castrucci, P.; Nanni, F.; Gautron, E.; Lefrant, S.; De Crescenzi, M. *Carbon* **2011,** *49,* 3307–3315. doi:10.1016/j.carbon.2011.04.014
8. Jia, Y.; Li, P.; Gui, X.; Wei, J.; Wang, K.; Zhu, H.; Wu, D.; Zhang, L.; Cao, A.; Xu, Y. *Appl. Phys. Lett.* **2011,** *98,* 133115. doi:10.1063/1.3573829
9. Castrucci, P.; Scilletta, C.; Del Gobbo, S.; Scarselli, M.; Camilli, L.; Simeoni, M.; Delley, B.; Continenza, A.; De Crescenzi, M. *Nanotechnology* **2011,** *22,* 115701. doi:10.1088/0957-4484/22/11/115701
10. El Khakani, M. A.; Le Borgne, V.; Aïssa, B.; Rosei, F.; Scilletta, C.; Speiser, E.; Scarselli, M.; Castrucci, P.; De Crescenzi, M. *Appl. Phys. Lett.* **2009,** *95,* 083114. doi:10.1063/1.3211958
11. Perfetto, E.; Cini, M.; Ugenti, S.; Castrucci, P.; Scarselli, M.; De Crescenzi, M.; Rosei, F.; El Khakani, M. A. *Phys. Rev. B* **2007,** *76,* 233408. doi:10.1103/PhysRevB.76.233408
12. Calliari, L.; Fanchenko, S.; Filippi, M. *Carbon* **2007,** *45,* 1410–1418. doi:10.1016/j.carbon.2007.03.034
13. Bursill, L. A.; Stadelmann, P. A.; Peng, J. L.; Prawer, S. *Phys. Rev. B* **1994,** *49,* 2882–2887. doi:10.1103/PhysRevB.49.2882
14. Shyu, F. L.; Lin, M. F. *Phys. Rev. B* **2000,** *62,* 8508–8516. doi:10.1103/PhysRevB.62.8508
15. Kramberger, C.; Hambach, R.; Giorgetti, C.; Rümmeli, M. H.; Knupfer, M.; Fink, J.; Büchner, B.; Reining, L.; Einarsson, E.; Maruyama, S.; Sottile, F.; Hannewald, K.; Olevano, V.; Marinopoulos, A. G.; Pichler, T. *Phys. Rev. Lett.* **2008,** *100,* 196803. doi:10.1103/PhysRevLett.100.196803
16. Marinopoulos, A. G.; Reining, L.; Rubio, A.; Vast, N. *Phys. Rev. Lett.* **2003,** *91,* 046402. doi:10.1103/PhysRevLett.91.046402
17. Jia, Y.; Li, P.; Wei, J.; Cao, A.; Wang, K.; Li, C.; Zhuang, D.; Zhu, H.; Wu, D. *Mater. Res. Bull.* **2010,** *45,* 1401–1405. doi:10.1016/j.materresbull.2010.06.045

License and Terms

Beilstein Journal of Nanotechnology

Functionalised zinc oxide nanowire gas sensors: Enhanced NO_2 gas sensor response by chemical modification of nanowire surfaces

Eric R. Waclawik*[1], Jin Chang[1], Andrea Ponzoni[2], Isabella Concina[2], Dario Zappa[2], Elisabetta Comini[2], Nunzio Motta[1], Guido Faglia[2] and Giorgio Sberveglieri[2]

Full Research Paper

Address:
[1]School of Chemistry, Physics & Mechanical Engineering, Queensland University of Technology, 2 George Street, 4000 Brisbane, Australia and [2]SENSOR Lab, CNR-IDASC & Brescia University, Chemistry & Physics Department, Via Valotti 9, 25133 Brescia, Italy

Email:
Eric R. Waclawik* - e.waclawik@qut.edu.au

* Corresponding author

Keywords:
gas sensor; nanowire; tris(hydroxymethyl)aminomethane; self-assembled monolayer; zinc oxide

Beilstein J. Nanotechnol. **2012,** *3,* 368–377.
doi:10.3762/bjnano.3.43

Received: 13 January 2012
Accepted: 16 March 2012
Published: 02 May 2012

This article is part of the Thematic Series "Nanostructures for sensors, electronics, energy and environment".

Associate Editor: P. Ziemann

Abstract

Surface coating with an organic self-assembled monolayer (SAM) can enhance surface reactions or the absorption of specific gases and hence improve the response of a metal oxide (MOx) sensor toward particular target gases in the environment. In this study the effect of an adsorbed organic layer on the dynamic response of zinc oxide nanowire gas sensors was investigated. The effect of ZnO surface functionalisation by two different organic molecules, tris(hydroxymethyl)aminomethane (THMA) and dodecanethiol (DT), was studied. The response towards ammonia, nitrous oxide and nitrogen dioxide was investigated for three sensor configurations, namely pure ZnO nanowires, organic-coated ZnO nanowires and ZnO nanowires covered with a sparse layer of organic-coated ZnO nanoparticles. Exposure of the nanowire sensors to the oxidising gas NO_2 produced a significant and reproducible response. ZnO and THMA-coated ZnO nanowire sensors both readily detected NO_2 down to a concentration in the very low ppm range. Notably, the THMA-coated nanowires consistently displayed a small, enhanced response to NO_2 compared to uncoated ZnO nanowire sensors. At the lower concentration levels tested, ZnO nanowire sensors that were coated with THMA-capped ZnO nanoparticles were found to exhibit the greatest enhanced response. $\Delta R/R$ was two times greater than that for the as-prepared ZnO nanowire sensors. It is proposed that the $\Delta R/R$ enhancement in this case originates from the changes induced in the depletion-layer width of the ZnO nanoparticles that bridge ZnO nanowires resulting from THMA ligand binding to the surface of the particle coating. The heightened response and selectivity to the NO_2 target are positive results arising from the coating of these ZnO nanowire sensors with organic-SAM-functionalised ZnO nanoparticles.

Introduction

Semiconductor gas sensors have been extensively investigated for practical applications such as the detection of gas leaks and the environmental monitoring of gaseous pollutants. Since the earliest reports in this field, research efforts were focussed on improving gas response, selectivity, and sensor stability, and on their practical use, yet further innovations in the semiconductor gas-sensing field are still in demand [1-3]. Impedance-semiconductor gas sensors typically operate at temperatures greater than 200 °C [4,5]. High operating temperatures are generally required to maximise the sensor response to target gases, either to activate the semiconductor surface towards chemisorption or else to ensure heterogeneous catalysis of a high proportion of target gas molecules at the sensor surface. High-temperature operation also ensures the complete desorption of gaseous species following transduction. Maintaining a semiconductor gas sensor at a stable temperature higher than 200 °C requires a stable and consistent power source, drawing on a high operating voltage and current. For certain applications maintaining the high operating temperature can have drawbacks, especially when high sensor power consumption is undesirable, such as when photovoltaics are the desired power source. A case in point is the monitoring of gas emissions remotely, in outdoor environments where mains power may be unavailable. For this application, highly responsive, low-power and thus low-temperature gas sensors would be advantageous.

Both the structural and physicochemical properties of metal-oxide films utilised in solid-state chemical sensors have proven to strongly affect the gas response in these devices. Not only do simple structural elements such as grain size play a significant role in gas response, but also crystallite shape, crystallographic orientation, film agglomeration, phase composition and surface architecture [5]. In terms of the targeted optimisation of gas-sensor characteristics, surface engineering is potentially a powerful instrument for the control of gas response. To date, designers have mainly focused on doping the metal oxide by means of metal catalyst nanoparticle additives, and decreasing the crystallite (grain) sizes or intercrystallite neck dimensions to the nanometre scale. Chemical functionalisation as an approach to modify the response of semiconductor surfaces towards different gases has not been examined to anywhere near the same level of detail. Coating of the semiconductor with a sensitising molecule layer could enhance surface reactions or modify the surface chemistry and, hence, improve sensor sensitivity and specificity to a particular gas. Although such chemical functionalisation of impedance-based gas sensor surfaces is often avoided due to the possibility of poisoning effects which may occur, akin to poisoning of heterogeneous catalyst surfaces, functionalisation can sometimes have a positive effect [6]. Self-assembled monolayers (SAMs) have been shown to effectively modify the surface physics and chemical properties of metals and metal-oxide materials [6]. Previously, when foreign receptors were introduced into MOx sensor grains, sensitizing actions were observed, particularly when they modified the work function and surface space-charge layer of the sensor material [7]. Another significant effect that may arise through organic SAM functionalisation of the semiconductor surface is a chemical effect. Since only the outermost 5 Å of a surface completely determines its chemical properties, that is whether it is hydrophobic, hydrophilic, acidic, or basic for example, surface functionalisation with an organic molecule may be expected to change the relative rates of diffusion of gaseous species to the surface of the semiconductor and alter the reaction processes that occur. An organic SAM can act as a functional group in nanowire chemical and biological sensors [6,8]. In terms of sensor response, although a decreased number of “active” sites for chemisorption may arise through chemical functionalisation by an organic layer, the effect may be offset by increased rates of gas decomposition or reduced interference caused by moisture or other species present in a gas stream. It should be noted that since chemisorption involves electronic charge transfer, functionalisation of the surface of a metal-oxide semiconductor gas sensor with an organic monolayer will strongly influence the electronic properties of the surface. Transfer of electron density into the semiconductor will reduce the depletion layer, which is an effect that is likely to modify the chemiresistor response significantly [3].

ZnO is one of the most widely studied materials, due to its promising optical, optoelectronic and piezoelectric properties [9,10]. Furthermore, ZnO materials can be reliably synthesised in a variety of different nanostructured forms, such as nanowires, nanoribbons, nanobelts and as tetrapods [11], and their potential use in NO_2 gas sensing in these forms is well known [12,13]. In this study we investigated the effects that two very different types of organic ligands imposed on the sensitivity and response of semiconductor gas sensors based on zinc oxide nanowires. Significantly, we chose to examine the response of *the same* ZnO nanowire sensors to target gases before and after functionalisation rather than to compare different sensors prepared in the same batch, in order to eliminate the possibility of differences in response caused by sensor batch variations being misconstrued as a result of the functionalisation process. The first ligand studied was dodecanethiol (DT), which can readily form a self-assembled monolayer at the ZnO surface simply by exposure of the nanowires to an ethanolic solution containing the thiol. The long DT hydrocarbon chains were expected to create a strongly hydrophobic surface. Similarly ZnO nanowire sensors were functionalised by tris(hydroxymethyl)aminomethane (THMA), and the response of THMA-functionalised sensors was compared to that of the unfunctionalised ZnO nanowire devices. Since the working principle of an oxide-semiconductor gas sensor involves the receptor function that is played by the surface of each oxide grain and the transducer function that is played by each grain boundary [3], the self-assembly of DT and THMA monolayers on the surface of the oxide was expected to modify both functions. The performances of both ZnO nanoparticle (ZnO NP) sensors and also ZnO nanowire (ZnO NW) sensors coated with a low density of DT-, or THMA-functionalised ZnO nanoparticles were examined and compared to nanowire-only devices to test the influence of grain-boundary effects on the gas response. We investigated the chemiresistor response towards ammonia, nitrous oxide and nitrogen dioxide.

Results and Discussion

The morphology, surface roughness and evenness-of-coating of the ZnO nanowire sensors were examined by scanning electron microscopy. SEM images of each sensor form are given in Figure 1. The SEM image in Figure 1a is of a drop-cast nanoparticle-based sensor. The nanoparticle films formed as high-surface-area, porous coatings, which were evenly deposited over the sensor support, including the metal contacts. When these sensors were tested for gas response, however, the conductivity of the ZnO NP films, as produced, proved too low to be useful in the gas-sensor configuration tested. The ZnO matrix deposition process clearly led to agglomeration of the primary ZnO particles into aggregates, some with micrometre dimensions. Such agglomeration of small crystallites into larger masses tends to reduce the gas permeability through the matrix [14]. It also increases the influence of the interagglomerate contact resistance on the gas response of the sensors. Analysis of transmission electron microscope images of these ZnO materials reveals that the primary particle size of these nanoparticle-based sensors was in the range 1 to 6 nm (Figure 2), yet the background resistance of these sensor elements was very high, presumably due to inter-agglomerate contact effects [14]. Strong agglomeration thus appeared to offset any of the advantages in terms of sensitivity that could be obtained through the use of small ZnO grains (crystallites) with these sensors. In the case of ZnO nanoparticle sensors in the size regime used here, it has been demonstrated previously that a significant response to low (2–10 ppm) NO_2 concentrations requires an operating temperature of 290 °C to elicit the

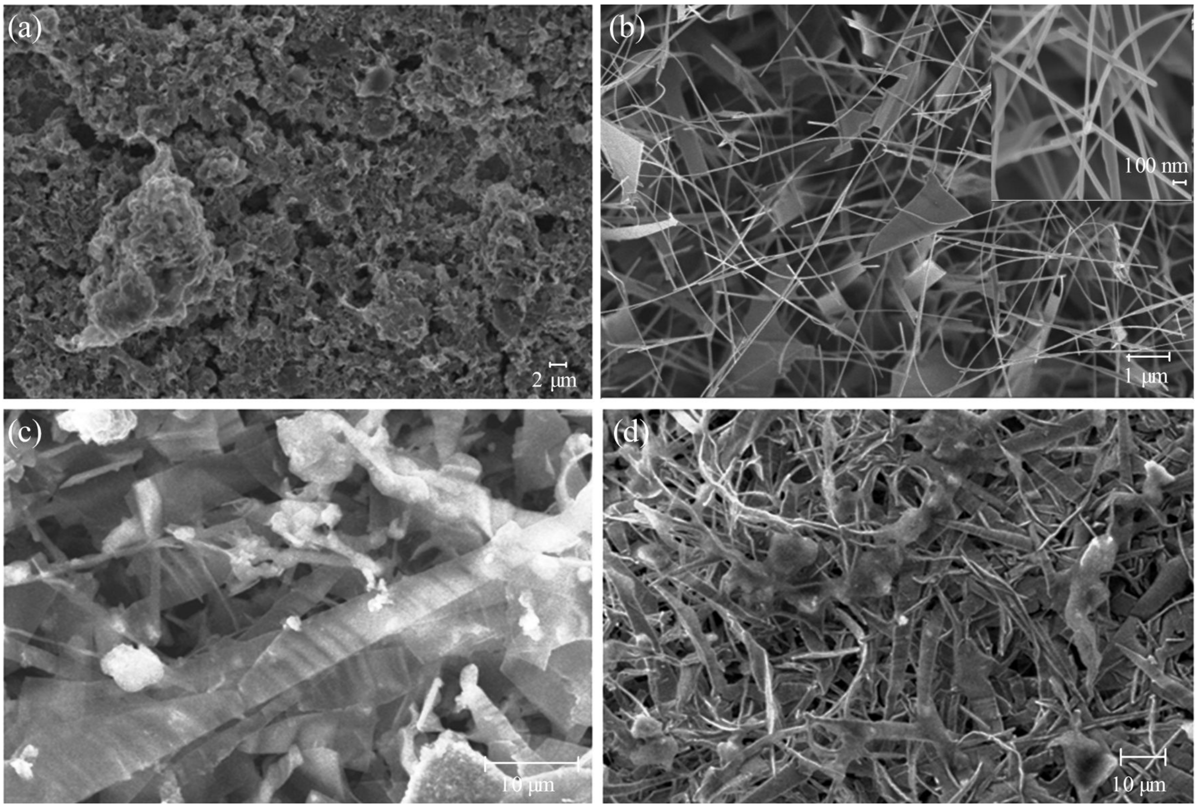

Figure 1: Scanning electron microscopy images of (a) the drop-cast ZnO nanoparticle sensor surface; (b) the pure ZnO nanowire sensor surface (inset: higher magnification FESEM image of ZnO NWs); (c) DT-ZnO NP + ZnO nanowire sensor surface; and (d) THMA-ZnO NP + ZnO nanowire sensor surface (note the change in scale).

maximum response of the material [15]. Since we were examining the potential useful effects that a ligand shell surrounding the nanoparticles could have upon the response to NO_2 at 190 °C, it was unsurprising that only a very low transient response was observed with the nanoparticle sensors.

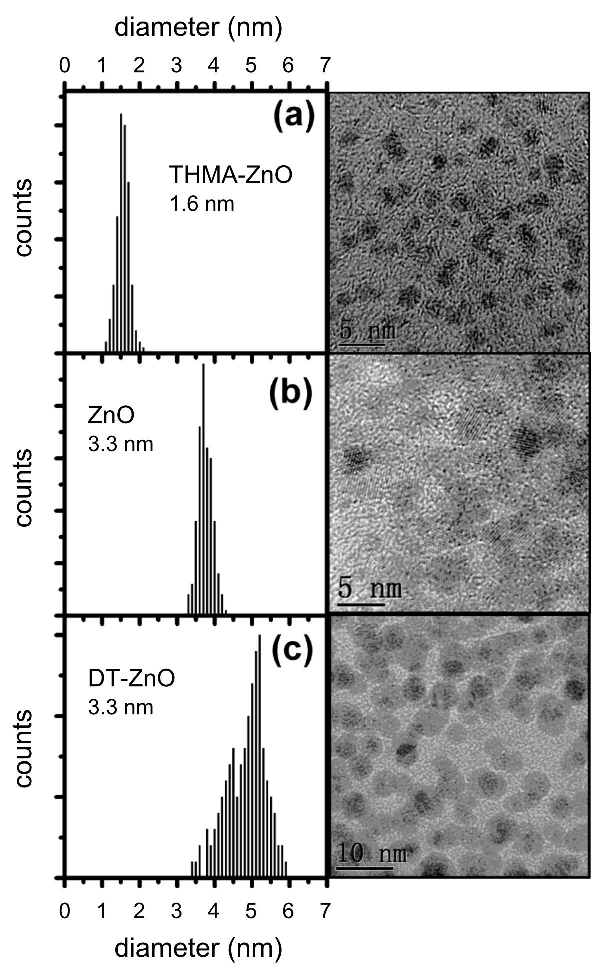

Figure 2: Transmission electron microscopy images and size-distribution analyses of ZnO nanocrystals after heating under reflux in ethanol for 30 min, for (a) THMA-functionalised ZnO nanoparticles; (b) ZnO NPs; and (c) DT-functionalised ZnO NPs.

In contrast to the case of drop-cast ZnO nanoparticle sensors, the nanowire samples (Figure 1b) were evenly deposited as an open structure, containing in this case a mixture of thin sheets and nanowire filaments. The individual nanowires typically had dimensions of 5–10 µm in length and approximately 50 nm in diameter (see inset to Figure 1b). The low resistivity of these devices, as made, arises from the high degree of crystallinity and the high aspect ratio of the nanowires. This particular structure thus offers preferential, low-resistance paths to charge carriers, with percolative conduction paths featuring a much-reduced number of crystallite interfaces with respect to their nanoparticle counterparts. Organic functionalisation of nanowire sensors identical to that shown in Figure 1b had no visible effect on the nanowire structures as seen by FESEM (either with DT or THMA). Finally, the SEM images of nanoparticle-coated samples in Figure 1c and Figure 1d show that the pure ZnO-based samples were effectively coated, yielding thicker, functionalised ZnO NP filaments and platelets. In each case ZnO NP agglomerates were also attached to the nanowire samples, sometimes contacting several plates or wires.

Ex situ functionalisation of NP- and NW-powder ZnO samples by either DT or THMA was confirmed by FTIR measurements. The FTIR spectra given in Figure 3 are of a ZnO nanowire sensor sample and samples that had been exposed to either 10 mM dodecanethiol or THMA solution for 24 h, followed by repeated washing with ethanol in order to remove possible excess surface-adsorbed organics. These samples were then dried in air. Evidence for successful the functionalisation of ZnO by DT can be seen by comparing the FTIR spectra in Figure 3. In Figure 3b, FTIR absorption peaks originating from the dodecanethiol C–H symmetric and asymmetric stretch vibrational modes can be clearly seen at 2850 and 2920 cm^{-1}, respectively, which indicates that functionalisation of ZnO by DT in this way was successful. The dodecanethiol peaks were completely absent in the pure ZnO FTIR spectrum of Figure 3. The presence of a C–O stretching peak near 1100 cm^{-1} and an N–H peak near 3300 cm^{-1} in the spectrum of a THMA-functionalised ZnO nanowire sensor Figure 3 also revealed that THMA adsorbed to the ZnO nanowires.

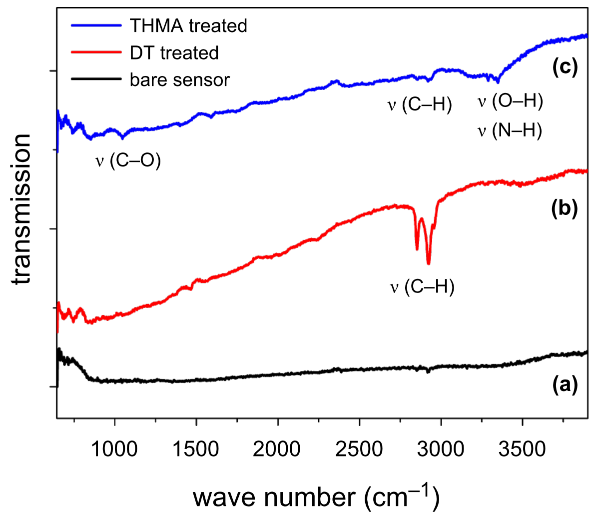

Figure 3: FTIR spectra of (a) pure ZnO nanowire sensor; (b) dodecanethiol-coated ZnO nanowire sensor; and (c) THMA-coated ZnO nanowire sensor.

The FTIR evidence for the successful functionalisation of ZnO sample surfaces by DT and THMA was confirmed by both XPS and thermogravimetry. The XPS survey of the DT-functionalised ZnO NW sensor surfaces given in Figure 4a provides further evidence for the successful chemisorption or ligand attachment of dodecanethiol to the ZnO NW surfaces. A peak corresponding to the Zn–S bond between the dodecanethiol ligand and the ZnO surface could readily be distinguished at 164.4 eV with these samples, while sulfur peaks in the XPS spectrum of the unfunctionalised sensors were completely absent. Similarly THMA-functionalisation led to a multicomponent nitrogen peak, which could be fitted to the C–N bond in THMA occurring at 400.2 eV and also a N–Zn bond between THMA and ZnO at 401.7 eV, as shown in Figure 4b. Similar amine-based peaks were also absent from the XPS spectra originating from pure ZnO NW sensor surfaces. The thermogravimetric results given in Figure 5 were also used to determine the temperature range that the dodecanethiol-coated or THMA-coated sensors could operate in without there being a significant breakdown of the organic monolayer coating. Inspection of Figure 5 reveals that only minor mass-loss peaks occurred between room temperature and 200 °C, corresponding to desorption of surface-adsorbed water and species such as surface acetate ligand residues, which remained after the zinc oxide synthesis and washing procedures [16]. The major mass-loss peak, accounting for 40% of the original mass, presumably corresponding to desorption and break down of the dodecanethiol monolayer, occurred at approximately 225 °C. This desorption temperature for dodecanethiol is significantly lower than that reported by Sadik et al. who used XPS to investigate the functionalization of O-terminated (desorption occurred at 350 °C) and Zn-terminated (400 °C desorption) zinc oxide surfaces [17]. The difference in these values can be ascribed to the fact that our materials were prepared in nanocrystalline

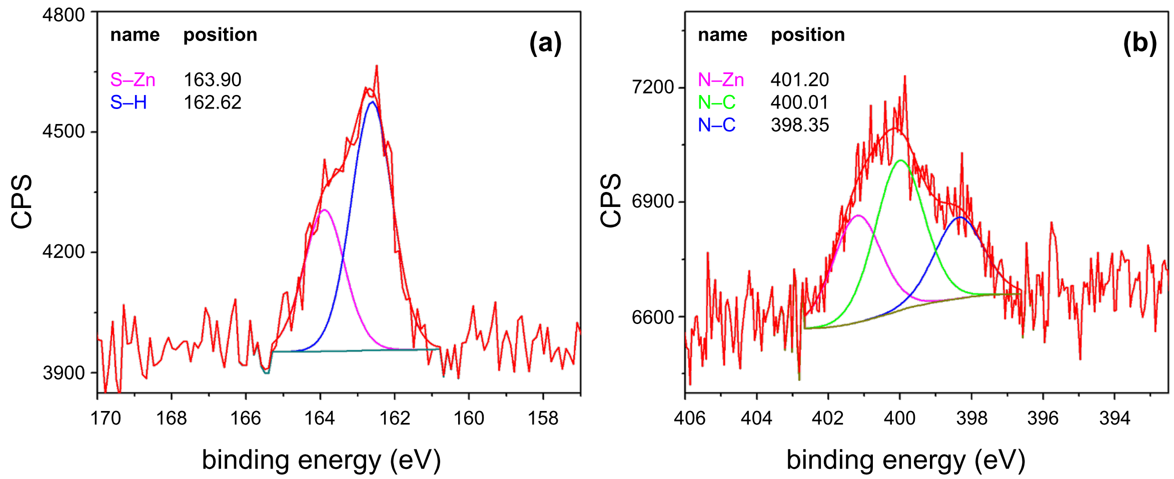

Figure 4: XPS spectra of (a) the sulfur peak of DT-functionalised ZnO NW sensor surface and (b) the amide peak of THMA-functionalised ZnO NW sensor surface.

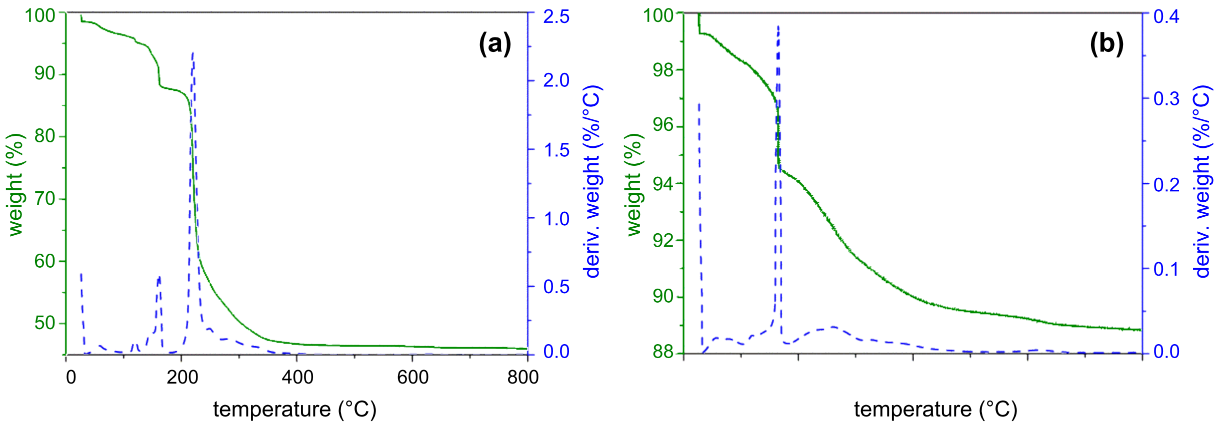

Figure 5: TG and DTG of (a) DT-coated and (b) THMA-coated ZnO obtained in air at 5 °C·min^{-1}.

rather than single-crystal form and therefore a range of different ZnO crystal surfaces were exposed rather than a single surface, but more importantly, the fact that the XPS study was performed in ultrahigh vacuum rather than in dry air. Taking the TG results into account, a sensor operating temperature of 190 °C was chosen for all gas-response tests.

Gas sensing measurements for the various ZnO samples with different morphologies and compositions were performed for the gases ammonia, nitrous oxide and nitrogen oxide. The sensors were maintained at the operating temperature of 190 °C in dry air until a stable sensor resistivity was reached, then the sensors were each exposed, in turn, to ammonia, nitrogen dioxide and nitrous oxide. The gas response results for the pure ZnO nanowire samples, and also after the same sensor surface had been functionalised by THMA, are both given in Figure 6. The results for the pristine and THMA-functionalised ZnO nanowire sensors exhibited similar behaviour upon exposure to the different gases. In both cases there was almost no response upon exposure to the reducing gas NH_3. Likewise these sensors did not appear to show a significant response when exposed to nitrous oxide, even for high concentrations of 300 ppm of N_2O in the gas stream. In contrast to these results for NH_3 and N_2O, exposure of the nanowire sensors to the oxidising gas NO_2 produced a significant and reproducible response. This result is consistent with the results obtained with other metal-oxide gas sensors: NO_2 is in general much easier to detect than NH_3 and N_2O; NO_2 is frequently sensed at a ppb level, NH_3 at a ppm level, see for example Ponzoni et al. [18], while N_2O is usually sensed at a hundreds of ppm level [19]. So, our results with pure ZnO here clearly reflect the different reactivity of these gaseous molecules with metal oxides. Furthermore, the response of pure ZnO to NH_3 is usually only enhanced at high temperature (around 300 °C) [20], but this is not compatible with the organic coating, which would be damaged/desorbed at such a high temperature. ZnO and THMA-coated ZnO nanowire sensors both readily detected NO_2 down to concentrations of 2 ppm. To confirm that the response of the nanowire samples to NO_2 was reproducible and that no poisoning effects occurred at the sensor surfaces, after exposure to N_2O, the sensors were re-exposed to NO_2. It can be seen by inspection of Figure 6 (a), that the response to NO_2 was unchanged.

The gas response of the *same* ZnO sensors pre- and post-functionalisation with THMA was significant and could be readily measured, although there appeared to be no clear indication of a significant change in NO_2 sensitivity after THMA functionalization. Furthermore, we note that the baseline conductivity of these sensors was not significantly changed. In contrast, in the case of the DT-functionalised sensors, surface reaction with the thiol (confirmed by FTIR) raised the conductivity of each individual sensor above the measurement range of our instrument (which corresponds to a minimum conductance value of G_{max} = 10 mS). We conclude from this that chemisorption of the thiol significantly increased the density of electrons present in the ZnO NW conduction band. We note that ZnO NW sensors modified by DT-functionalised or THMA-functionalised ZnO NPs showed a small increase in baseline conductivity, as can be seen in Table 1.

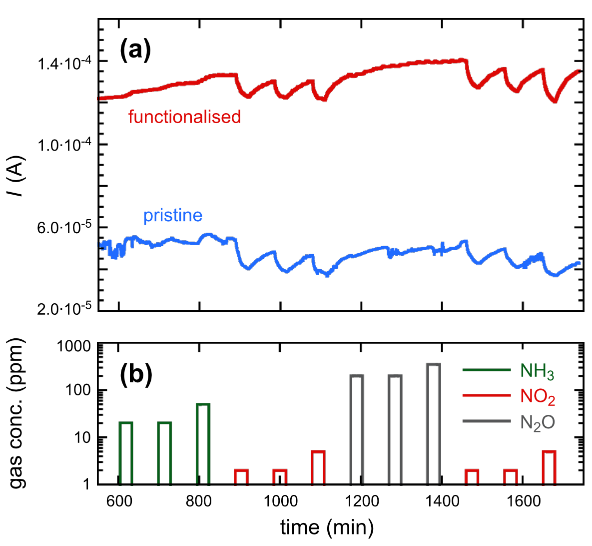

Figure 6: Dynamic response of the same ZnO nanowire sensor, (a) before and after THMA functionalization and (b) during exposure to different concentrations of NH_3, N_2O and NO_2.

Overall, the pure and THMA-functionalised ZnO NW sensors proved to be effective for the detection of the oxidising gas NO_2 (Figure 6). It is well known that ZnO adsorbs atmospheric oxygen to form adsorbed O_2^-, O^- and O^{2-} species and that these electrons are drawn from the ZnO conduction band as a consequence of this adsorption. Adsorbed O_2^- is stable below 100 °C, O^- is the adsorbed species in highest concentration between 100 and 300 °C, while O^{2-} is prevalent above 300 °C [21,22]. At the sensor operating temperature of 190 °C, the strongly oxidising gas NO_2 also depletes ZnO of electrons upon chemisorption, leading to a reduced conductivity after the gas exposure, according to the following process:

$$NO_2(g) \rightleftarrows NO_2(ads) \tag{1}$$

$$NO_2(ads) + e^- \rightleftarrows NO_2^-(ads) \tag{2}$$

One approach to the use of organic SAMs to enhance gas response is to use them to generate extra oxygen vacancies and

Table 1: Average response of all ZnO NW samples upon exposure to 2 ppm NO_2.

code	before functionalisation	G_0 (S)	after functionalisation	G_0 (S)	$G_{0,after}/G_{0,before}$
3a	pure	$2.53 \cdot 10^{-3}$	+ DDT	out of range	(>3.95)
3b	pure	$4.66 \cdot 10^{-3}$	+ DDT	out of range	(>2.15)
3c	pure	$9.87 \cdot 10^{-3}$	+ DDT	out of range	(>1.01)
3d	pure	$4.48 \cdot 10^{-3}$	+ THMA	$6.99 \cdot 10^{-3}$	1.56
3e	pure	$4.52 \cdot 10^{-3}$	+ THMA	$7.67 \cdot 10^{-3}$	1.70
7a	pure	$2.57 \cdot 10^{-4}$	+ THMA	$6.13 \cdot 10^{-4}$	2.38
7b	pure	$2.06 \cdot 10^{-4}$	+ ZnO NP + DDT	$1.80 \cdot 10^{-4}$	0.87
7c	pure	$1.83 \cdot 10^{-4}$	+ ZnO NP + DDT	$3.15 \cdot 10^{-4}$	1.72
8a	pure	$9.25 \cdot 10^{-5}$	+ ZnO NP + DDT	$1.41 \cdot 10^{-4}$	1.52
8b	pure	$3.40 \cdot 10^{-4}$	+ ZnO NP + THMA	$4.29 \cdot 10^{-4}$	1.26
8c	pure	$8.56 \cdot 10^{-5}$	+ ZnO NP + THMA	$1.30 \cdot 10^{-4}$	1.51
8d	pure	$4.48 \cdot 10^{-5}$	+ ZnO NP + THMA	$8.07 \cdot 10^{-5}$	1.80

defects in the MOx sensor surface. This has been successfully demonstrated previously for the case of a ZnO nanobelt oxygen gas sensor, by heating the sensor to temperatures at which desorption and decomposition of the organic SAM occurred [6]. This is not likely to be the case here, however. The approach in this study was slightly different. The sensors were heated close to the SAM decomposition temperature, which was confirmed using TG (Figure 5), but not so far that significant SAM decomposition was likely to occur. Temperature-programmed desorption (TPD) experiments have shown that chemisorbed thiolates remain stable on the ZnO surface up to approximately 500 K (227 °C) [23]. Similarly for the case of amines like THMA, adsorption leads to a Lewis acid/base interaction [24], and our TG results show that for THMA, no significant decomposition or desorption occurred at 190 °C. Since a thick and impervious monolayer coating would prevent any contact between the gas and the sensor surface, leading to little to no response, the organic layer must in each case be porous enough to allow gas molecules to pass to the semiconductor surface and to interact with surface-adsorbed oxygen according to the mechanisms outlined in Equation 1 and Equation 2. There must also be enough defects or reactive sites at the semiconductor surface initially, for the THMA molecules (and presumably for DT molecules) to react at defects or reactive sites and inject negative charge carriers into the material. Thus functionalisation has the opposite effect to O_2 (and NO_2) adsorption. Electrons are injected into the conduction band of the semiconductor by THMA, just as they are for DT, albeit to a lesser extent.

The dynamic responses of the THMA-functionalised ZnO-nanowire-based chemiresistor gas sensors are given in Figure 7a and Figure 7b, as operated at the comparatively low temperature of 190 °C. It is interesting to note that all three of the replicas of these sensors possessed a consistent enhanced sensitivity toward NO_2 after they had been coated with the nanoparticles and THMA. This is of interest from a practical point of view due to the enormous number of different types of organic molecules that could in principle be used to enhance sensor response. Nanoparticle size and density-of-coverage are other avenues that could be explored in this context. A consistent enhancement of response with these capped nanoparticle-functionalised resistive gas sensors toward particular gases, may allow them to operate at lower temperatures and so reduce the power consumed by these devices. Perhaps just as intriguing as the potential practical applications of this type of coating, is the possible mechanism by which the enhanced gas response was achieved, by attachment of the particles to the surface of the sensor.

Of the two organic monolayers investigated, DT and THMA, THMA was likely to be the stronger capping ligand for ZnO, as demonstrated by the smaller nanoparticle size and nanoparticle distributions produced when THMA was introduced to the zinc acetate synthesis route (Figure 2). THMA is clearly able to displace any surface adsorbed acetate on the ZnO NPs and stifle further particle growth during synthesis. This being the case, THMA is also likely to bind strongly to ZnO nanowire surfaces. The presence of the three hydroxyl groups in THMA ensures multidentate binding to the ZnO surface and is likely to facilitate hydrogen-bonding type interactions with surface-adsorbed hydroxyls under our surface-functionalisation (and gas-testing) conditions. In terms of an electronic effect, THMA (and DT) binding led to an increase in free-electron carrier concentration in ZnO, reflected in the increased conductivity of the functionalised nanowire gas sensors (Table 1). In terms of gas response, there are several ways in which a gas sensor can achieve enhanced response in the case of ZnO nanowire sensors. For

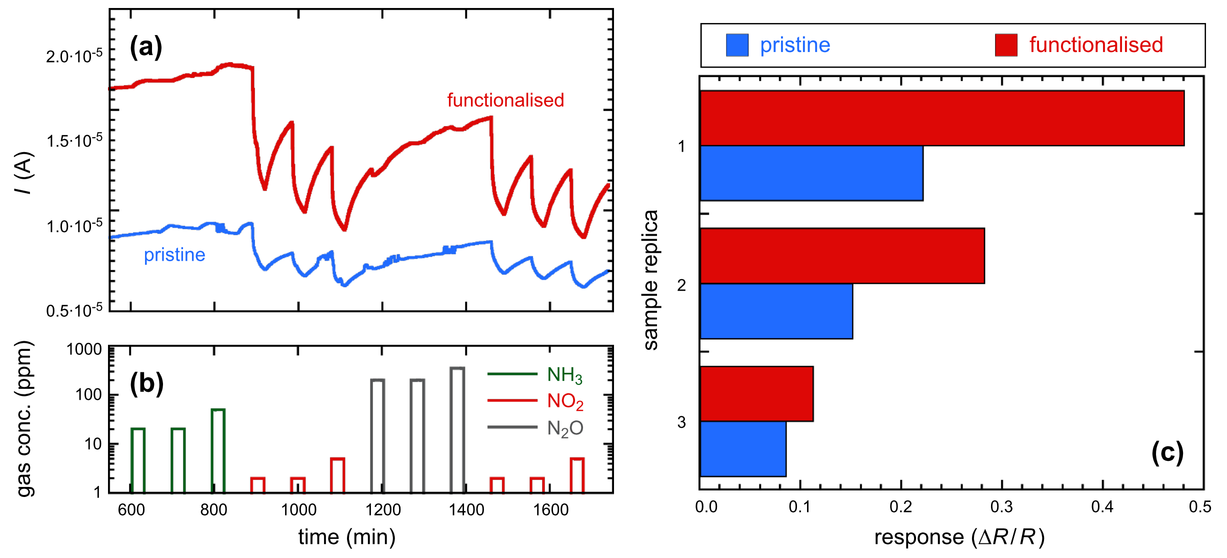

Figure 7: Dynamic response of the same ZnO nanowire sensor, (a) before and after coating with ZnO nanoparticles and THMA; (b) during exposure to different concentrations of NH_3, N_2O and NO_2; and (c) response $\Delta R/R$ exhibited by three sensor replicas before and after THMA functionalization to 2 ppm of NO_2.

instance it is well known that gas sensitivity to NO_2 is linearly proportional to oxygen-vacancy-related defects [25]. THMA-SAMs appeared to have little effect on $\Delta R/R$ with NO_2 exposure, so in this case the surface-ligand binding did not appear to affect sensor response by changing this parameter significantly. Since the gas-sensor configuration with the most enhanced gas response was the THMA-ZnO-nanoparticle-coated configuration, it appears that some property arising through the coating with the nanoparticles influenced the gas response to NO_2 in a positive way, modulating the response by increasing the resistance through the ZnO nanowire contacts.

A reasonable explanation for this can be suggested upon comparison of Table 1 with the results shown in Figure 6 and Figure 7. Due to the reduced size, about 1.3 nm, which is comparable with the depth of the depletion region, the nanoparticles are likely to be fully depleted of electrons, different to the case of nanowires, which feature a depleted surface layer but also possess an unaltered “bulk” core due to their much larger diameter (about 50 nm, from Figure 1 inset). Looking at the overall results obtained with all the sensor replicas, as shown in Table 1, the more effective baseline conductance increase obtained after coating with THMA-ZnO nanoparticles compared to the THMA-coating, can be explained in terms of a preferential charge-carrier injection from THMA into depleted nanoparticles instead of nanowires. On the other hand, exposure to NO_2 would modify the charge-carrier equilibrium between THMA and the ZnO nanowire, with THMA injecting additional carriers to balance the effects of NO_2, thus quenching, in part, the overall sensor response to that gas. Following this scheme, it is not surprising that nanowires feature an almost unaltered response to NO_2 after being coated with THMA. In the case of the THMA-ZnO nanoparticles coating, the presence of such small nanoparticles is expected to mitigate such a quenching effect by preventing a large charge injection into nanowires. The overall result from the THMA- and nanoparticles-functionalised cases is a response increase in these samples, consistent with the results shown in Figure 7.

Conclusion

In this study the dynamic gas response of resistive gas sensors formed from functionalised ZnO nanowires was examined. The response of the nanowire sensors when functionalised with organic molecule layers of dodecanethiol, tris(hydroxymethyl)aminomethane and also with DT, or THMA-functionalised ZnO nanoparticles was compared for ammonia, nitrous oxide and nitrogen dioxide. Of the three gases examined, only the reducing gas NO_2 generated a significant response in these sensors. Significantly, rather than averaging the results of several different sensors made in a single batch, the responses of the *same* individual sensors were compared pre- and post-functionalisation. Any changes in response could thus be attributed to the functionalisation step. Apart from a slight change in baseline conductivity, the gas response $\Delta R/R$ of DT-functionalised NP-modified ZnO NW sensors did not show any significant enhancement (or poisoning effect) when exposed to NO_2. In contrast to this, ZnO nanowire sensors coated with a thin layer of very small THMA-functionalised nanoparticles (average nanoparticle diameter 1.3 nm) elicited up to 2× enhancement in $\Delta R/R$ toward very low, 2 ppm, concentrations of NO_2 following the nanoparticle-coating step. The results obtained demonstrate that the modification of metal-oxide surfaces, such as ZnO nanowires, with nanostructured materials containing organic monolayers, can tune the electronic and interfacial properties of these materials, and in the case of gas sensors, has the potential to enhance the gas response significantly.

Experimental

Zinc oxide nanowire films were grown on alumina substrates for sensing tests (2 mm × 2 mm × 0.25 mm). The ZnO nanowires were grown from the vapour phase by using the evaporation–condensation technique. Pure Zn precursor powder was placed at the centre of an alumina tube and then the tube temperature was raised above the Zn decomposition temperature of 600 °C. A controlled flow of inert argon gas was maintained during the decomposition and the overall pressure was maintained at several hundreds of mbar. The temperature gradient downstream of the gas flow promoted condensation of metal cations on clean alumina substrates, which interacted with residual oxygen to give ZnO nanowires [13]. The stabilised samples were then provided by interdigitated Pt electrodes deposited by RF magnetron sputtering, while on the back side a Pt meander was deposited to act as heater (by Joule effect) and temperature sensor. Ex situ functionalisation of dodecanethiol-coated nanowire samples was accomplished by immersing the completed sensors for 24 h in a 10 mM solution of dodecanethiol in ethanol. Tris(hydroxymethyl)aminomethane-functionalised ZnO nanowires and nanoparticles were similarly functionalised by immersing the completed sensors for 24 h in 10 mM ethanolic solutions. The functionalisation of ZnO by this procedure was confirmed by FTIR and XPS measurements. Prior to functionalisation with ligands or ligand-capped ZnO nanoparticles and the gas-sensing tests, all nanowire samples were stabilised by annealing at 450 °C for 25 d.

Ligand-capped ZnO NPs were all synthesised by the wet-chemical method. All were produced by hydrolysis of anhydrous zinc acetate ($Zn(CH_3CO_2)_2$ or $Zn(Ac)_2$, 99.99%), in the presence of base (sodium hydroxide) in absolute ethanol. Ligands *n*-dodecanethiol ($C_{12}H_{25}SH$, or DDT, 99%) and tris(hydroxymethyl)aminomethane ($C_4H_{11}NO_3$ or THMA, 99%) were added as required. All chemicals were used as received from Aldrich without further purification or distillation. For example, in a typical synthesis, $Zn(Ac)_2$ (0.5 mmol, 92 mg) and THMA (0.2 mmol, 24 mg) were added into absolute ethanol (30 mL) under stirring. Then the mixture was heated at around 80 °C for 1 h to dissolve $Zn(Ac)_2$ and THMA. Following complete dissolution of the precursors, a NaOH/ethanol solution (20 mL, 0.05 M) was injected into the hot solution and then the mixture was heated under reflux for a further 72 h. The obtained cloudy solution was centrifuged and rinsed with deionized water and ethanol to remove byproducts. For the synthesis of DT-ligand-capped ZnO samples, THMA was simply replaced by DT. For comparison, bare ZnO NPs were synthesised in the same procedure without the use of capping ligands. The morphology and size of all nanoparticle samples was determined by transmission electron microscope (TEM, JEOL-2100) with an accelerating voltage of 200 kV. For TEM experiments, the specimens were prepared by deposition of a dilute solution of the colloid onto a carbon-coated copper grid and drying at room temperature.

Thermogravimetric (TG) measurements were performed on an SDT 2960 TA® Instruments model at 5 $°C \cdot min^{-1}$ over a temperature range from 24 °C (room temperature) up to 1000 °C under a dry air flow of 100 $cm^3 \cdot min^{-1}$. Derivative thermogravimetric (DTG) curves were generated with approximately 2000 points. Samples were characterised by scanning electron microscopy (SEM) (Zeiss SUPRA 40). FTIR measurements on organic-functionalised ZnO were performed at room temperature by using a Spectrum 1000 FTIR spectrometer. X-ray photoelectron spectroscopy (XPS) measurements of ZnO nanowires were measured before and after functionalisation by either DT or THMA, to confirmed the presence of the ligands on the ZnO nanowire surfaces after the functionalisation, washing and low-temperature anneal had been performed, but prior to gas sensing, by using a Kratos Axis ULTRA XPS incorporating a 165 mm hemispherical electron-energy analyser. Monochromatic Mg Kα X-rays (1253.6 eV) at 150 W (15 kV, 10 mA) were used as the incident radiation. Multiplex high-resolution scans were achieved at an analyser pass energy of 20 eV, in steps of 0.10 eV.

Characterisation of the electrical and gas-sensing properties was carried out using a two-probe technique by applying a constant 0.2 V bias to the films and measuring the through current with a picoammeter. Gas-sensing measurements were carried out by the flow-through method, working at a constant flow of 300 sccm in a thermostatic sealed chamber at room pressure under constant-humidity conditions (RH = 30% @ 20 °C). Controlled gas mixtures were obtained by using mass-flow controllers to mix flows from certified bottles. Sensor response was calculated as $(R_{gas} - R_{air})/R_{air}$, denoted as $\Delta R/R$, and $(G_{gas} - G_{air})/G_{air}$, denoted as $\Delta G/G$ for oxidizing (N_2O, NO_2) and reducing gases (NH_3), respectively. R and G represent the measured electrical resistance and conductance of the sample. Sensor response was measured at 190 °C operating temperature. We established through the TG measurements of functionalised ZnO samples, that the degradation of the organic capping layer of the nanowires and nanoparticles at this operating temperature was minimal.

Acknowledgements

The authors acknowledge the financial support of the Queensland Government through the Queensland Smart State Futures Program NIRAP (National and International Research Alliances Program). ERW acknowledges the QUT Faculty of Science for financial support and the Queensland Government for a Queensland International Fellowship. JC gratefully acknowledges the China Scholarship Council for a PhD scholarship in pursuit of this work.

References

1. Seiyama, T.; Kato, A.; Fujiishi, K.; Nagatani, M. *Anal. Chem.* **1962,** *34,* 1502–1503. doi:10.1021/ac60191a001
2. Taguchi, N. Method for making a gas-sensing element. U.S. Patent 3,625,756, Dec 7, 1971.
3. Yamazoe, N.; Sakai, G.; Shimanoe, K. *Catal. Surv. Asia* **2003,** *7,* 63–75. doi:10.1023/A:1023436725457
4. Yamazoe, N. *Sens. Actuators, B* **1991,** *5,* 7–19. doi:10.1016/0925-4005(91)80213-4
5. Korotcenkov, G. *Sens. Actuators, B* **2005,** *107,* 209–232. doi:10.1016/j.snb.2004.10.006
6. Lao, C.; Li, Y.; Wong, C. P.; Wang, Z. L. *Nano Lett.* **2007,** *7,* 1323–1328. doi:10.1021/nl070359m
7. Yamazoe, N.; Fuchigami, J.; Kishikawa, M.; Seiyama, T. *Surf. Sci.* **1979,** *86,* 335–344. doi:10.1016/0039-6028(79)90411-4
8. Cui, Y.; Zhong, Z.; Wang, D.; Wang, W. U.; Lieber, C. M. *Nano Lett.* **2003,** *3,* 149–152. doi:10.1021/nl025875l
9. Wang, Z. L.; Song, J. *Science* **2006,** *312,* 242–246. doi:10.1126/science.1124005
10. Wang, X.; Zhou, J.; Song, J.; Liu, J.; Xu, N.; Wang, Z. L. *Nano Lett.* **2006,** *6,* 2768–2772. doi:10.1021/nl061802g
11. Djurišić, A. B.; Choy, W. C. H.; Roy, V. A. L.; Leung, Y. H.; Kwong, C. Y.; Cheah, K. W.; Gundu Rao, T. K.; Chan, W. K.; Fei Lui, H.; Surya, C. *Adv. Funct. Mater.* **2004,** *14,* 856–864. doi:10.1002/adfm.200305082
12. Forleo, A.; Francioso, L.; Capone, S.; Siciliano, P.; Lommens, P.; Hens, Z. *Sens. Actuators, B* **2010,** *146,* 111–115. doi:10.1016/j.snb.2010.02.059
13. Sberveglieri, G.; Baratto, C.; Comini, E.; Faglia, G.; Ferroni, M.; Ponzoni, A.; Vomiero, A. *Sens. Actuators, B* **2007,** *121,* 208–213. doi:10.1016/j.snb.2006.09.049
14. Korotcenkov, G.; Macsanov, V.; Tolstoy, V.; Brinzari, V.; Schwank, J.; Faglia, G. *Sens. Actuators, B* **2003,** *96,* 602–609. doi:10.1016/j.snb.2003.07.002
15. Shouli, B.; Liangyuan, C.; Jingwei, H.; Dianqing, L.; Ruixian, L.; Aifan, C.; Liu, C. C. *Sens. Actuators, B* **2011,** *159,* 97–102. doi:10.1016/j.snb.2011.06.056
16. Sakohara, S.; Tickanen, L. D.; Anderson, M. A. *J. Phys. Chem.* **1992,** *96,* 11086–11091. doi:10.1021/j100205a084
17. Sadik, P. W.; Pearton, S. J.; Norton, D. P.; Lambers, E.; Ren, F. *J. Appl. Phys.* **2007,** *101,* 104514. doi:10.1063/1.2736893
18. Ponzoni, A.; Comini, E.; Ferroni, M.; Sberveglieri, G. *Thin Solid Films* **2005,** *490,* 81–85. doi:10.1016/j.tsf.2005.04.031
19. Kanazawa, E.; Sakai, G.; Shimanoe, K.; Kanmura, Y.; Teraoka, Y.; Miura, N.; Yamazoe, N. *Sens. Actuators, B* **2001,** *77,* 72–77. doi:10.1016/S0925-4005(01)00675-X
20. Sarala Devi, G.; Bala Subrahmanyam, V.; Gadkari, S. C.; Gupta, S. K. *Anal. Chim. Acta* **2006,** *568,* 41–46. doi:10.1016/j.aca.2006.02.040
21. Sadek, A. Z.; Choopun, S.; Wlodarski, W.; Ippolito, S. J.; Kalantar-zadeh, K. *IEEE Sens. J.* **2007,** *7,* 919–924. doi:10.1109/JSEN.2007.895963
22. Oh, E.; Choi, H.-Y.; Jung, S.-H.; Cho, S.; Kim, J. C.; Lee, K.-H.; Kang, S.-W.; Kim, J.; Yun, J.-Y.; Jeong, S.-H. *Sens. Actuators, B* **2009,** *141,* 239–243. doi:10.1016/j.snb.2009.06.031
23. Dvorak, J.; Jirsak, T.; Rodriguez, J. A. *Surf. Sci.* **2001,** *479,* 155–168. doi:10.1016/S0039-6028(01)00973-6
24. Ballerini, G.; Ogle, K.; Barthés-Labrousse, M.-G. *Appl. Surf. Sci.* **2007,** *253,* 6860–6867. doi:10.1016/j.apsusc.2007.01.126
25. Ahn, M.-W.; Park, K.-S.; Heo, J.-H.; Park, J.-G.; Kim, D.-W.; Choi, K. J.; Lee, J.-H.; Hong, S.-H. *Appl. Phys. Lett.* **2008,** *93,* 263103. doi:10.1063/1.3046726

License and Terms

The definitive version of this article is the electronic one which can be found at:
doi:10.3762/bjnano.3.43

Beilstein Journal
of Nanotechnology

Reduced electron recombination of dye-sensitized solar cells based on TiO_2 spheres consisting of ultrathin nanosheets with [001] facet exposed

Hongxia Wang*, Meinan Liu, Cheng Yan and John Bell

Full Research Paper

Open Access

Address:
School of Chemistry, Physics and Mechanical Engineering,
Queensland University of Technology, 2 George Street, GPO Box
2434, Brisbane, QLD 4001, Australia

Email:
Hongxia Wang* - hx.wang@qut.edu.au

* Corresponding author

Keywords:
dye-sensitized solar cells; electrochemical impedance spectroscopy;
electron recombination; TiO_2 [001] facet; ultrathin nanosheets

Beilstein J. Nanotechnol. **2012,** *3,* 378–387.
doi:10.3762/bjnano.3.44

Received: 18 January 2012
Accepted: 23 April 2012
Published: 07 May 2012

This article is part of the Thematic Series "Nanostructures for sensors, electronics, energy and environment".

Guest Editor: N. Motta

Abstract

An anatase TiO_2 material with hierarchically structured spheres consisting of ultrathin nanosheets with 100% of the [001] facet exposed was employed to fabricate dye-sensitized solar cells (DSCs). Investigation of the electron transport and back reaction of the DSCs by electrochemical impedance spectroscopy showed that the spheres had a threefold lower electron recombination rate compared to the conventional TiO_2 nanoparticles. In contrast, the effective electron diffusion coefficient, D_n, was not sensitive to the variation of the TiO_2 morphology. The TiO_2 spheres showed the same D_n as that of the nanoparticles. The influence of $TiCl_4$ post-treatment on the conduction band of the TiO_2 spheres and on the kinetics of electron transport and back reactions was also investigated. It was found that the $TiCl_4$ post-treatment caused a downward shift of the TiO_2 conduction band edge by 30 meV. Meanwhile, a fourfold increase of the effective electron lifetime of the DSC was also observed after $TiCl_4$ treatment. The synergistic effect of the variation of the TiO_2 conduction band and the electron recombination determined the open-circuit voltage of the DSC.

Introduction

In the past two decades, dye-sensitized solar cells (DSCs) have received substantial attention from both academic and industrial communities as one of the most promising low-cost, high-efficiency third-generation photovoltaic devices [1,2]. A typical DSC consists of a dye-coated TiO_2 electrode, which is deposited on a fluorine-doped tin oxide (FTO) conductive-glass substrate, a I^-/I_3^- redox-couple-based electrolyte and a platinum counter electrode. Upon illumination, a photon with high energy (higher than the energy difference between the HOMO and LUMO level of the dye molecule) excites an electron from the ground state of the dye molecule to its excited state. The electron is then injected to the conduction band of the adjacent TiO_2 material, owing to a favorable alignment of the energetics. The electron goes through a series of trapping/detrapping process in the TiO_2 film before reaching the current collector, which is based on the conductive fluorine-doped tin oxide (FTO) substrate. Meanwhile, a parallel reaction, which involves transfer of the hole from the oxidized state of the dye (dye^+) to the surrounding I^- ions of the redox couple of the electrolyte, occurs to regenerate the dye molecule, resulting in the formation of I_3^- ions. The electrical circuit is completed through transfer of the electron, which arrives at the Pt counter electrode through the external circuit, to the I_3^- ions of the electrolyte.

Apparently, the operation of a DSC depends on several reactions that occur at the interface between different materials [3]. In particular, the process of electron injection at the TiO_2/dye interface and the electron recombination reaction at the TiO_2/dye/electrolyte interface are critical because they control both the short-circuit current and open-circuit voltage of the DSC. The surface properties of the TiO_2 material play an important role in both processes. The process of electron injection in DSCs is controlled by the energy difference between the conduction band of the TiO_2 material and the LUMO level of the dye, and the process of electron recombination is mainly dominated by the interaction between the electron at the surface of TiO_2 and I_3^- ions in the electrolyte. Generally, the TiO_2 used in DSCs is based on the anatase phase with the [101] facet exposed, due to the robust stability of this surface compared to other crystal facets [4]. It has been reported that the average surface energies of the different facets of anatase TiO_2 lie in the order of [001] (0.90 J/m^2) > [100] (0.53 J/m^2) > [101] (0.44 J/m^2) [5]. Apparently, the lowest surface energy of the [101] facet is the most stable surface of the TiO_2 material. However, with the progress in synthesis techniques, other active facets of TiO_2 crystals, such as [001], which is normally unstable due to a higher surface energy, can now be made [6]. In practice, TiO_2 material with a large percentage of [001] high-energy surface has shown superior performance in applications such as water splitting and lithium-ion batteries [6-8]. Further investigation shows that the [001] surface is more beneficial to the photooxidization process through the O^- centers compared to the [101] surface, which contains more Ti^{3+} centers [9].

The different surface properties of the [001] and [101] facets of TiO_2 are expected to have a profound effect on the chemicophysical processes in DSCs as well. Fan et al. reported that the [001] surface can absorb more dye molecules compared to the [101] surface [10]. However, the influence of the TiO_2 [001] facet on the kinetics of electron transfer and back reaction has not been reported. A deep understanding of the role of the TiO_2 [001] facet in these key processes of electron transport and recombination of DSCs is of great importance for both practical applications and basic research.

In this work, anatase TiO_2 spheres with a hierarchical structure consisting of ultrathin nanosheets with 100% of the [001] facet exposed were synthesized and applied in dye-sensitized solar cells (DSCs). The photovoltaic performance of the DSCs with different concentrations of the hierarchically structured TiO_2 spheres was evaluated. The kinetics of electron transport and back reaction of the DSCs with the spheres were investigated by electrochemical impedance spectroscopy. In addition, the effect of treatment by an aqueous solution of $TiCl_4$ on the performance of the DSCs with the TiO_2 spheres was discussed.

Experimental

Synthesis of TiO_2 nanosheet particles

Hierarchically structured TiO_2 spheres of the nanosheets were synthesized by following the method originally reported by Chen et al. [6]. Briefly, a precursor solution containing titanium isopropoxide (Sigma-Aldrich; 1.15 mL) and diethylenetriamine (DETA; 0.02 mL) in 32 mL isopropanol was prepared by vigorous magnetic stirring of the mixture of the three components at room temperature. The precursor solution was then transferred to a Teflon-lined stainless steel autoclave (45 mL volume, Parr Instrument Co.) for the hydrothermal reaction. The hydrothermal process was carried out at 200 °C for 24 h in an electric oven. After that, the autoclave was allowed to cool to room temperature naturally. The as-collected white powder was washed with deionized water and then ethanol several times to remove the organic residues. The powder was then dried at 80 °C for 5 h and finally sintered at 400 °C for 3 h to improve the crystallinity.

Fabrication of TiO_2 paste

TiO_2 pastes for the DSCs were fabricated by mixing methylcellulose (M_w = 20,000), α-terpinol and the as-prepared TiO_2 powder in a controlled amount, by using magnetic stirring at 80 °C for 48 h. Two sets of paste with different concentrations of the TiO_2 powder were prepared. Paste A contained 13 wt % TiO_2 powder, 2.6 wt % methylcellulose and 84.4 wt % α-terpinol. Paste B contained 25 wt % TiO_2 powder, 2.5 wt % methylcellulose and 72.5 wt % α-terpinol. A commercial TiO_2 paste (DSL-18-NR, Dyesol) consisting of anatase TiO_2 nanoparticles with an average size of 20 nm was employed for comparison.

Assembly of dye-sensitized solar cells

The procedure for the fabrication of the dye-sensitized solar cells was reported in our previous work [11,12]. Briefly, a substrate based on fluorine-doped tin oxide (FTO) conductive glass (TEC15, Pilkington) was thoroughly washed with detergent water, distilled water, acetone, isopropanol and ethanol in sequence under sonication for 15 min. The cleaned FTO substrate was first coated with a compact layer of TiO_2 film by spray pyrolysis to reduce the electron back reaction at the interface between the bare FTO and the electrolyte. The substrate was then deposited with the as-prepared TiO_2 paste or the commercial paste by a doctor-blading method using adhesive tape as a spacer to control the thickness of the film. The TiO_2 film was dried on a hotplate at 90 °C for 10 min before being sintered at 450 °C for 30 min to form a mesoporous structure. The average thickness of the TiO_2 film was 13 µm. $TiCl_4$ post-treatment of the TiO_2 film was carried out by immersing the sintered film in $TiCl_4$ aqueous solution (40 mM) at 70 °C for 30 min. The film was washed with distilled water thoroughly and blow dried with N_2 gas. The film was then resintered at 450 °C for 30 min. The geometrical area of the TiO_2 film was 0.25 cm^2.

The TiO_2 film (with or without $TiCl_4$ treatment) when it was still warm (around 80 °C) was immersed in a dye solution containing 0.25 mM *cis*-bis(isothiocyanato) bis(2,2′- bipyridyl-4,4′-dicarboxylate) ruthenium(II) bis-tetrabutylammonium (N719, Dyesol) in ethanol for 16 h to form a dye-coated photoanode. A platinum counter electrode was prepared by dropping 5 µL isopropanol solution containing $H_2PtCl_6{\cdot}6H_2O$ (5 mM) onto a cleaned FTO substrate (1.5 × 1.0 cm^2). After being allowed to dry in air, the substrate was then sintered at 390 °C for 15 min in an electric oven to form a thin Pt layer on the FTO substrate. A dye-sensitized solar cell was assembled by sealing the dye-coated TiO_2 electrode with the platinum-coated FTO counter electrode by using a thermal plastic (Surlyn 1705) at 130 °C. The electrolyte composed of 0.6 M 1-propyl-3-methylimidiazolium iodide, 0.05 M I_2, 0.1 M guanidinium thiocyanate, 0.2 M NaI, 0.1 M *N*-methyl benzimidazole in 3-methoxypropionitrile was introduced into the space between the electrodes through the holes that were predrilled in the Pt counter electrode by a vacuum-assisted technique. The holes were then sealed by using a Surlyn film covered with a microscope slip.

Characterization

The morphology and the crystal structure of the as-prepared TiO_2 powder were investigated by scanning electron microscope (SEM, FEI Quanta 200) and powder X-ray diffraction (XRD, PANanalytical Xpert Pro), respectively. Transmission electron microscopy (TEM, Philips CM 200) was used to monitor the detailed structure of the TiO_2 powder. The thickness of the TiO_2 films for the DSCs was determined by a profilometer (Dektak 150). The photocurrent density–voltage (*J–V*) characteristics of the DSCs were obtained by using a Xe lamp (150 W) based solar simulator (Newport), by recording the current produced by the cells as a function of the applied bias under AM1.5 illumination (100 mW/cm^2) with a computer-controlled digital source meter (Keithley 2420). The illumination intensity of the incident light from the solar simulator was measured with a silicon photodiode, which was calibrated with an optical meter (1918-C, Oriel). Aluminum foil with a size comparable to the active area of the TiO_2 film was used as a reflector on the counter electrode side of the DSCs during the *J–V* measurement.

The electrochemical impedance spectroscopy (EIS) of the DSCs was measured in the frequency range of 50,000–0.1 Hz at room temperature by a Versa-stat 3 electrochemical workstation (Princeton Applied Research). The EIS measurement was carried out under illumination, which was provided by a light emitting diode (LED, 627 nm) at open-circuit. The intensity of the incident illumination on the front side of the DSC (TiO_2 side) was adjusted by using a combination of neutral density filters. The EIS spectrum was analyzed with a Zview software, by using a transmission-line-based equivalent circuit to obtain the information of chemical capacitance, electron-recombination resistance and electron-transport resistance of the DSCs [12,13].

Results and Discussion

Figure 1a shows the image of the as-prepared TiO_2 powder by SEM. The material consists of microsized particles with spherical shape. The surface of the sphere is very rough and appears fluffy. The diameter of the sphere is around 1.6 µm as determined by TEM (Figure 1b). TEM images (Figure 1b, Figure 1c) also illustrate that the sphere has a substructure, which consists of ultrathin nanosheets packed together. It is speculated that the sphere is formed through self-assembly of the nanosheets to realize a minimum surface energy. Some spheres have pits on the surface, which may be due to the insufficient reaction duration. The measurement of the N_2 adsorption/desorption isotherms of the TiO_2 powder shows that the specific surface area of the TiO_2 spheres is 82 m^2/g, which is slightly higher than the specific surface area of the film made from the commercial TiO_2 paste (DSL-18NR, Dyesol. Surface area: 72.9 m^2/g) [14]. The large surface area of the material suggests that the nanosheets are probably loosely packed such that a greater surface area is exposed. The XRD pattern of the material (Figure 1d) shows that the as-prepared TiO_2 powder is anatase with a tetragonal structure and space group $I4_1/amd$ (JCPDS card, No. 71-1169). Both the TEM images and the XRD results are in good agreement with the results reported by Chen et al. According to Chen et al., the TiO_2 spheres synthesized by this method have 100% of the [001] surface exposed [6].

The SEM image of the TiO_2 film consisting of the spheres is shown in Figure 1e and Figure 1f. Apparently, the TiO_2 particles are connected to each other in the film. Figure 1f shows that the film contains a large number of small pores. However, the sphere of the TiO_2 particles is rarely seen in the film. This indicates that the mechanical force of grinding and sonication employed in the preparation of the film broke up the spheres into small particles, probably in the form of nanosheets. Never-

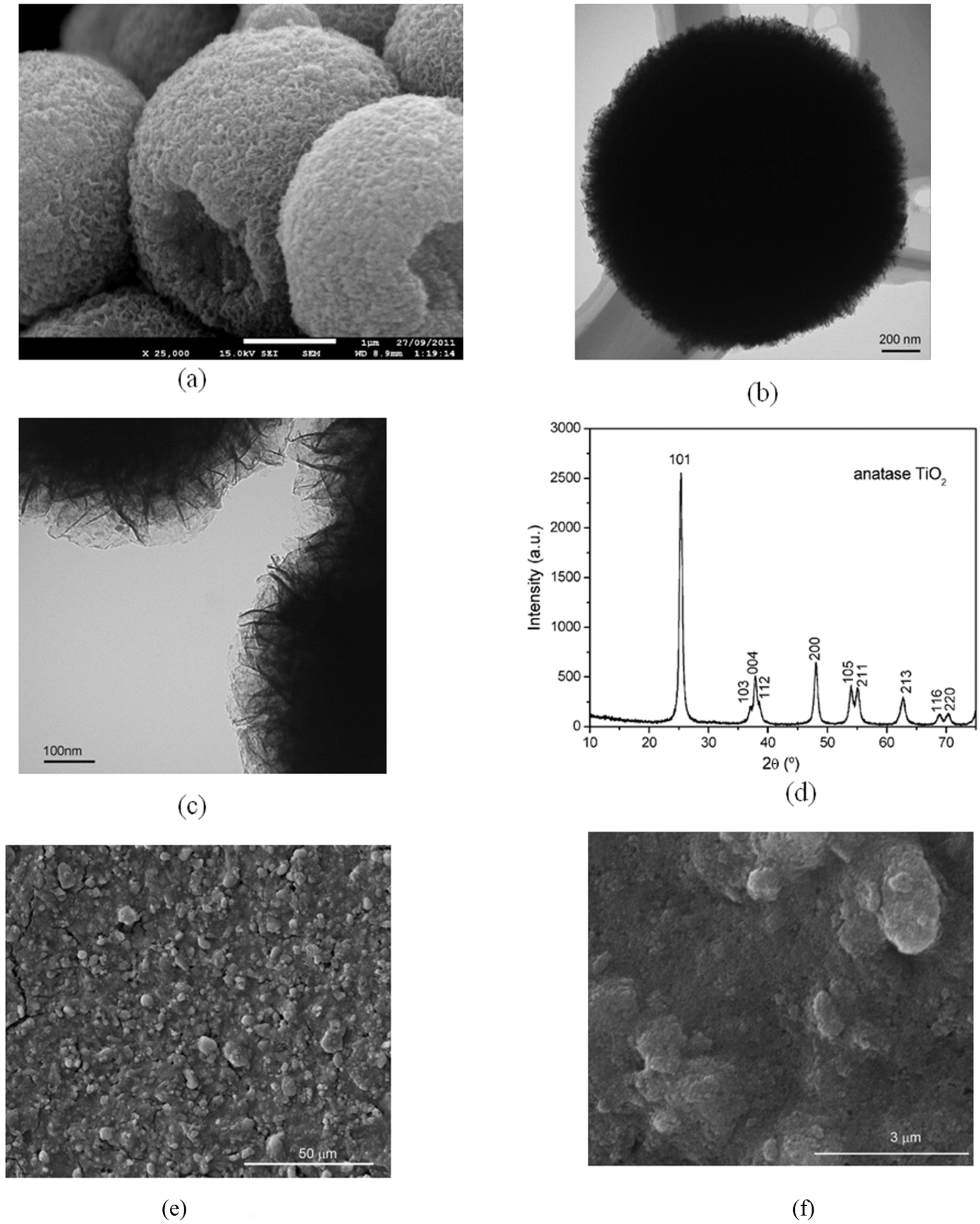

Figure 1: Images of TiO_2 particles by SEM (a) and by TEM (b, c) as well as XRD pattern of the TiO_2 particles (d) and morphology of the TiO_2 film consisting of the as-prepared sphere particles (e, f).

theless, the same XRD pattern of the sintered TiO_2 film (not shown) indicates that the film has the same surface properties as the spheres.

J–V characteristics of the DSCs

The *J–V* characteristics of the DSCs with the TiO_2 film made from paste A, which contained 13 wt % TiO_2 spheres with and without $TiCl_4$ post-treatment, is shown in Figure 2a. The DSC solely based on paste A without $TiCl_4$ treatment (curve A) produced a short-circuit current density (J_{sc}) of 8.79 mA/cm^2 and open-circuit voltage (V_{oc}) of 0.76 V. In contrast, when the TiO_2 film was subjected to $TiCl_4$-solution treatment, the J_{sc} of the DSC (curve B) increased to 12.1 mA/cm^2, which is 37.5% higher than that of curve A.

Figure 2b shows the *J–V* performance of the DSCs made from paste B, which contained 25 wt % as-prepared TiO_2 nanosheet-based particles. The J_{sc} of the cell was 15.6 mA/cm^2 and V_{oc} = 0.70 V (Figure 2b, curve C) when there was no $TiCl_4$ treatment. Compared to curve A, it was found that the ratio of the J_{sc} of curve C to that of curve A ((15.6 mA/cm^2)/(12.1 mA/cm^2) = 1.77) is very close to the ratio of the concentration of the TiO_2 spheres in the two pastes ((TiO_2 wt % in paste B)/(TiO_2 wt % in paste A) = 25/13 = 1.92). This suggests that the higher J_{sc} of the DSC made from paste B is due to the availability of more TiO_2 particles in the film, which can absorb more dye molecules, leading to a stronger light absorption. The J_{sc} of the DSC made from paste B was further increased from 15.6 mA/cm^2 (Figure 2b, curve C) to 18.2 mA/cm^2 when the TiO_2 film was processed with $TiCl_4$ solution (Figure 2b, curve D). Meanwhile, the V_{oc} of curve D was 20 mV higher than that of curve C, suggesting a beneficial effect of the $TiCl_4$ post-treatment on V_{oc} as well. The best performance was obtained in the case of curve D with power conversion efficiency = 7.57% (Figure 2b), which is comparable to the efficiency (η = 7.52%) of the DSCs made from the commercial paste (*I–V* curve is not shown). The detailed characteristic parameters of the performance of the DSCs with different TiO_2 pastes are shown in Table 1.

Electrochemical impedance spectroscopy

Information on the charge-transfer and charge-transport process in DSCs can be measured by small-perturbation-based transient

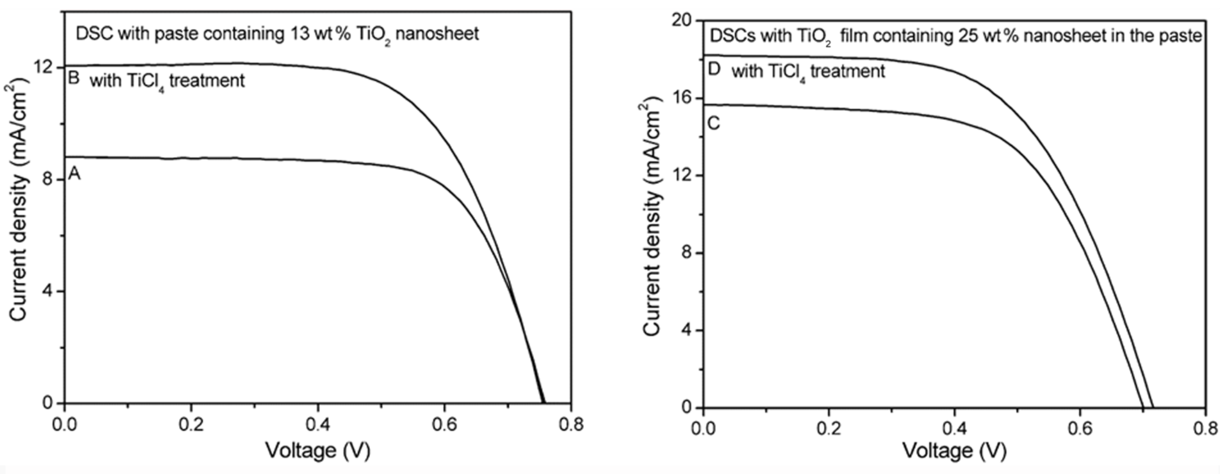

(a) (b)

Figure 2: *J–V* characteristics of the dye-sensitized solar cells made from paste A containing 13 wt % TiO_2 spheres (a) and from paste B containing 25 wt % spheres (b) with (curve B and D) and without (curve A and C) $TiCl_4$ treatment.

Table 1: Characteristic performance parameters of the dye-sensitized solar cells.

cell name	J_{sc} (mA/cm^2)	V_{oc} (V)	*FF*	efficiency (%)
13 wt % TiO_2 nanosheet (curve A)	8.79	0.757	0.700	4.66
13 wt % TiO_2 nanosheet with $TiCl_4$ treatment (curve B)	12.07	0.754	0.646	5.88
25 wt % TiO_2 nanosheet (curve C)	15.60	0.700	0.610	6.66
25 wt % TiO_2 nanosheet with $TiCl_4$ treatment (curve D)	18.20	0.720	0.580	7.57
DSC made from TiO_2 nanoparticles	16.50	0.755	0.604	7.52

methods, such as electrochemical impedance spectroscopy (EIS) or intensity modulated photocurrent spectroscopy (IMPS) and intensity modulated photovoltage spectroscopy (IMVS) [13,15]. Compared to IMPS and IMVS, the advantage of the EIS method for characterization of DSCs lies in the fact that both the effective electron lifetime, τ_n, and the effective electron diffusion coefficient, D_n, can be obtained in one measurement. This is achieved by fitting the EIS spectrum using a suitable equivalent circuit that mimics the physical process in the device. The equivalent circuit that depicts the process of electron trapping/detrapping in DSCs is shown in Figure 3a. It contains a series resistance, R_s, a capacitance at the Pt electrode/electrolyte interface, C_{Pt}, and a resistance for the charge-transfer process between electrons at the Pt electrode and I_3^- ions of the electrolyte, R_{Pt}. Z_w is the Warburg resistance arising from the ion transport in the electrolyte and Z_{tl} is a distribution line describing the electron transport and recombination in the mesoporous TiO_2 film [13,16]. A typical EIS spectrum of a DSC is shown in Figure 3b for the Nyquist plot and Figure 3c for the Bode plot. The corresponding fitting results (green line) using the equivalent circuit are also shown in Figure 3b and Figure 3c. The distorted semicircle in the high frequency range (above 10 Hz) is ascribed to the electron transfer process at the interface of Pt counter electrode/electrolyte combined with the electron-transport process in the TiO_2 film (the semicircle corresponding to the electron transport process in TiO_2 is buried in the semicircle of the charge-transfer process at the Pt/electrolyte interface in the spectrum) [3]. The large semicircle in the lower frequency range (10–0.1 Hz) is due to the electron recombination process in the TiO_2 film. Under a high incident illumination intensity, the density of the photogenerated electron in the TiO_2 film is very high (up to $10^{18}/cm^3$) and the TiO_2 film becomes conductive [17]. In this case, the resistance corresponding to the electron-transport process becomes too small to be observed in the EIS spectrum. Consequently, the EIS spectrum is mainly dominated by the electron recombination process. Nevertheless, under low incident illumination intensity, the conductivity of the TiO_2 film is very low due to a low density of photogenerated electrons. In this case, the main feature of the EIS spectrum is due to the transport of electrons in the TiO_2 film. Hence, an accurate fitting of the EIS spectrum of a DSC using the equivalent circuit is normally obtained in the illumination range in which both the electron-transport resistance and the electron-recombination resistance are substantial [13]. Only the results of good fits are shown in this work.

Comparison of electron transport and recombination of the DSC based on TiO_2 spheres and nanoparticles

The electron-recombination process in DSCs is reflected by the effective electron lifetime, τ_n, whereas the electron-transport

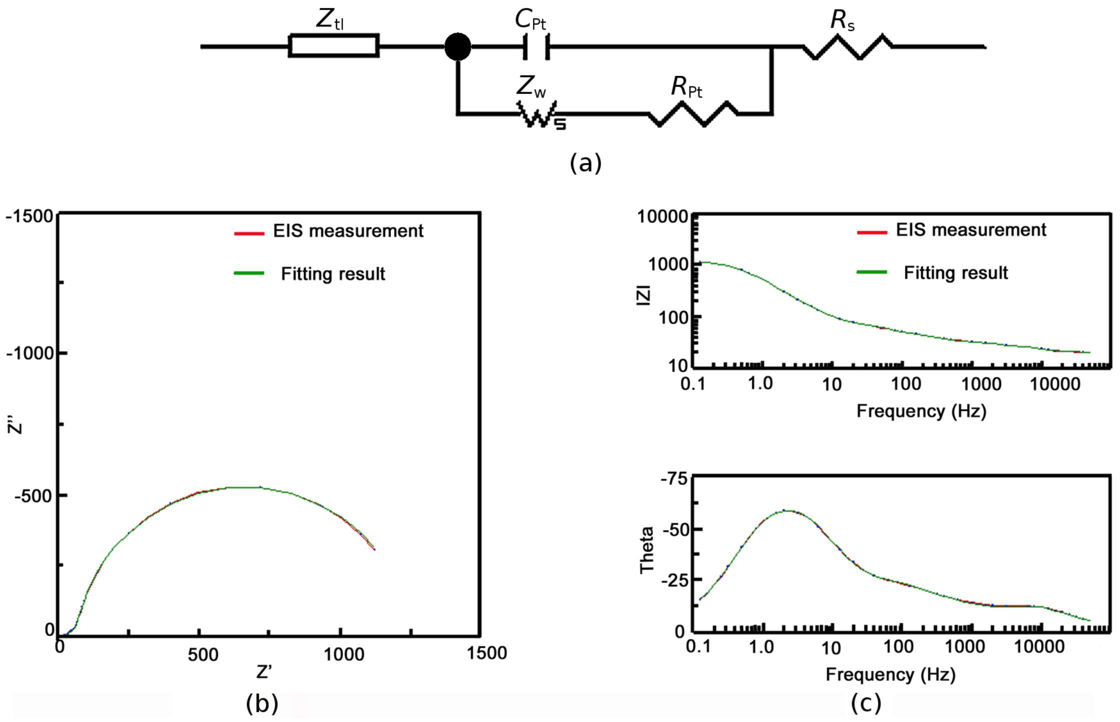

Figure 3: Equivalent circuit (a) and the Nyquist plot (b) and Bode plot (c) of the impedance spectrum of a dye-sensitized solar cell.

process is manifested by the effective electron diffusion coefficient D_n. Bisquert et al. showed that both τ_n and D_n of a DSC are dependent on the distribution of the density of electrons in the conduction band (free electron) and in the trap states (trapped electron) of the TiO_2 film as well as the lifetime and diffusion coefficient of free electron (τ_0 and D_0), through the following consideration:

$$\tau_n = \left(1 + \frac{\partial n_t}{\partial n_c}\right)\tau_0 \tag{1}$$

and

$$D_n = \left(1 + \frac{\partial n_t}{\partial n_c}\right)^{-1} D_0 \tag{2}$$

where n_t and n_c are the densities of the trapped electron and free electron, respectively [18].

The charge distribution, $g(E)$, in a mesoporous TiO_2 film is described by [18,19]:

$$\begin{aligned} g({}_nE_F) &= \frac{N_{t,0}}{k_B T_0}\exp(-\frac{E_c - {}_nE_F}{k_B T_0}) \\ &= \frac{N_{t,0}}{k_B T_0}\exp(-\frac{E_c - E_{F,\mathrm{redox}} - qV}{k_B T_0}), \end{aligned} \tag{3}$$

where ${}_nE_F$ is the quasi Fermi level of TiO_2, E_c the conduction band of TiO_2, $E_{F,\mathrm{redox}}$ the potential energy of the redox couple, $N_{t,0}$ the total density of the trapped electrons, k_B is the Boltzmann constant and T_0 the characteristic temperature that reflects the profile of the charge distribution in TiO_2.

Therefore, comparison of the change of τ_n and D_n in DSCs due to the different material composition should be made by using the density of charge as the reference, provided that the distribution profile of charge density is the same [20].

The density of charge in the TiO_2 film is reflected by the chemical capacitance, C_μ, which is measured by EIS, through the relationship [18]:

$$C_\mu({}_nE_F) = \int_{E_v}^{E_c} C_\mu({}_nE_F, E)\mathrm{d}E \approx q^2 g({}_nE_F). \tag{4}$$

where E_v is the valence band of TiO_2. Thus, we employ the density of chemical capacitance as a reference for the investigation of the variation of τ_n and D_n in the following.

Figure 4a shows the τ_n of the DSCs with the TiO_2 films consisting of the nanosheet-based spheres and the conventional nanoparticles as a function of the chemical capacitance density. It is found the τ_n of the nanosheets based DSC is nearly threefold higher than that of the nanoparticles for a constant capacitance density. This suggests that the TiO_2 film with the spheres has a lower electron-recombination reaction rate compared to the film with the nanoparticles. Besides $\tau_{n,}$ the effective electron diffusion coefficient, D_n, is another important parameter that determines the performance of a DSC. The comparison of the D_n of the cell based on the spheres and the nanoparticles is shown in Figure 4b. It is interesting that both materials show the same D_n, suggesting that the electron transport is not affected by the morphology and the exposed crystal facet of the TiO_2 material. The identical D_n also suggests that the diffusion coefficient of the free electron is the same for the two materials, according to Equation 2 [13]. It also justifies the assumption that the profile of the distribution of charge density is the same in the two types of TiO_2 film. In contrast, the different τ_n suggests that the free-electron lifetime of the spheres is different to that of the nanoparticles. The high τ_n of the spheres could be related to the properties of the [001] facet, but clarification of this issue requires further investigation. As a consequence, the electron diffusion length, L_n, which depends on both the τ_n and D_n by $L_n = \sqrt{\tau_n D_n}$, is up to 1.6-fold higher for the nanosheet-based TiO_2 spheres compared to that of the nanoparticles (Figure 4c). It is found that the L_n of the DSC based on the nanoparticles is only around 16 µm (Figure 4c), which is comparable to the thickness of the TiO_2 film (13 µm). A previous study has shown that the L_n of a DSC needs to be at least three times the thickness of the TiO_2 film in order to collect most of the photogenerated electrons [13]. Therefore, the short L_n may limit the performance of the DSC. The higher L_n of the spheres-based DSC should lead to a higher electron collection efficiency compared to its nanoparticles counterpart.

Besides J_{sc}, V_{oc} is another key performance parameter of a DSC. The maximum voltage of a DSC is determined by the potential difference between the conduction band of TiO_2 and the redox potential of I^-/I_3^- in the electrolyte. Obviously, the position of the TiO_2 conduction band edge, E_c, has a direct impact on the open-circuit voltage (V_{oc}) of the DSC. Thus, it is important to know the relative position of the E_c of the nanosheet-based spheres relative to the nanoparticles in order to determine the reason for the different V_{oc}. According to Equation 3, the change of E_c of TiO_2 can be monitored by the variation of the voltage (V) of the DSC at a constant electron density.

As shown in Figure 4d, the E_c of the nanosheet-based spheres is found to be 100 meV lower than that of the nanoparticles. The lower E_c of the spheres is probably due to the different dye

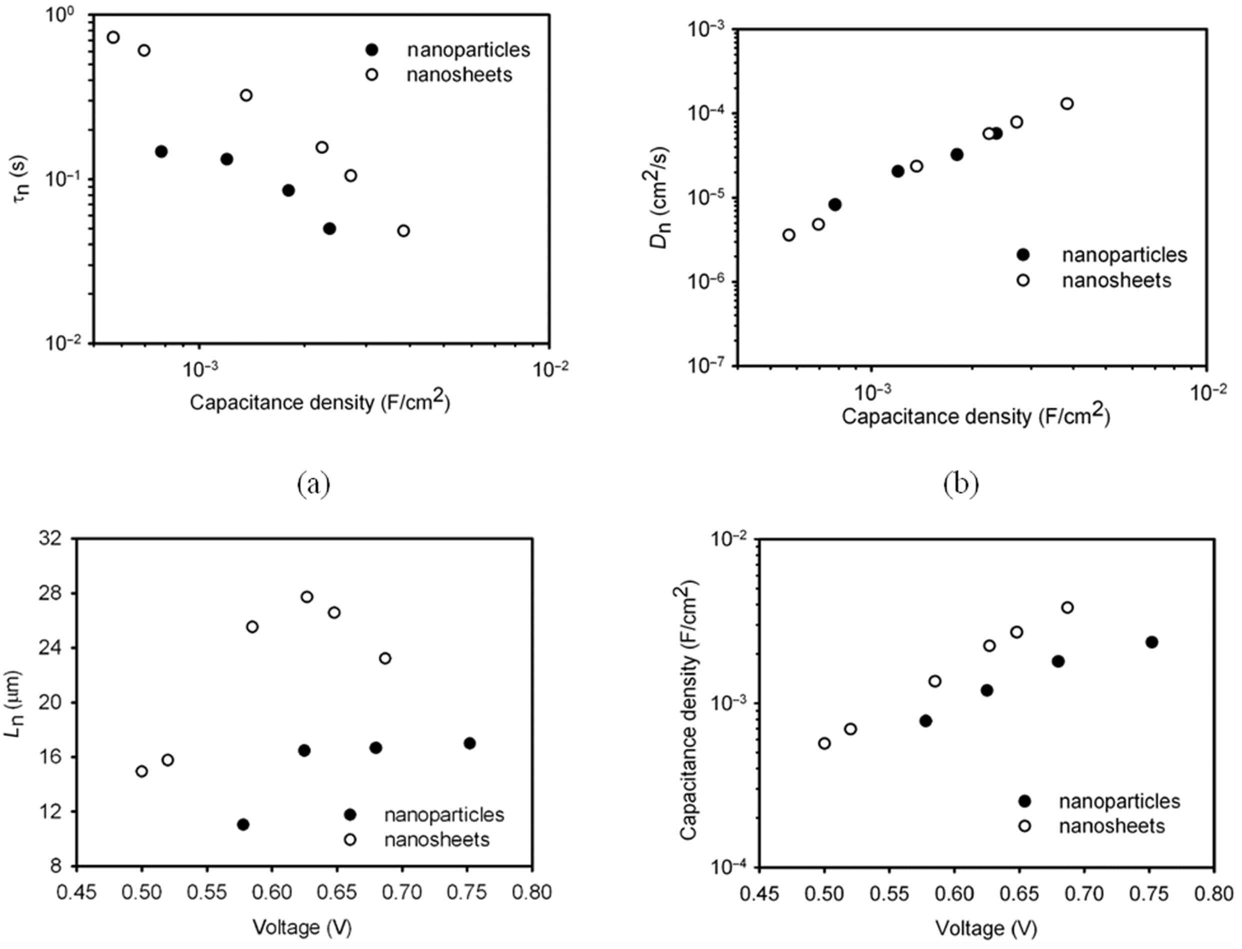

(a) (b)

(c) (d)

Figure 4: Comparison of the effective electron lifetime, τ_n, (a) and effective electron diffusion coefficient, D_n, (b) and electron diffusion length, L_n, (c) of the DSCs with TiO_2 nanosheets (open circle) and with conventional nanoparticles (solid circle). (d) Variation of the chemical capacitance density of the nanosheets and nanoparticles as a function of voltage.

loading on the TiO_2 films. According to Fan et al. [10], the TiO_2 [001] facet can absorb more dye than the [101] facet. Nazeeruddin et al. confirmed that the dye molecule is adsorbed on TiO_2 particles mainly through the carboxylic acid group (–COOH) [4], leading to the protonation of the surface of TiO_2 and the downward shift of the E_c. The more dye molecules are adsorbed on the TiO_2 film, the more downward shift is expected for the E_c.

Effect of $TiCl_4$ treatment

The strategy of treating TiO_2 mesoporous films with $TiCl_4$ aqueous solution has been extensively employed to improve the performance of DSCs. In most cases, it is found that the J_{sc} of the DSC is enhanced, while the V_{oc} is reduced after the $TiCl_4$ treatment of the film. O'Regan et al. found that $TiCl_4$ treatment caused 80 meV downward shift of the TiO_2 conduction band, resulting in an increased driving force for the electron-injection process. They reported that the enhanced J_{sc} was owing to an improved electron-injection efficiency of the DSC [21,22]. In the following section, the influence of the $TiCl_4$ solution treatment on the E_c of the TiO_2-spheres-based film and on the kinetics of electron transport and back reaction of the corresponding DSCs is investigated.

Figure 5a illustrates the chemical capacitance density of the DSCs made from paste B with and without $TiCl_4$ treatment, as a function of the voltage. It is found that, at a constant charge density, the voltage of the cell with $TiCl_4$ treatment is lower than that of the DSC without the treatment. The maximum difference in voltage between the cells is around 30 mV. Provided that the distribution profile of the charge density is the same for the TiO_2 film with and without $TiCl_4$ treatment, the reduced potential of the DSC with $TiCl_4$ treatment means that the $TiCl_4$ treatment caused a downward shift of the TiO_2

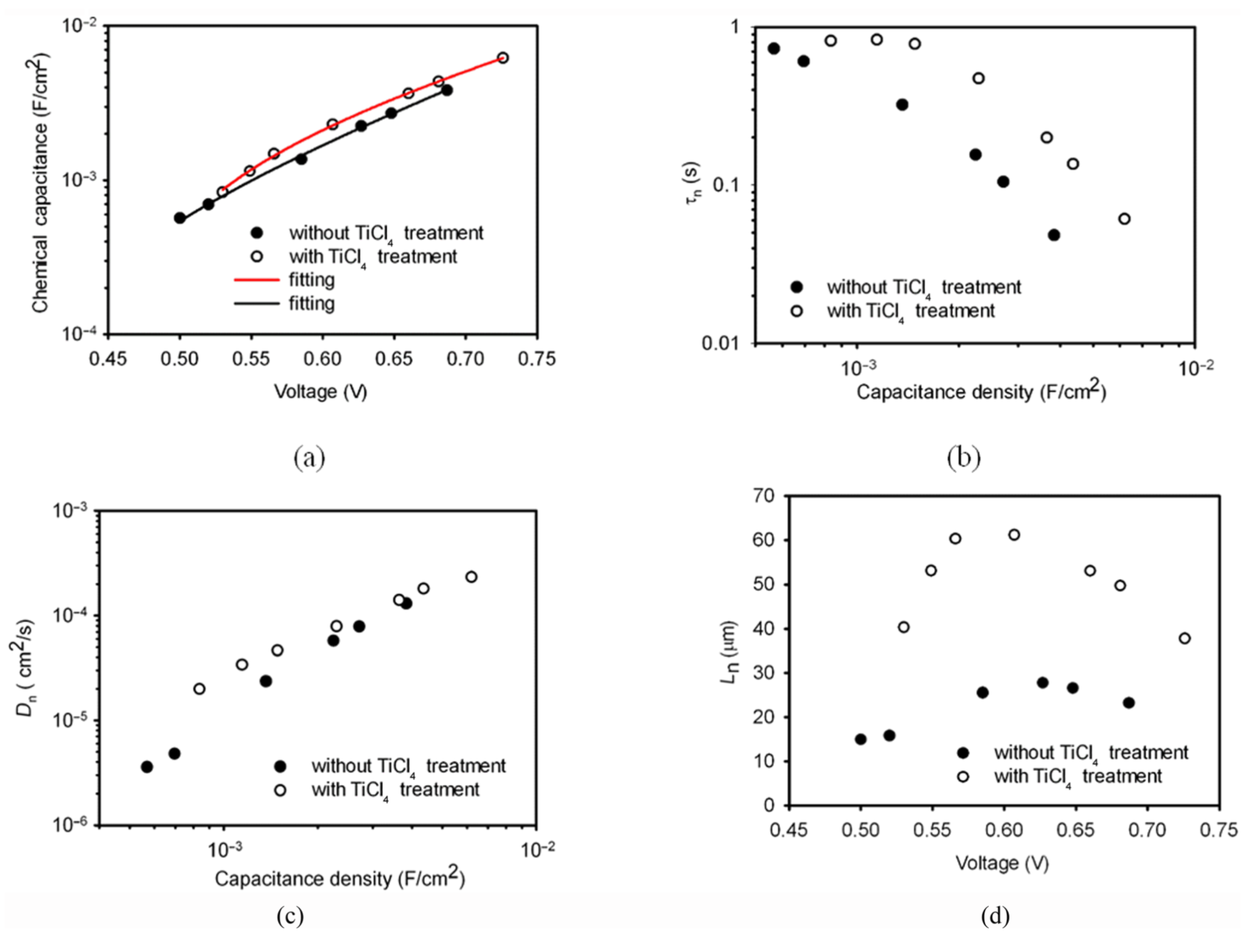

(a)

(b)

(c)

(d)

Figure 5: Comparison of dye-sensitized solar cells based on hierarchically structured TiO_2 spheres with and without $TiCl_4$ post-treatment. (a) Chemical capacitance vs voltage; (b) effective electron lifetime, τ_n, as a function of density of chemical capacitance; (c) effective electron diffusion coefficient, D_n, as a function of density of chemical capacitance; and (d) electron diffusion length, L_n as a function of voltage.

conduction band by 30 meV, which may decrease the maximum voltage the DSC can achieve. This observation is in good agreement with the results reported by O'Regan et al. [21]. However, the V_{oc} of the cell with $TiCl_4$ treatment is actually 20 mV higher than the DSC without the treatment, as shown in Figure 2b. This indicates that the electron recombination of the DSC is probably affected by the $TiCl_4$ treatment.

Figure 5b shows the τ_n as a function of capacitance density of the DSC with and without $TiCl_4$ treatment. It is found that τ_n is enhanced by a factor of 3.8 after $TiCl_4$ treatment. In contrast, D_n of the DSCs is relatively unchanged with the $TiCl_4$ treatment (Figure 5c). Owing to the enhanced τ_n, the electron diffusion length, L_n, of the DSC is enhanced by a factor of two through $TiCl_4$ treatment (Figure 5d). Hence, the improved voltage (20 mV) of the DSC (Figure 2b, curve D) with $TiCl_4$ treatment compared to the cell without $TiCl_4$ treatment (curve C in Figure 2b) should be a result of a synergistic effect of the decreased TiO_2 conduction band and the increased electron lifetime. Apparently, the beneficial effect of the enhanced electron lifetime on V_{oc} surpasses the negative effect of the downward shift of the E_c of TiO_2, leading to a higher V_{oc}.

Conclusion

Dye-sensitized solar cells with a TiO_2 electrode made from hierarchically structured TiO_2 spheres, consisting of nanosheets with 100% of the [001] facet exposed, were assembled and characterized in terms of the device performance, the kinetics of electron transport and back reaction. It was found that the TiO_2-spheres-based DSCs generated an energy conversion efficiency of 7.57%, which is comparable to the conventional TiO_2 nanoparticles. Investigation of the kinetics of electron transport and back reaction of the DSCs showed that the spheres had a threefold higher effective electron lifetime compared to the nanoparticles. However, the effective electron diffusion coefficient, D_n, of the DSCs was not affected by the different morphology and exposed crystal facets of the TiO_2 material. Monitoring of the variation of the conduction band of the dyed

TiO_2 film disclosed that the E_c of the spheres-based TiO_2 electrode was 100 meV lower than that of the nanoparticles.

This work also investigated the influence of treatment with $TiCl_4$ aqueous solution on the E_c of the TiO_2 spheres and on the τ_n and D_n of the corresponding DSCs. It was found that $TiCl_4$ treatment caused a downward shift (30 meV) of the TiO_2 conduction band and a fourfold increase of the τ_n, whereas the D_n of the cell was not significantly affected by the $TiCl_4$ treatment.

Acknowledgements

The authors (H. Wang and M. Liu) acknowledge the financial support by Queensland University of Technology via the Vice-Chancellor Research Fellowship scheme.

References

1. O'Regan, B.; Grätzel, M. *Nature* **1991,** *353,* 737–740. doi:10.1038/353737a0
2. Wang, H.; Li, H.; Xue, B.; Wang, Z.; Meng, Q.; Chen, L. *J. Am. Chem. Soc.* **2005,** *127,* 6394–6401. doi:10.1021/ja043268p
3. Wang, H.; Bell, J.; Desilvestro, J.; Bertoz, M.; Evans, G. *J. Phys. Chem. C* **2007,** *111,* 15125–15131. doi:10.1021/jp075305f
4. Nazeeruddin, M. K.; Humphry-Baker, R.; Liska, P.; Grätzel, M. *J. Phys. Chem. B* **2003,** *107,* 8981–8987. doi:10.1021/jp022656f
5. Liu, M.; Chang, J.; Yan, C.; Bell, J. *Int. J. Smart Nano Mater.* **2012,** *3,* 72–80. doi:10.1080/19475411.2011.638345
6. Chen, J. S.; Tan, Y. L.; Li, C. M.; Cheah, Y. L.; Luan, D.; Madhavi, S.; Boey, F. Y. C.; Archer, L. A.; Lou, X. W. *J. Am. Chem. Soc.* **2010,** *132,* 6124–6130. doi:10.1021/ja100102y
7. Yang, H. G.; Sun, C. H.; Qiao, S. Z.; Zou, J.; Liu, G.; Smith, S. C.; Cheng, H. M.; Lu, G. Q. *Nature* **2008,** *453,* 638–641. doi:10.1038/nature06964
8. Zhu, J.; Wang, S.; Bian, Z.; Xie, S.; Cai, C.; Wang, J.; Yang, H.; Li, H. *CrystEngComm* **2010,** *12,* 2219–2224. doi:10.1039/c000128g
9. D'Arienzo, M.; Carbajo, J.; Bahamonde, A.; Crippa, M.; Polizzi, S.; Scotti, R.; Wahba, L.; Morazzoni, F. *J. Am. Chem. Soc.* **2011,** *133,* 17652–17661. doi:10.1021/ja204838s
10. Fan, J.; Cai, W.; Yu, J. *Chem.–Asian J.* **2011,** *6,* 2481–2490. doi:10.1002/asia.201100188
11. Wang, H.; Liu, M.; Zhang, M.; Wang, P.; Miura, H.; Cheng, Y.; Bell, J. *Phys. Chem. Chem. Phys.* **2011,** *13,* 17359–17366. doi:10.1039/C1CP22482D
12. Villanueva-Cab, J.; Wang, H.; Oskam, G.; Peter, L. M. *J. Phys. Chem. Lett.* **2010,** *1,* 748–751. doi:10.1021/jz1000243
13. Wang, H.; Peter, L. M. *J. Phys. Chem. C* **2009,** *113,* 18125–18133. doi:10.1021/jp906629t
14. Samadpour, M.; Giménez, S.; Zad, A. I.; Taghavinia, N.; Mora-Seró, I. *Phys. Chem. Chem. Phys.* **2012,** *14,* 522–528. doi:10.1039/c1cp22619c
15. Bisquert, J. *J. Phys. Chem. B* **2002,** *106,* 325–333. doi:10.1021/jp011941g
16. Wang, H.; Nicholson, P. G.; Peter, L.; Zakeeruddin, S. M.; Grätzel, M. *J. Phys. Chem. C* **2010,** *114,* 14300–14306. doi:10.1021/jp105753k
17. Nguyen, T. T. O.; Peter, L. M.; Wang, H. *J. Phys. Chem. C* **2009,** *113,* 8532–8536. doi:10.1021/jp901213f
18. Bisquert, J.; Vikhrenko, V. S. *J. Phys. Chem. B* **2004,** *108,* 2313–2322. doi:10.1021/jp035395y
19. Peter, L. M. *J. Phys. Chem. C* **2007,** *111,* 6601–6612. doi:10.1021/jp069058b
20. Wang, H.; Peter, L. M. *J. Phys. Chem. C* **2012,** in press. doi:10.1021/jp211807w
21. O'Regan, B. C.; Durrant, J. R.; Sommeling, P. M.; Bakker, N. J. *J. Phys. Chem. C* **2007,** *111,* 14001–14010. doi:10.1021/jp073056p
22. Sommeling, P. M.; O'Regan, B. C.; Haswell, R. R.; Smit, H. J. P.; Bakker, N. J.; Smits, J. J. T.; Kroon, J. M.; van Roosmalen, J. A. M. *J. Phys. Chem. B* **2006,** *110,* 19191–19197. doi:10.1021/jp061346k

License and Terms

The definitive version of this article is the electronic one which can be found at:
doi:10.3762/bjnano.3.44

Beilstein Journal
of Nanotechnology

Glassy carbon electrodes modified with multiwalled carbon nanotubes for the determination of ascorbic acid by square-wave voltammetry

Sushil Kumar[1] and Victoria Vicente-Beckett*[2]

Full Research Paper

Open Access

Address:
[1]Central Queensland University, Centre for Plant and Water Science, Rockhampton, Queensland 4702, Australia and [2]Central Queensland University, Centre for Environmental Management, Rockhampton, Queensland 4702, Australia

Email:
Victoria Vicente-Beckett* - v.vicente-beckett@cqu.edu.au

* Corresponding author

Keywords:
ascorbic acid; carbon nanotubes; glassy carbon electrode; square-wave voltammetry

Beilstein J. Nanotechnol. **2012,** *3,* 388–396.
doi:10.3762/bjnano.3.45

Received: 19 December 2011
Accepted: 26 April 2012
Published: 10 May 2012

This article is part of the Thematic Series "Nanostructures for sensors, electronics, energy and environment".

Guest Editor: N. Motta

Abstract

Multiwalled carbon nanotubes were used to modify the surface of a glassy carbon electrode to enhance its electroactivity. Nafion served to immobilise the carbon nanotubes on the electrode surface. The modified electrode was used to develop an analytical method for the analysis of ascorbic acid (AA) by square-wave voltammetry (SWV). The oxidation of ascorbic acid at the modified glassy carbon electrode showed a peak potential at 315 mV, about 80 mV lower than that observed at the bare (unmodified) electrode. The peak current was about threefold higher than the response at the bare electrode. Replicate measurements of peak currents showed good precision (3% rsd). Peak currents increased with increasing ascorbic acid concentration (dynamic range = 0.0047–5.0 mmol/L) and displayed good linearity ($R^2 = 0.994$). The limit of detection was 1.4 µmol/L AA, while the limit of quantitation was 4.7 µmol/L AA. The modified electrode was applied to the determination of the amount of ascorbic acid in four brands of commercial orange-juice products. The measured content agreed well (96–104%) with the product label claim for all brands tested. Recovery tests on spiked samples of orange juice showed good recovery (99–104%). The reliability of the SWV method was validated by conducting parallel experiments based on high-performance liquid chromatography (HPLC) with absorbance detection. The observed mean AA contents of the commercial orange juice samples obtained by the two methods were compared statistically and were found to have no significant difference ($P = 0.05$).

Introduction

L-ascorbic acid (AA), also known as vitamin C, is a well-known antioxidant, which helps the human body to reduce oxidative damage and protects food quality by preventing oxidative deterioration [1-3]. The overall oxidation of AA is [2]

$$C_6H_8O_6\,(\text{AA}) \rightarrow C_6H_6O_6\,(\text{dehydro-AA}) + 2H^+ + 2e^- \quad (1)$$

The growing use of AA in the food, pharmaceutical and cosmetic industries and its significance in biomedical science require the development of reliable, rapid and preferably portable analytical methods to quantify AA during the production and quality-control stages and in clinical applications [3-5]. Several methods for the determination of ascorbic acid concentration have been reported, such as HPLC [6], enzymatic analysis [7] and spectrophotometry [7]. However, these methods are relatively time-consuming and/or expensive.

The spectrophotometric method suffers from poor selectivity due to interference from other compounds present in commercial fruit juices (e.g., sugars or glucuronic acid) while citrate may affect enzymatic methods [7]. Electrochemical techniques, particularly cyclic voltammetry (CV) and square-wave voltammetry (SWV), have been employed as alternative tools for the evaluation of antioxidant activity [8]. These methods are attractive because of the speed of analysis, simplicity and low cost of the instrumental requirements.

Ascorbic acid oxidation at a bare glassy carbon electrode (GCE) generally occurs at a relatively high oxidation potential (e.g., 400 mV versus Ag/AgCl electrode), indicating a slow electron-transfer rate at the GCE [9]. Such sluggish electrode kinetics may also be due to electrode fouling caused by the deposition of oxidation product(s) of AA on the electrode surface, which results in poor selectivity and reproducibility, thus limiting the use of bare GCEs in quantitative measurements. Presently there are increasing reports on the use of carbon nanotubes (CNTs) in electroanalysis [10].

CNTs may be multiwalled or single-walled depending on the number of layers of carbon atoms in the nanotubes [11,12]. CNTs have unique geometric, mechanical, electronic and chemical properties. They possess a high aspect ratio (length/diameter) [13] and large surface areas (typically 200–300 m^2/g) and, hence, potentially high electroactivity [14]. The defects present at the open ends of the CNTs have been observed to produce relatively low peak potentials and high peak currents in the voltammetry of several electroactive molecules at electrodes modified with CNTs [14,15]. Nafion, a perfluorosulfonated polymer with cation-exchange properties, has been used to stably confine insoluble particles on electrode surfaces as well as to protect the electrode from fouling during electrochemical studies, thus improving the performance of the modified electrode [16-18]. Multiwalled CNT (MWCNT)-modified GCEs exhibited signals enhanced by about five-fold in the detection of dopamine in the presence of AA [17]. Jacobs et al. [19] reviewed the use of MWCNTs to obtain enhanced signals in the detection of substances such as carbohydrates, nucleic acids, glucose, pesticides, and serotonin, with similar reports relating to trace metals [20] and nitroaromatic compounds [21].

This study reports the use of a MWCNT-modified GCE for the direct analysis of ascorbic acid by SWV and the application of the method to the analysis of ascorbic acid in commercial orange-juice products. The reliability of SWV method was validated against HPLC, an independent non-electrochemical analytical technique.

Results and Discussion

CV and SWV at a bare GCE

CV provides an excellent and convenient tool to determine whether an electrochemical reaction is diffusion-controlled or kinetically controlled. The oxidation of 2 mmol/L ascorbic acid by using CV at a bare GCE was studied over the potential scan rates 25–200 mV/s. The left panel of Figure 1 shows a typical CV scan and a SWV scan for comparison. The plot on the right panel shows a good linear relationship between the observed CV peak current and the square root of the scan rate ($v^{1/2}$), demonstrating that the oxidation process is diffusion-controlled [22].

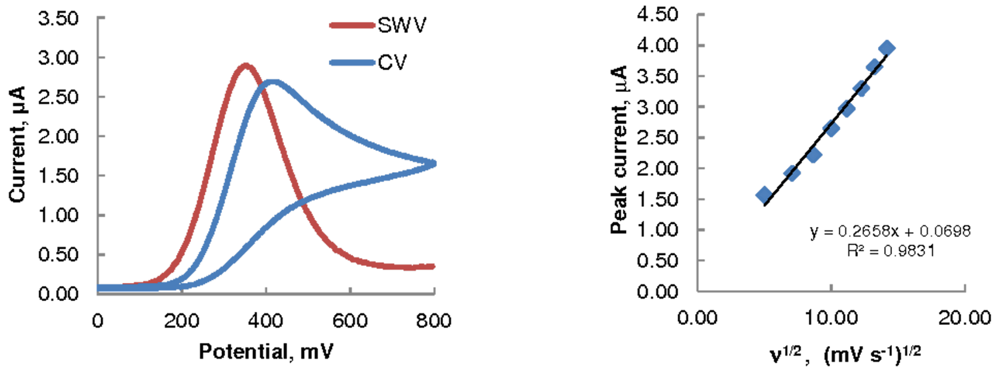

Figure 1: Typical CV and SWV voltammograms (left) at a bare GCE, 2 mmol/L AA in 0.1 M acetate buffer (pH 3.7), scan rate = 75 mV/s; dependence of CV peak currents on the scan rate v (right).

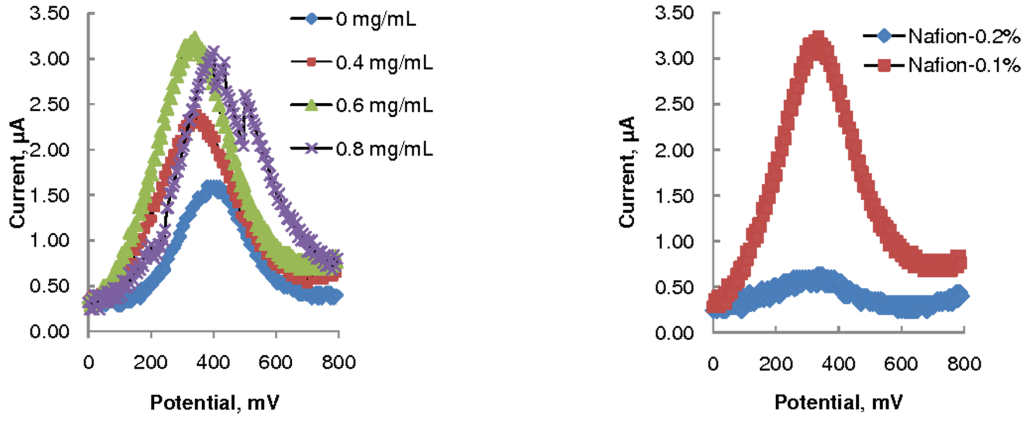

Figure 2: SWV of 1 mmol/L AA (in 0.1M acetate buffer, pH 3.7), scan rate = 75 mV/s: influence of varying the MWCNTs concentration (left) and Nafion concentration (right).

The mean peak potentials for the oxidation of ascorbic acid occurred at 418 mV (±7.2% rsd) and at 395 mV (±6.6% rsd) in CV and SWV, respectively. The net peak current was slightly higher (by ca. 7%) in SWV than in CV at all concentrations of ascorbic acid studied. The small negative shift (23 mV) of the peak potential observed in SWV relative to that observed in CV suggests that the applied square-wave potential helped maintain the electrode surface activity (through reduced adsorption of the oxidation products), resulting in a more favourable AA oxidation process. SWV was therefore chosen in this study for the development of the analytical method for AA analysis.

GCE surface modification

The effect of using an increasing concentration of MWCNTs in 0.1% (w/v) Nafion solution to modify the GCE is depicted in the voltammograms of 1 mmol/L AA in 0.1 M acetate buffer presented in Figure 2. The left panel shows that the maximum current response occurred at 0.6 mg/mL MWCNTs, which was nearly twice the response observed at the electrode modified only with Nafion (0.0 mg/mL MWCNTs). At 0.8 mg/mL MWCNTs the current was not stable, and no voltammogram could be recorded at 1 mg/mL MWCNTs. This suggests that at the higher concentrations the MWCNTs aggregated on the GCE could not be efficiently retained by the Nafion membrane, leading to a rather unstable layer structure [23,24]. Therefore, 0.6 mg/mL MWCNTs was employed in further SWV experiments.

With the MWCNT concentration fixed at 0.6 mg/mL, the influence of Nafion concentration (0.05–0.2%) on the voltammetric response was studied. No stable response could be recorded at 0.05% (w/v) Nafion. Stable responses were obtained at 0.1% (w/v) Nafion, but dramatically lower responses were recorded at 0.2% (w/v) Nafion. The lowest Nafion concentration was apparently unable to keep the MWCNTs attached to the GCE, whereas at the highest concentration the Nafion membrane was probably too thick with the result that it inhibited access of the analyte to the electrode. Further electroanalytical experiments therefore used GCE modified with 0.6 mg/mL MWCNTs in 0.1% (w/v) Nafion. The stability of the modified electrode was demonstrated in 100 CV scans (between 0 and 800 mV at 75 mV scan rate) in 0.25 mmol/L AA. The modified electrode showed only a 4% decrease in peak current over the 100 cycles, thus demonstrating a very stable and effective MWCNTs/Nafion film on the GCE.

Effect of pH

The influence of pH on the oxidation of ascorbic acid was investigated over the pH range 3.7–7.5. The highest SWV response for AA oxidation was observed at pH 3.7; the peak currents were found to decrease with increasing pH (Figure 3). At pH 3.7 molecular ascorbic acid is present in a relatively large proportion (estimated to be about 72% at pH 3.7 for pK_{a1} = 4.10

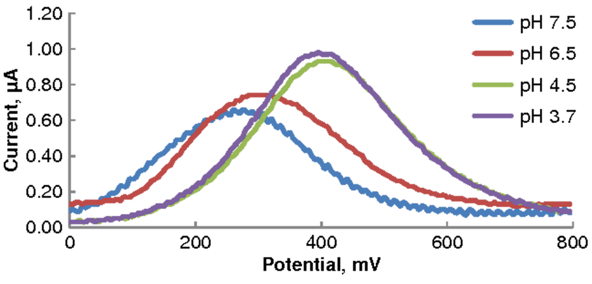

Figure 3: SWV on MWCNT–GCE, 0.25 mmol/L AA in different pH media (phosphate buffer, pH 6.5 and 7.5; acetate buffer, pH 3.7 and 4.5); scan rate = 75 mV/s.

and pK_{a2} = 11.79 [25]), making it compatible with the cation-exchange nature of the Nafion film; pH much higher than pK_{a1} would produce more anionic AA, which would be repelled by the Nafion membrane. The relatively low pH apparently also helped neutralise some of the negative charge on the Nafion surface. All subsequent SWV analyses were performed in 0.1 M acetate buffer (pH 3.7).

Analytical performance of the SWV method

Figure 4 shows SWV voltammograms in 0.25–5.0 mmol/L AA, with peak currents increasing linearly with AA concentration. The MWCNT–GCE responses were nearly three-fold higher than those obtained at the bare GCE, demonstrating the electrocatalytic action of MWCNTs. The peak potentials at the MWCNT–GCE shifted negatively by almost 80 mV compared with those obtained on the bare GCE, consistent with the observation of Fei et al. [15], who used CV at a GCE modified with a composite film of single-walled carbon nanotubes and dihexadecyl hydrogen phosphate for the determination of ascorbic acid concentration and reported a negative shift of up to 468 mV.

Table 1 shows that the calibration plot (dynamic concentration range = 0.0047–5.0 mmol/L) obtained on MWCNT–GCE showed better linearity (R^2 = 0.994) than that on the bare GCE (R^2 = 0.984). In addition, the calibration sensitivity (the slope of the regression equation) for the modified electrode was 2.8 times higher than that of the bare electrode. Table 1 also shows that better repeatability and reproducibility of both peak currents and peak potentials were observed on the modified GCE compared to the bare GCE, demonstrating clearly that the

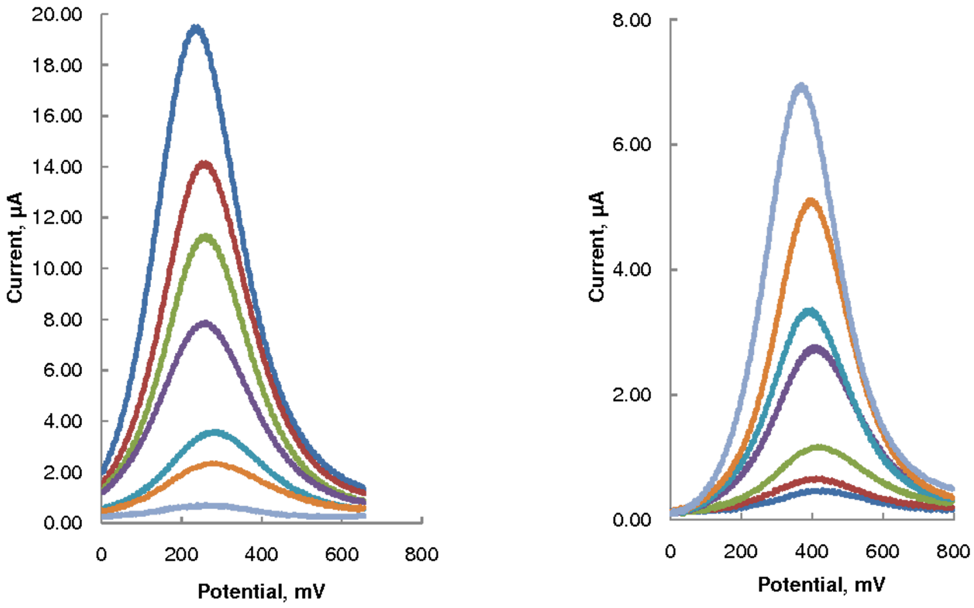

Figure 4: SWV in increasing AA concentrations (0.25–5.0 mmol/L in 0.1 M acetate buffer, pH 3.7); scan rate = 75 mV/s; at MWCNT–GCE electrode (left) and at bare GCE (right). (See Table 1 for the linear characteristics of the corresponding plots of the peak current vs AA concentration.)

Table 1: Analytical performance of the SWV method.

analytical parameter	MWCNT–GCE	bare GCE
dynamic AA concentration range (mmol/L)	0.0047–5.0	0.028–5.0
calibration sensitivity (slope of regression equation)	3.71	1.32
R^2	0.994	0.984
LOD (µmol/L)	1.4	8.3
LOQ (µmol/L)	4.7	28
mean peak potential (n = 5) and repeatability (% rsd), 1 mmol/L AA	313 mV (±3.8%)	395 mV (±6.6%)
mean peak current (n = 5) and repeatability (% rsd), 1 mmol/L AA	3.41 µA (±3.5%)	1.17 µA (±7.5%)
mean peak potential (n = 5) and reproducibility (% rsd), 1 mmol/L AA	313 mV (±3.4%)	387 mV (±6.8%)
mean peak current (n = 5) and reproducibility (% rsd), 1 mmol/L AA	3.13 µA (±3.2%)	1.21 µA (±6.3%)

modified electrode was protected from fouling by the Nafion membrane.

The limit of detection (LOD) (based on 3 × standard deviation of the blank) and the limits of quantitation (LOQ) (based on 10 × standard deviation) were much lower for the modified electrode than for the bare GCE (Table 1). The estimated LOD was better than that (2.8 μmol/L) reported by Zhang and Jiang [26], who used CV at a glassy carbon electrode modified with gold nanoparticles for the analysis of AA.

Analysis of ascorbic acid in commercial orange-juice products

Calibration-curve technique

The ascorbic acid contents of four brands (labelled simply as 1–4) of commercial orange-juice products were determined by SWV on MWCNT–GCE using the external-standard calibration technique. Typical SWV voltammograms are shown in Figure 5 and the results are presented in Table 2 (together with those obtained by the HPLC method, which are discussed later). It is seen that the measured AA content of the (1/5) diluted juice samples agreed very well (96–104%) with the claim on the product label.

Recovery test

Recovery tests were performed to establish the reliability of the SWV method. The diluted juice samples were spiked with 0.5 mmol AA and analysed. It is seen from Table 2 that, with the exception of juice 3, excellent recoveries of the spiked amount (92–103%) were obtained by SWV.

SWV using the standard-addition technique

The standard-addition technique (Figure 6) was applied in the analysis of the juice 3 (which gave the lowest recovery) to verify whether there were any matrix effects. The AA concentration of the (1/5)-diluted juice was found to be 0.471 mmol/L. Since this differed only by 4.4% from the result obtained by the calibration-curve technique (Table 2) no significant matrix effects were evident in the analysis.

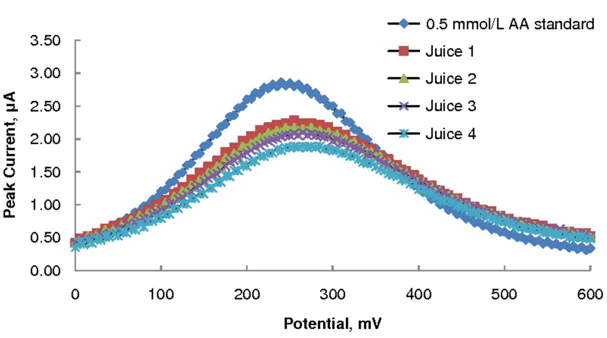

Figure 5: SWV voltammograms of four commercial orange juice samples (diluted by 1/5) in acetate buffer, pH 3.7; 0.5 mmol/L AA standard shown for comparison.

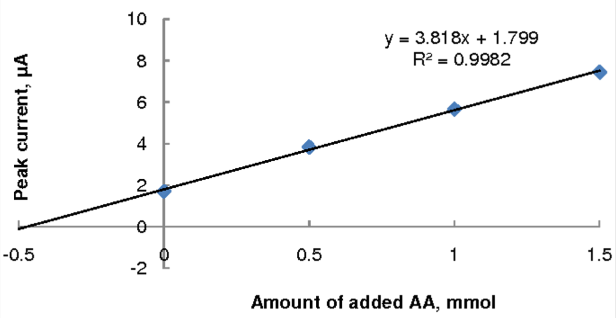

Figure 6: Standard addition plot of SWV data for (1/5)-diluted juice 3.

HPLC of ascorbic acid

Typical chromatograms of a juice sample and the AA standard (retention time = 1.862 min) are shown in Figure 7. An excellent linear correlation ($R^2 = 0.998$) between the AA peak area and standard AA concentrations (dynamic concentration range = 0.0023–5.0 mmol/L) was observed. The method

Table 2: Ascorbic acid content of commercial orange-juice samples.

	juice 1	juice 2	juice 3	juice 4
AA concentration (1/5 product-label claim)	0.454 mmol/L (8 mg/100mL)			
mmol/L AA (1/5)-diluted sample, SWV ± sd	0.435 ± 0.011	0.474 ± 0.016	0.451 ± 0.010	0.469 ± 0.017
% AA (relative to label claim), SWV	95.8	104.4	99.3	103.3
mmol/L AA (1/5)-diluted sample, HPLC ± sd	0.462 ± 0.011	0.439 ± 0.009	0.464 ± 0.015	0.461 ± 0.011
% AA (relative to label claim), HPLC	101.8	96.7	102.2	101.5
mmol/L AA spiked sample (SWV)	0.951	0.973	0.912	0.981
% recovery (SWV)	103	99.8	92.2	102.4
mmol/L AA spiked sample (HPLC)	0.965	0.931	0.942	0.951
% recovery (HPLC)	101	98.4	95.6	98.0

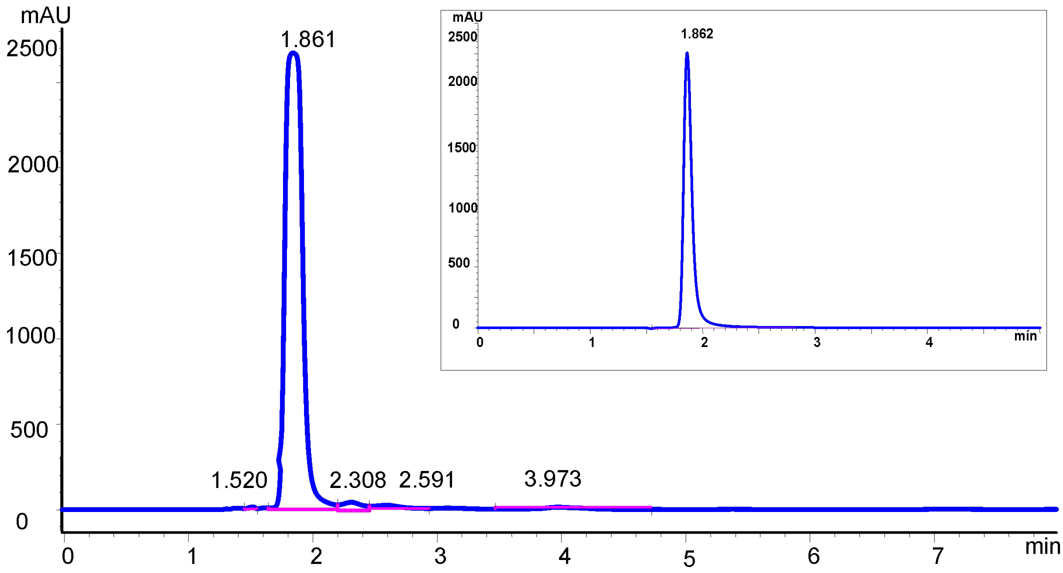

Figure 7: Typical HPLC chromatograms of sample of (1/5)-diluted juice 1 and 0.5 mmol/L AA standard (inset).

showed excellent precision (2.1% and 2.4% for repeatability and reproducibility, respectively). The better precision of the HPLC data compared to the SWV data is attributed to the auto-injection facility of the HPLC equipment. The LOD and LOQ were 0.7 and 2.3 µmol/L, respectively. The LOD is approximately half that (1.53 µmol/L) reported by Burini [27], who used a C_{18} column with a mobile phase of 80 mM phosphate buffer (pH 7.8) and methanol.

Triplicate HPLC analyses of the same four brands of commercial orange juice were performed. The chromatograms showed AA eluting at 1.86 min with no major additional peaks observed (Figure 7). The percentage recoveries in the spiked samples (see Table 2) analysed by HPLC were excellent (95–101%). Fresh fruit juices may contain a number of organic acids (e.g., citric acid) and sugars (e.g., glucose, fructose and sucrose), which could cause potential interferences. However no such interferences were evident in the analyses.

Comparison of the SWV method with the HPLC method

The results of the HPLC method were compared statistically with those of the SWV method. Table 3 shows that the calculated *F*-value for each juice analysed was less than the tabulated *F*-value ($P = 0.05$) for a two-tailed test, indicating that the precisions of the means of the two methods (SWV and HPLC) were not significantly different for all of the juice samples studied. Comparison of the mean (three replicates) AA content of each commercial orange juice obtained by the two methods (SWV and HPLC) using the *t*-test showed that for each juice analysed there was no significant difference ($P = 0.05$) between the mean values obtained by the two methods (see Table 3).

Table 3: Comparison of the results of SWV and HPLC methods.

statistic	juice 1	juice 2	juice 2	juice 4
calculated *F*	1.15	3.42	2.13	2.32
tabulated *F* (*P* = 0.05, 2-tailed) [28]	39			
calculated *t*	2.01	2.24	1.22	1.83
critical *t* (*P* = 0.05) [28]	4.303			

Conclusion

The MWCNTs-modified GCE was stable over 100 CV runs with the peak currents decreasing by only 4%. The SWV method at the bare GCE was found to be more sensitive than CV for the determination of the concentration of ascorbic acid. The excitation by a square-wave potential probably helped minimise fouling of the electrode surface caused by the oxidation products of AA, which probably caused the poorer reproducibility and sensitivity observed in the CV technique. The SWV method on MWCNT–GCE for AA analysis showed good analytical performance in terms of linearity, repeatability and reproducibility, and limit of detection or quantitation. The AA oxidation peak potential observed in SWV shifted negatively by 80 mV at the modified GCE compared with bare GCE, indicating a more favourable oxidation process in the presence of

MWCNTs. The sensitivity of the modified GC electrode increased by a factor of 2.8 and is attributed to the increased surface area provided by the MWCNT coating on the GCE, and to enhanced electrochemical activity from edge-plane defects at the MWCNTs facilitating the electron transfer. The LOD and LOQ of the SWV method at the MWCNT–GCE were only twice the limits obtained with the HPLC method. This is rather impressive considering the much simpler SWV instrumentation compared to the HPLC system. The SWV method proved its reliability in the analyses of AA in samples of orange juice, with good recoveries comparable to those obtained by HPLC. The mean AA contents obtained by the two methods were not significantly different ($P = 0.05$). The SWV method has clear advantages over the HPLC method: it is simple, precise, reliable and rapid, and notably (for the application tested) did not require any special pretreatment of the sample. The analysis time spent on SWV manipulations and measurement was less than 15 min, making the method suitable for routine analyses. Using CNTs to modify conventional electrodes (such as the popular GCE) is a simple and effective approach to enhance the electrode sensitivity for trace analyses.

Experimental

Electrodes and electrochemical instrumentation

All voltammetric measurements were performed in a 20 mL glass vial with a lid that had ports to accommodate the three mini electrodes (Cypress System, Chelmsford, MA, USA): the GCE ($d = 1$ mm) working electrode, platinum-wire auxiliary electrode ($d = 0.5$ mm), and a Ag|AgCl (leak-free) reference electrode. All potentials are reported against the Ag|AgCl reference electrode. Cyclic and square-wave voltammetric experiments were carried out at room temperature (23–25 °C) by using a MacLab potentiostat interfaced to a PowerLab 400 and controlled by the EChem v1.5 software (all components from eDAQ, Denistone, NSW, Australia). SWV (SW amplitude = 15 mV, frequency = 20 Hz) voltammograms of ascorbic acid were recorded from 0–800 mV at a scan rate of 75 mV/s.

Reagents

The multiwalled carbon nanotubes (diameter: 6–13 nm, length: 2.5–20 µm, purity > 99.8%) and Nafion (5% (w/v) in a mixture of lower aliphatic alcohols) were purchased from Sigma Aldrich (St. Louis, MO, USA). L-ascorbic acid was obtained from BDH Chemicals (Port Fairy, VIC, Australia). All other chemicals (HCOOH, K_2HPO_4, KH_2PO_4, KOH, CH_3COOH, $C_2H_3NaO_2$, and HNO_3) used in this work were of analytical reagent grade and obtained from Ajax Chemicals (Sydney, NSW, Australia). All standard solutions were prepared with ultrapure Milli-Q water (18.2 MΩ·cm; Milli-Q System, Millipore, Molsheim, France).

Electrode Preparation

Prior to its use or modification with MWCNTs, the working GCE was polished on a microcloth (Buehler**,** Lake Bluff, IL, USA) in a slurry of 0.05 µm alumina (Buehler, Lake Bluff, IL, USA) in Milli-Q water until the surface showed a mirror-like finish. The electrode was then rinsed with Milli-Q water, sonicated for 1 min to remove trace alumina particles from the electrode surface, and then air dried. This cleaning procedure was applied before all voltammetric measurements were carried out. The platinum-wire auxiliary electrode was typically polished with a CarbiMet fine-grit polishing disc (Buehler, Lake Bluff, IL, USA) to remove any oxides of platinum formed on its surface, immersed in 10% (v/v) nitric acid for about 30 s, rinsed thoroughly with Milli-Q water and then air dried. The reference electrode was cleaned by thoroughly rinsing the tip with Milli-Q water and then air dried.

To determine the optimum concentration of MWCNTs needed to modify the glassy carbon electrode, suspensions of 0.0, 0.4, 0.6 and 1.0 mg MWCNTs were dispersed in separate 1 mL aliquots of 0.1% (w/v) Nafion/ethanol and sonicated for 1.5 h. On the polished GCE, 5 µL of each suspension were applied evenly, and the ethanol was allowed to evaporate at room temperature for 1 h. The modified electrode was then washed repeatedly with Milli-Q water to remove any remaining modifying solution and kept at room temperature until use. The influence of Nafion concentration was determined by varying its concentration (0.05, 0.10, 0.20% (w/v) in ethanol) while keeping the MWCNTs at 0.6 mg/mL. The homogeneity of the dispersion of MWCNTs in the Nafion film (at the optimum concentrations of MWCNTs and Nafion) was ascertained by applying a few microlitres of the modifying solution on a glass slide, allowing the ethanol to evaporate and viewing the dried film through a digital optical microscope.

HPLC analyses

HPLC analyses were performed on an Agilent 1200 system (Agilent Technologies Pty Ltd Australia, Mulgrave, VIC) controlled by the Agilent ChemStation software. The column was an Agilent Zorbax Eclipse XDB-C_{18} (15 × 0.46 cm, particle size = 5 µm, total carbon content = 10%, surface area = 1800 m^2/g and average pore diameter = 80 nm). The chromatographic conditions used were: mobile phase 0.1% (v/v) formic acid in Milli-Q water [29], flow rate 1 mL/min, injection volume 20 µL and detection wavelength = 245 nm.

Standard AA solutions; repeatability or reproducibility tests

Stock (250 mmol/L) standard AA solutions were prepared either in 0.1 M phosphate buffer (pH 6.5 or pH 7.5) or in 0.1 M acetate buffer (pH 3.7 or pH 4.5). Five replicate SWV runs in

1 mmol/L AA were conducted on a single day (to test the repeatability of the SWV response) and over five days, by using freshly prepared modified electrodes and AA solutions (to assess reproducibility). For HPLC work, stock standard (250 mmol/L) AA solution was prepared in 0.1% (v/v) formic acid/ Milli-Q water (pH 2.7 approx). Three samples of freshly prepared 0.5 mmol/L AA solutions were run on one day to establish the repeatability of the analytical response, while similar fresh preparations were run over three different days to establish reproducibility of the analytical response.

Analysis of commercial orange-juice products

Four brands (identified simply as 1–4) of commercial orange-juice products were obtained from a local supermarket. Juices were filtered through Whatman No.4 paper to remove fibre and pulp. For SWV, all juice samples were diluted (1/5) with 0.1 M acetate buffer (pH 3.7) for analysis. The same four brands of commercial orange juice were employed for HPLC analysis. The juice samples were likewise filtered to remove fibre and pulp. All juice samples were diluted (1/5) with 0.1% (v/v) formic acid/Milli-Q water for HPLC analysis.

Recovery tests

Recovery tests were performed in triplicate. To aliquots of the orange-juice products representing (1/5)-diluted orange-juice samples, 2 mL of 250 mmol/L standard ascorbic acid (equivalent to a spiked amount of 0.5 mmol AA) were added and then diluted in 100 mL standard flasks with 0.1 M acetate buffer (pH 3.7) or with 0.1% (v/v) formic acid/Milli-Q water for analysis by SWV or HPLC, respectively.

SWV by the standard addition method

Four lots of 100 mL solutions of (1/5)-diluted juice (i.e., containing 0.454 mmol/L of AA, as per the product-label claim) were prepared in 100 mL standard flasks. Aliquots of 0.0, 2.0, 4.0, 6.0 mL of 250 mmol/L standard AA solution were added into separate juice sample flasks representing 0.0, 0.5, 1.0 and 1.5 mmol of added AA and then diluted to volume.

References

1. Linster, C. L.; Van Schaftingen, E. *FEBS J.* **2007,** *274,* 1–22. doi:10.1111/j.1742-4658.2006.05607.x
2. Rumsey, S. C.; Levine, M. *J. Nutr. Biochem.* **1998,** *9,* 116–130. doi:10.1016/S0955-2863(98)00002-3
3. Bremus, C.; Herrmann, U.; Bringer-Meyer, S.; Sahm, H. *J. Biotechnol.* **2006,** *124,* 196–205. doi:10.1016/j.jbiotec.2006.01.010
4. Liu, Y.; Huang, J.; Hou, H.; You, T. *Electrochem. Commun.* **2008,** *10,* 1431–1434. doi:10.1016/j.elecom.2008.07.020
5. Zerdin, K.; Rooney, M. L.; Vermuë, J. *Food Chem.* **2003,** *82,* 387–395. doi:10.1016/S0308-8146(02)00559-9
6. Esteve, M. J.; Farré, R.; Frigola, A.; López, J. C.; Romera, J. M.; Ramirez, M.; Gil, A. *Food Chem.* **1995,** *52,* 99–102. doi:10.1016/0308-8146(94)P4188-L
7. Nováková, L.; Solich, P.; Solichová, D. *TrAC, Trends Anal. Chem.* **2008,** *27,* 942–958. doi:10.1016/j.trac.2008.08.006
8. Barros, L.; Falcão, S.; Baptista, P.; Freire, C.; Vilas-Boas, M.; Ferreira, I. C. F. R. *Food Chem.* **2008,** *111,* 61–66. doi:10.1016/j.foodchem.2008.03.033
9. Zhang, M.; Gong, K.; Zhang, H.; Mao, L. *Biosens. Bioelectron.* **2005,** *20,* 1270–1276. doi:10.1016/j.bios.2004.04.018
10. Rivas, G. A.; Rubianes, M. D.; Rodríguez, M. C.; Ferreyra, N. F.; Luque, G. L.; Pedano, M. L.; Miscoria, S. A.; Parrado, C. *Talanta* **2007,** *74,* 291–307. doi:10.1016/j.talanta.2007.10.013
11. Coleman, J. N.; Khan, U.; Blau, W. J.; Gun'ko, Y. K. *Carbon* **2006,** *44,* 1624–1652. doi:10.1016/j.carbon.2006.02.038
12. Merkoçi, A.; Pumera, M.; Llopis, X.; Pérez, B.; del Valle, M.; Alegret, S. *TrAC, Trends Anal. Chem.* **2005,** *24,* 826–838. doi:10.1016/j.trac.2005.03.019
13. Popov, V. N. *Mater. Sci. Eng., R* **2004,** *43,* 61–102. doi:10.1016/j.mser.2003.10.001
14. Wildgoose, G. G.; Banks, C. E.; Leventis, H. C.; Compton, R. G. *Microchim. Acta* **2006,** *152,* 187–214. doi:10.1007/s00604-005-0449-x
15. Fei, J.; Wu, K.; Yi, L.; Li, J. *Bull. Korean Chem. Soc.* **2005,** *26,* 1403–1409. doi:10.5012/bkcs.2005.26.9.1403
16. Lee, S.-J.; Yu, T. L.; Lin, H.-L.; Liu, W.-H.; Lai, C.-L. *Polymer* **2004,** *45,* 2853–2862. doi:10.1016/j.polymer.2004.01.076
17. Wu, K.; Hu, S. *Microchim. Acta* **2004,** *144,* 131–137. doi:10.1007/s00604-003-0103-4
18. Yang, S.; Yang, R.; Li, G.; Qu, L.; Li, J.; Yu, L. *J. Electroanal. Chem.* **2010,** *639,* 77–82. doi:10.1016/j.jelechem.2009.11.025
19. Jacobs, C. B.; Peairs, M. J.; Venton, B. J. *Anal. Chim. Acta* **2010,** *662,* 105–127. doi:10.1016/j.aca.2010.01.009
20. Hwang, G. H.; Han, W. K.; Park, J. S.; Kang, S. G. *Talanta* **2008,** *76,* 301–308. doi:10.1016/j.talanta.2008.02.039
21. Liu, Y.; Lan, D.; Wanzhi, W. *J. Electroanal. Chem.* **2009,** *637,* 1–5. doi:10.1016/j.jelechem.2009.09.021
22. Yilmaz, S.; Sadikoglu, M.; Saglikoglu, G.; Yagmur, S.; Askin, A. *Int. J. Electrochem. Sci.* **2008,** *3,* 1534–1542.
23. Lee, D. Y.; Lee, M.-H.; Kim, K. J.; Heo, S.; Kim, B.-Y.; Lee, S.-J. *Surf. Coat. Technol.* **2005,** *200,* 1920–1925. doi:10.1016/j.surfcoat.2005.08.024
24. Wu, P.; Li, B.; Du, H.; Gan, L.; Kang, F.; Zeng, Y. *J. Power Sources* **2008,** *184,* 381–384. doi:10.1016/j.jpowsour.2008.03.020
25. *Handbook of Chemistry and Physics,* 51th ed.; Chemical Rubber Pub. Co.: Cleveland, Ohio, 1970.
26. Zhang, L.; Jiang, X. *J. Electroanal. Chem.* **2005,** *583,* 292–299. doi:10.1016/j.jelechem.2005.06.014
27. Burini, G. *J. Chromatogr., A* **2007,** *1154,* 97–102. doi:10.1016/j.chroma.2007.03.013
28. Levine, D. M.; Berenson, M. L.; Stephan, D.; Krehbiel, T. C.; Ng, P. T. *Statistics for managers using Microsoft Excel,* 5th ed.; Prentice Hall: Upper Saddle River, NJ, 2007.
29. Rodríguez-Bernaldo de Quirós, A.; Fernández-Arias, M.; López-Hernández, J. *Food Chem.* **2009,** *116,* 509–512. doi:10.1016/j.foodchem.2009.03.013

License and Terms

Beilstein Journal
of Nanotechnology

Conducting composite materials from the biopolymer kappa-carrageenan and carbon nanotubes

Ali Aldalbahi[1,§], Jin Chu[2], Peter Feng[2] and Marc in het Panhuis[*1]

Full Research Paper

Open Access

Address:
[1]Soft Materials Group, School of Chemistry, and ARC Centre of Excellence for Electromaterials Science, University of Wollongong, Wollongong, NSW 2522, Australia and [2]Institute of Functional Nanomaterials and Department of Physics, University of Puerto Rico, San Juan, Puerto Rico 00931, USA

Email:
Marc in het Panhuis* - panhuis@uow.edu.au

* Corresponding author
§ Present address: King Saud University, Riyadh 11451, Saudi Arabia

Keywords:
biopolymers; carbon nanotubes; carrageenan; composite materials; conductivity; mechanical; rheology

Beilstein J. Nanotechnol. **2012,** *3,* 415–427.
doi:10.3762/bjnano.3.48

Received: 14 March 2012
Accepted: 26 April 2012
Published: 23 May 2012

This article is part of the Thematic Series "Nanostructures for sensors, electronics, energy and environment".

Guest Editor: N. Motta

Abstract

Conducting composite films containing carbon nanotubes (CNTs) were prepared by using the biopolymer kappa-carrageenan (KC) as a dispersant. Rheological studies indicated that 0.5% w/v was the appropriate KC concentration for dispersing CNTs. Our results showed that multiwalled nanotubes (MWNTs) required less sonic energy than single-walled nanotubes (SWNTs) for the dispersion process to be complete. Films prepared by vacuum filtration exhibited higher conductivity and improved mechanical characteristics compared to those prepared by evaporative casting. All composite films displayed sensitivity to water vapour, but MWNT films were more sensitive than SWNT films.

Introduction

Carbon nanotubes (CNTs) have attracted attention due to their unique electronic, mechanical, optical and thermal properties, which make them suitable for applications in nanotechnology [1-4]. However, one of the main disadvantages of CNTs is their process-ability; they are difficult to disperse in most common solvents due to their high surface energy and van der Waals interactions [3,5-7]. To overcome this issue, a diverse range of molecules have been used to aid the dispersion of CNTs in aqueous media, such as surfactants, polymers and biopolymers [8-16]. Well known examples of surfactants and polymers include, sodium dodecyl sulfonate, Triton X-100 and polystyrene sulfonate [17-24]. In addition, it has been established that biopolymers such as gellan gum, xanthan gum, gum arabic and iota-carrageenan are effective for the dispersion of CNTs in aqueous solutions [8,25-29]. For example, gellan gum-CNT dispersions have been wet-processed by inkjet printing into optically transparent films, which displayed sensitivity to water vapour [30].

Other commonly employed wet-processing methods used to process biopolymer–CNT dispersions into materials include (but are not limited to) evaporative casting, vacuum filtration and fibre spinning [11,29]. Formation of films by evaporation is well-known and involves the controlled evaporation of the solvent from a CNT dispersion. It has been established that the mechanical and electrical characteristics of these CNT networks are contingent on the CNT/dispersant ratio. Increasing the nanotube concentration usually leads to an increase in the electrical conductivity and to mechanical reinforcement [31,32]. Vacuum filtration of dispersions usually results in films, which are generally referred to as buckypapers [9,33]. These films can be defined as an entangled network of CNTs, which are held together by van der Waals interactions at the CNT–CNT junctions and are arranged in a two-dimensional structure [34]. Although the formation of buckypapers is straightforward, it has been shown that the electrical, mechanical and physical characteristics are dependent on various parameters, such as the type of CNTs (SWNT or MWNT), the filtration substrate (pore size; hydrophilic or hydrophobic), the sonication time and the type of dispersant (surfactants or polymers) [9,33]. The electrical properties combined with their flexible nature makes CNT networks ideal for a number of potential applications, such as solar cells, displays, touch screens, sensors, electronic paper, supercapacitors and batteries [35-38].

Carrageenans are a biopolymer family of water-soluble, linear, sulfonated galactans extracted from various sources of the Rhodophyta (marine red algae). The carrageenans are well known for their gel-forming and thickening properties [39,40]. This biopolymer is an anionic polysaccharide whose structure contains galactose, 3,6-anhydrogalactose units, carboxy and hydroxy groups and ester sulfates. There are three types of carrageenan depending on the number of charged sulfated groups per biopolymer repeat unit, i.e., kappa-carrageenan (one group), iota-carrageenan (two groups) and lambda-carrageenan (three groups) [39]. Carrageenans have been extensively employed in the food industry and are commonly referred to as E407 (European Union specification) as well as being approved by the US Food and Drug Administration as a direct food additive [40]. Recent demonstrations of other applications include their use in drug delivery for the inhibition of viral infections [41,42].

Glycerin (or glycerol, glycerine) is a polyol compound widely used in a diverse range of industries. For example, in the food industries it is added as a humectant, while it is also used to produce an essential ingredient (glyceryl nitrate) for explosives. Of particular relevance to the research presented in this paper is its usage as a plasticizer to increase the flexibility of polymer films [43].

In this work, it is shown that kappa-carrageenan (KC) is a suitable dispersant for the stabilization of SWNTs and MWNTs in water. The KC concentration and sonication time were optimised to facilitate the efficient dispersion of these CNTs. The electrical and mechanical characteristics of free-standing composite films prepared by evaporative casting and vacuum filtration were assessed, including the effect of incorporating the plasticizer glycerin. The gas-sensing ability of these composite films is demonstrated.

Results and Discussion

Rheological of carrageenan solutions

Rheology is a suitable method for following any changes in viscosity of gel-forming polymers, such as the carrageenans. This is an important step due to the adverse effect that the viscosity of a solution can have on the sonication process. Polymers undergo a dilute to semidilute transition resulting in a significant change in their viscosity. High viscosity is undesirable as it decreases CNT mobility, which impedes the efficiency of the dispersion process. Therefore, our initial studies focussed on establishing the appropriate biopolymer concentration using flow-curve analysis. The viscosity was measured as a function of shear rate for KC solutions over a concentration range of 0.2–1.2% w/v at 21 °C (Figure 1a). All KC solutions displayed shear-thinning behaviour, i.e., decreasing viscosity (η) with increasing shear rate ($\dot{\gamma}$). These flow curves were fitted to the well-known power-law model [44]:

$$\eta = K\dot{\gamma}^{n-1}, \tag{1}$$

where K and n indicate the “consistency” and power-law index, respectively. Figure 1a shows that the viscosity of KC solutions increased with increasing concentration. For example, the apparent viscosity of the KC solution (at shear rate 21 s^{-1}) increased from 16 mPa·s at 0.2% w/v to 3190 mPa·s at 1.2% w/v; whereas, the consistency of KC exhibited an increase from 33 ± 1 mPa·s^n to 21890 ± 48 mPa·s^n as the concentration was increased from 0.2 to 1.2% w/v. This behaviour is consistent with observations of other polysaccharides [45,46] and polymers in general [47].

Table 1 shows that KC solutions with a concentration <0.5% w/v have power-index values of ~0.8. However, for higher concentrations the solutions become more shear-thinning (n decreases), and thicker (K increases). Figure 1c shows a sharp increase in the apparent viscosity of the KC solution

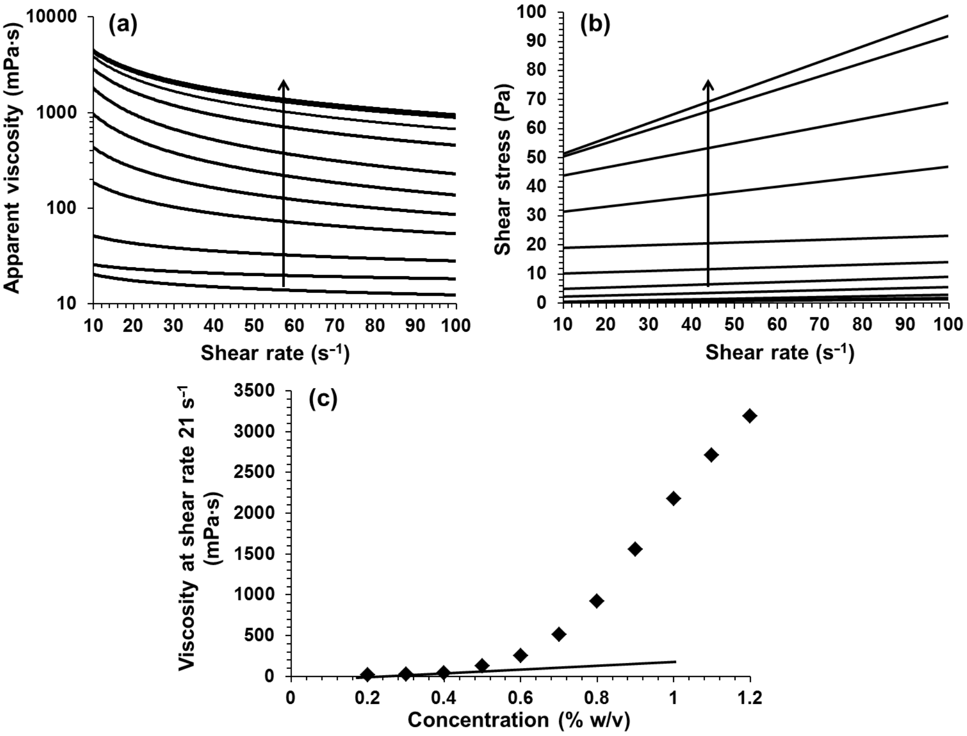

Figure 1: Effect of increasing concentration on (a) the viscosity and (b) the shear stress versus shear rate of KC solutions. The lines in (a) and (b) are fits to Equation 1 and Equation 2, respectively (measured data points omitted for clarity). The arrows indicate the direction of increase in KC concentration (0.2–1.2% w/v). (c) Viscosity at shear rate 21 s^{-1} as a function of concentration of KC. All samples were measured at 21 °C. The straight line in (c) indicates the rate of increase at the lower concentrations.

around 0.5% w/v, which is characteristic of dilute to semidilute transition.

The relation between shear stress and shear rate for IC solutions at different concentrations is shown in Figure 1b. It can be seen that KC solutions exhibit a yield point, i.e., the viscous KC solutions start to flow only when a certain amount of force is applied. This point can be determined by using approximations such as the Bingham model [44]:

$$\tau = \tau_B + \eta_B s, \tag{2}$$

where τ_B and η_B indicate the Bingham yield point and Bingham flow coefficient, respectively. Although the values obtained by

Table 1: Summary of rheology analysis of KC solutions at different concentrations (*c*). Consistency (*K*) and power-law index (*n*) values were obtained through curve fitting with the power-law model (Equation 1). Bingham yield point (τ_B) and Bingham flow coefficient (η_B) values were obtained by using the Bingham model (Equation 2). Values for all solutions were obtained over a shear-rate range of 10–100 s^{-1} and 21 °C.

c (% w/v)	*K* (mPa·s^n)	*n*	τ_B (Pa)	η_B (Pa·s)
0.2	33 ± 1	0.79 ± 0.01	0.11 ± 0.01	0.012 ± 0.001
0.3	36 ± 1	0.85 ± 0.01	0.11 ± 0.01	0.018 ± 0.001
0.4	94 ± 1	0.74 ± 0.01	0.37 ± 0.01	0.025 ± 0.001
0.5	637 ± 1	0.46 ± 0.01	1.88 ± 0.05	0.037 ± 0.001
0.6	2158 ± 2	0.30 ± 0.01	4.49 ± 0.06	0.044 ± 0.001
0.7	6725 ± 9	0.16 ± 0.01	9.87 ± 0.05	0.044 ± 0.001
0.8	14030 ± 12	0.11 ± 0.01	18.53 ± 0.18	0.047 ± 0.001
0.9	17718 ± 6	0.21 ± 0.01	29.79 ± 0.39	0.173 ± 0.006
1.0	20506 ± 42	0.24 ± 0.01	41.08 ± 0.89	0.279 ± 0.015
1.1	21058 ± 32	0.32 ± 0.01	45.78 ± 1.21	0.462 ± 0.019
1.2	21890 ± 48	0.33 ± 0.01	46.08 ± 0.54	0.529 ± 0.008

using the Bingham model are dependent on the shear-rate range, it provides a good approximation for the determination of yield points [44]. The model shows that, over a shear-rate range of 10–100 s^{-1}, the Bingham yield point and Bingham flow coefficient significantly increased with concentration. For example, the Bingham yield point of the KC solution (0.2% w/v) was 0.11 ± 0.01 Pa compared to 46.08 ± 0.54 Pa at a higher concentration (1.2% w/v), as shown in Table 1. Thus, it is clear that an increase in concentration results in an increase in Bingham yield point and Bingham flow coefficient.

It is well-known that rheology through dynamic modulus measurements can be used to determine the sol–gel transition of polymer solutions. A larger loss modulus (G″) than storage modulus (G′) in the linear viscoelastic region is indicative of solution-like behaviour. Whereas, the reverse (G′ > G″) is indicative of gel-like behaviour [44]. The KC solutions with concentrations below 0.5% w/v exhibited lower G′ values than G″ values (Figure 2a–c). As expected, by increasing the concentration, the loss and storage moduli increased (Figure 2d–e), but two distinct rates of increase were observed. Figure 2f shows this data expressed in terms of the loss factor, tan δ = G″/G′ at a fixed shear-strain value (1.47%). Values of tan δ > 1 indicate solution-like behaviour, whereas tan δ values ≤ 1 point towards gel-like behaviour. These results provide further evidence for a dilute to semidilute transition for KC concentrations around 0.5% w/v.

Optimisation of sonication time

A KC concentration (0.5% w/v) in the dilute range was selected to optimise the dispersion of CNTs at a concentration of 0.10% w/v. The optimum sonication time is defined as the

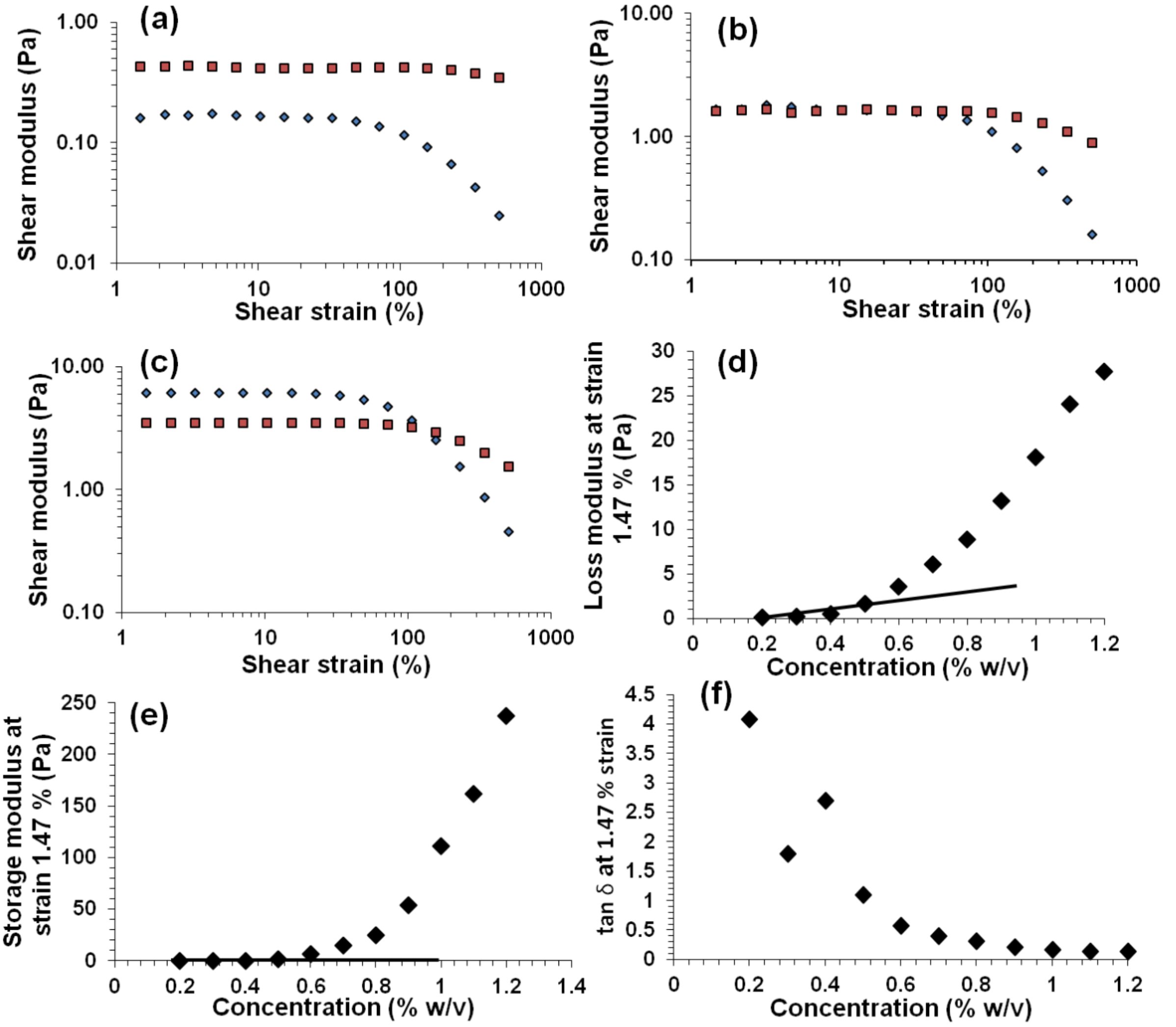

Figure 2: (a–c) Storage (G′, diamonds) and loss modulus (G″, squares) of KC solutions at concentrations of 0.4%, 0.5%, and 0.6% w/v, respectively; (d and e) loss and storage modulus of KC versus solution concentration at 1.47% shear strain, and (f) loss factor (tan δ = G″/G′) versus concentration for KC at 1.47% shear strain. The straight lines in (d and e) indicate the rate of increase at the lower concentrations.

minimum amount of time required to successfully disperse the CNTs [8]. This optimisation is necessary as it has been reported that excess sonication leads to damage of the nanotubes [15,48]. The optimum sonication time was determined as defined in [8], by establishing the time it takes for the UV–vis absorption intensity to level out and the visible aggregates to disappear. CNTs absorb at most wavelengths, while KCs do not exhibit any bands for wavelengths greater than 250 nm; thus, by monitoring a wavelength in this range the dispersion of CNTs can be monitored.

Figure 3a and Figure 3b show that the UV–vis absorbance intensity increases with sonication time, indicating that an increasing amount of CNTs became dispersed over time. The absorbance at an arbitrarily picked wavelength (660 nm) becomes independent of sonication after 20 and 35 min of sonication for MWNTs and SWNTs, respectively (Figure 3c). Optical microscopy revealed the presence of aggregates in the dispersions subjected to short sonication times (5 min), see Figure 3d. In contrast, after 20 and 35 min of sonolysis no aggregates were visible, suggesting that homogenous dispersions were achieved. Therefore, these sonication times (20 and 35 minutes) were selected as being optimal for ensuring that the MWNTs and SWNTs were well dispersed in the KC solution. Conversion of sonication time to energy shows that achieving complete dispersion of MWNTs and SWNTs requires 14.4 ± 0.8 kJ (~0.96 kJ per mg) and 25.2 ± 1.1 kJ (~1.68 kJ per mg), respectively (inset in Figure 3c), i.e. SWNTs are 1.75 times more costly to disperse than are MWNTs.

Stability and rheology of optimised dispersions

Wet-processing methods, such as vacuum filtration and evaporative casting, require dispersions that are stable for several days. Stability was assessed by monitoring of the UV–vis absorbance as a function of time. Figure 4a shows that the KC–CNT dispersions are reasonably stable for a period of at least 10 days. In addition, these dispersions appeared to be stable after two months of storage under controlled conditions (21 °C, RH = 45%, Figure 4b).

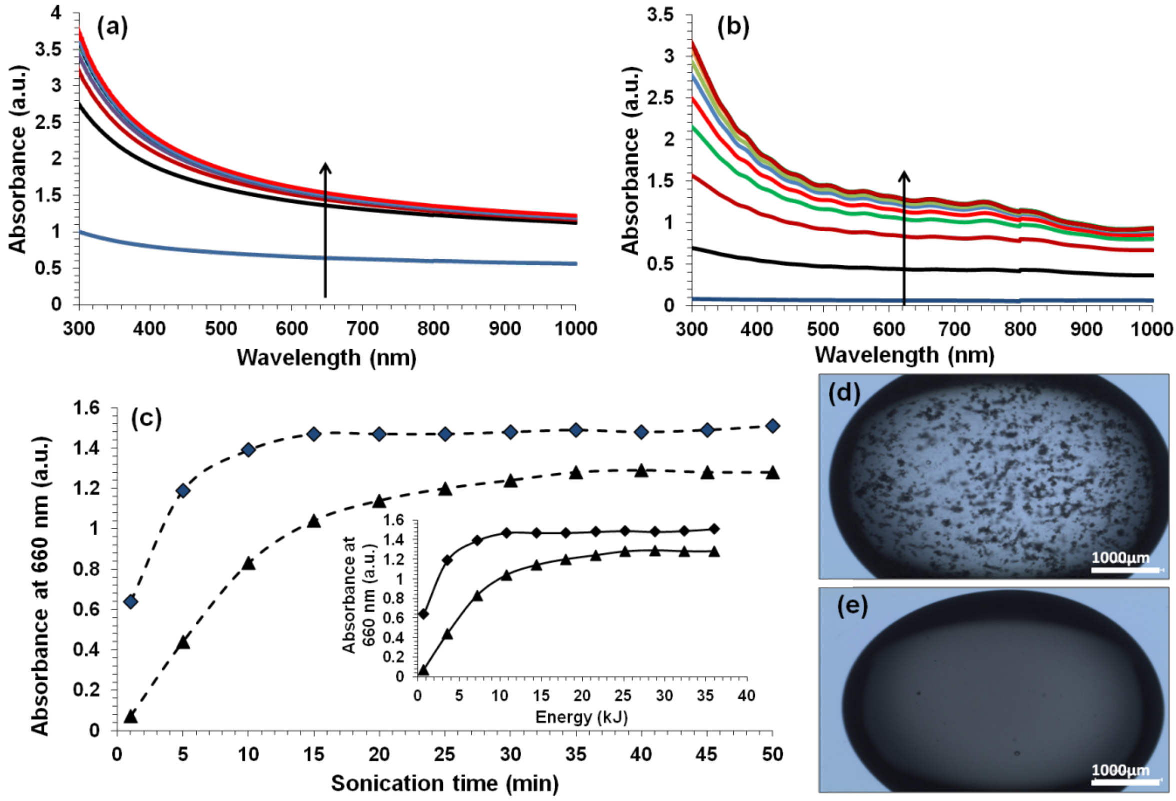

Figure 3: Effect of increasing sonication time on the UV–visible absorption spectrum of a dispersion containing (a) 0.10% w/v MWNTs and 0.50% w/v KC and (b) 0.10% w/v SWNTs and 0.50% w/v KC. (c) Absorbance at 660 nm versus sonication time and energy (inset) for KC–MWNT (diamonds) and KC–SWNT (triangles) dispersions. (d and e) KC–SWNTs after 5 and 35 minutes sonication, respectively. All samples were measured at 21 °C. Arrows indicate increasing sonication time.

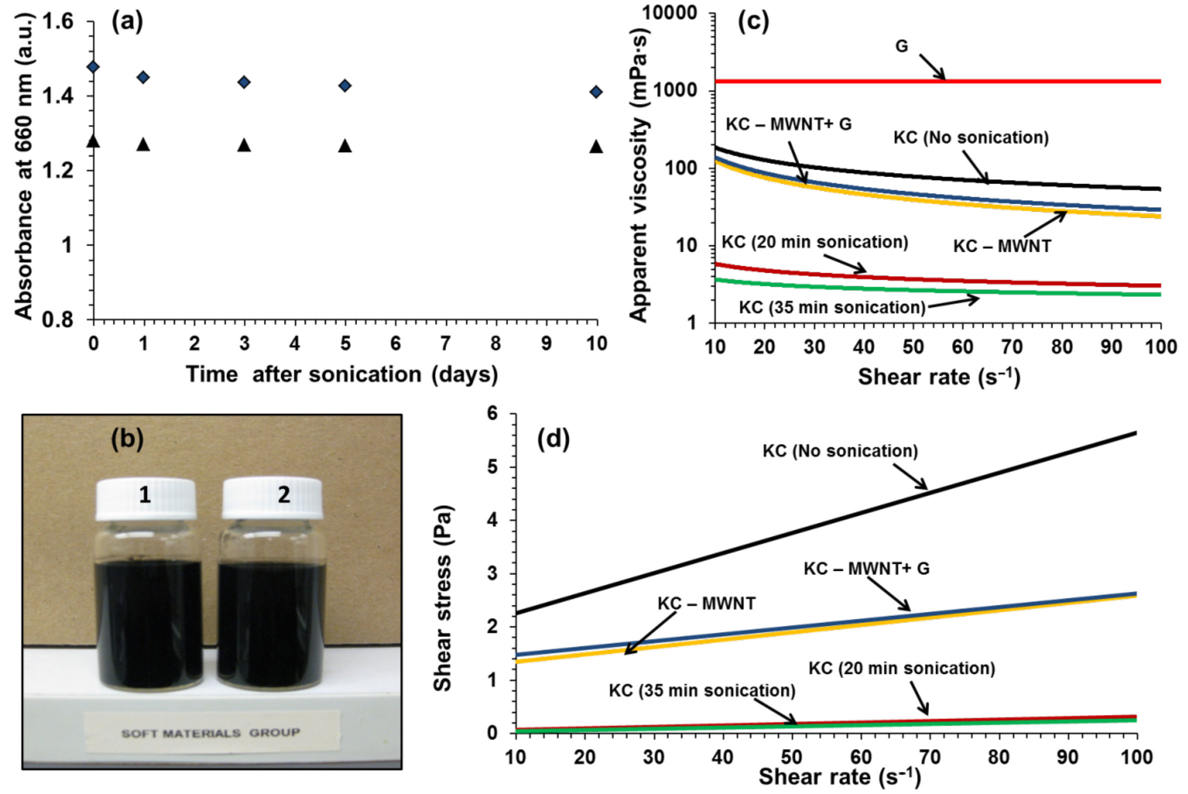

Figure 4: (a) UV–vis absorbance at 21 °C and at 660 nm wavelength for MWNT (diamonds) and SWNT (triangles) dispersions as a function of time. (b) Photographs of KC–MWNT (1) and KC–SWNT (2) dispersions after being left undisturbed for two months. (c) Apparent viscosity as a function of shear rate for undiluted glycerin (G), KC solutions (0.5% w/v) at different sonication times and KC–CNTs (KC concentration = 0.5% w/v, CNT concentration = 0.1% w/v) dispersions. (d) Shear stress versus shear rate of unsonicated KC, at different sonication times of KC solutions and KC–CNTs dispersions. The lines in (c) and (d) are fits to Equation 1 and Equation 2, respectively.

The flow curves of KC–CNT dispersions and sonicated KC solutions are shown in Figure 4b and Figure 4c. It is clear that the apparent viscosity and consistency of KC solutions decreased significantly during sonication, while the value of the power-law index increased (Table 2). For example, over 35 minutes of sonication the consistency decreased from 637.4 ± 4.4 mPa·s^n to 5.8 ± 0.1 mPa·s^n, while n increased from 0.46 to 0.80. This suggests that sonication results in solutions that are thinner (K decreases) and less shear-thinning (n increases). This is in excellent agreement with previous observations, i.e., sonolysis reduces the molecular weight of the biopolymer, and this is responsible for the observed reduction in

Table 2: Summary of rheological analysis over a shear-rate range of 10–100 s^{-1} at 21 °C for KC solutions, and KC–CNT and KC–CNT–G dispersions for different sonication times (ST). Concentrations of KC, CNT and G are 0.5% w/v, 0.10% w/v and 0.25% w/v, respectively. Consistency (K) and power-law index (n) values were obtained through curve fitting with the power-law model (Equation 1). Bingham yield point (τ_B) and Bingham flow coefficient (η_B) values were obtained using the Bingham model (Equation 2).

Sample	ST (min)	K (mPa·s^n)	n	τ_B (Pa)	η_B (Pa·s)
KC	0	637 ± 4	0.46 ± 0.01	1.88 ± 0.17	0.047 ± 0.003
KC	20	11.2 ± 0.2	0.72 ± 0.01	0.04 ± 0.01	0.003 ± 0.001
KC	35	5.8 ± 0.1	0.80 ± 0.01	0.02 ± 0.01	0.002 ± 0.001
G	0	1320.0 ± 0.1	0.99 ± 0.01	0.19 ± 0.02	1.314 ± 0.002
KC–MWNT	20	648.5 ± 4.4	0.28 ± 0.01	1.21 ± 0.02	0.014 ± 0.001
KC–MWNT–G	20	662.9 ± 5.7	0.32 ± 0.01	1.35 ± 0.01	0.013 ± 0.001
KC–SWNT	35	814.4 ± 4.4	0.21 ± 0.01	1.29 ± 0.01	0.010 ± 0.001
KC–SWNT–G	35	849.4 ± 8.5	0.26 ± 0.01	1.26 ± 0.01	0.014 ± 0.001

apparent viscosity [8,11,49]. The addition of CNTs resulted in dispersions that were thicker (*K* increases) and more shear-thinning (*n* decreases) than the corresponding sonicated KC solutions (Table 2). Similar observations were made for the Bingham parameters, i.e., sonolysis reduced the τ_B and η_B values, while the addition of CNT resulted in increased values. As expected, the addition of glycerin did not dramatically affect the flow properties of the KC-CNT dispersions. Glycerin is a Newtonian fluid, i.e., $n \sim 1$ indicating that its viscosity is independent of the shear rate (Table 2).

Electrical conductivity of films

Free-standing films were prepared by evaporative casting and vacuum filtration of KC–CNT dispersions. All films exhibited linear *I–V* characteristics, i.e., ohmic behaviour (Figure 5a). The total resistance (R_T) increased with channel length (Figure 5b), and was found to scale linearly with sample length according to [9,27]

$$R_T = \frac{1}{\sigma A} l + R_C \tag{3}$$

where l, A, σ and R_C are the length, cross-sectional area, electrical conductivity and contact resistance of the sample, respectively. The slope of the straight-line fit to Equation 3 can then be used to calculate the bulk conductivities (Table 3). Due to the difference in the density values of MWNTs (2.15 g/cm^3) and SWNTs (1.5 g/cm^3) it is not appropriate to compare in terms of

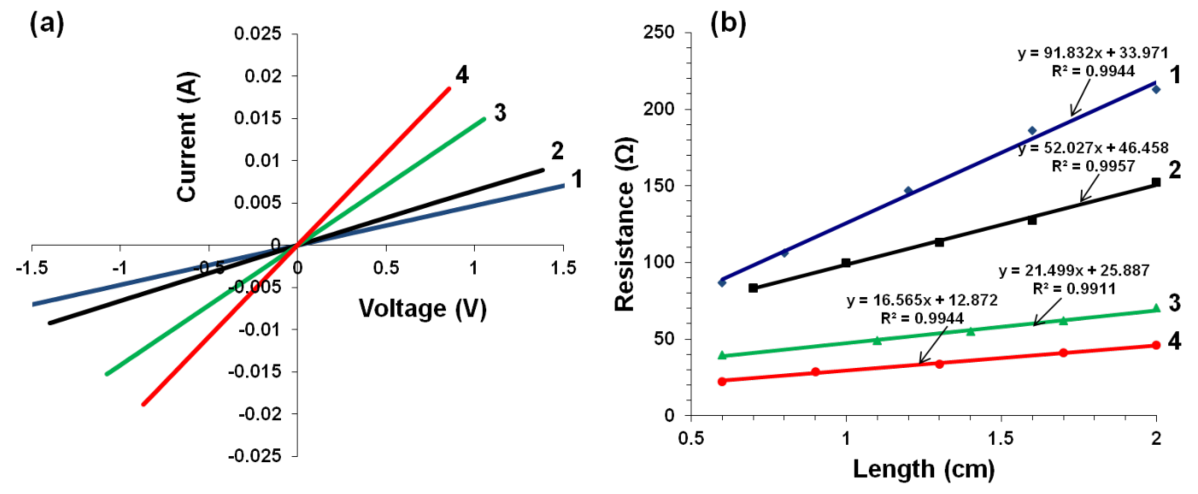

Figure 5: (a) *I–V* characteristics for KC–CNT (channel length 2 cm) and (b) resistance as a function of length for KC–CNT composite films prepared by evaporative casting and vacuum filtration of KC–CNT dispersions. Numbers 1 and 2 are KC–MWNT and KC–SWNT composite films, respectively, prepared by evaporative cast method. Numbers 3 and 4 are KC–MWNT and KC–SWNT composite films, respectively, prepared by the vacuum-filtration method. The straight lines in (b) are fits to Equation 3.

Table 3: Effect of preparation method and addition of glycerin (G) on the conductivity (σ) of KC–CNT films prepared by evaporative casting (E1–4) and vacuum filtration (B1–4) methods. CNT mass (M_f) and volume (V_f) fractions values are calculated by using Equation 4 and Equation 5, respectively. The naming of the dispersions indicates the concentrations of biopolymer, CNTs and glycerin, i.e., “KC05–MW01–G025” corresponds to dispersion with KC, MWNT and G concentrations of 0.5% w/v, 0.1% w/v and 0.25% w/v, respectively.

Film	Dispersion	θ	M_f	V_f	σ (S/cm)
E1	KC05–MW01	64.5 ± 1.1	0.17	0.10	8.6 ± 1.6
E2	KC05–MW01–G025	56.0 ± 1.1	0.12	0.071	5.0 ± 0.9
E3	KC05–SW01	62.7 ± 1.1	0.17	0.13	7.4 ± 0.9
E4	KC05–SW01–G025	50.9 ± 1.4	0.12	0.099	2.9 ± 0.5
B1	KC015–MW003	76.9 ± 0.8	—	—	16.4 ± 1.6
B2	KC015–MW003–G0075	72.4 ± 0.8	—	—	14.5 ± 1.7
B3	KC015–SW003	79.5 ± 2.0	—	—	25.4 ± 1.6
B4	KC015–SW003–G0075	73.0 ± 0.8	—	—	17.9 ± 1.9

mass fraction, but rather the volume fraction is more suitable. The CNT mass (M_f) and volume (V_f) fractions of films prepared by evaporative casting were obtained as follows:

$$M_f = \frac{m_{CNT}}{m_{total}}, \quad (4)$$

$$V_f = (m_{CNT}/\rho_{CNT})/(m_{KC}/\rho_{KC} + m_G/\rho_G + m_{CNT}/\rho_{CNT}), \quad (5)$$

where m_{CNT}, m_{KC}, m_G, m_{total}, ρ_{CNT}, ρ_{KC}, and ρ_G, are the mass of CNT, KC, and G, their total mass, and the densities of CNT, KC and G, respectively. The density value of KC was determined experimentally (1.22 ± 0.06 g/cm^3) and the well-known density values of G (1.26 g/cm^3) and the CNTs were used to calculate the CNT volume fraction. It was found that evaporation-cast MWNT films exhibited higher conductivity values compared to SWNT films at a similar volume fraction, $V_f \sim 0.10$. The conductivity of SWNT films with a higher volume fraction ($V_f = 0.13$) was still lower than that of a MWNT film with $V_f = 0.10$. These observations are in agreement with our previous observations for biopolymer composite materials [8].

It was not possible to calculate the CNT mass or volume fractions for buckypapers, as it is unknown what was lost during the filtration process. In our previous work, we showed that the contact angle increases linearly with CNT mass and volume fraction [8]. The contact angle of all buckypaper materials is higher than those of evaporation-cast films (Table 3). This could suggest that the CNT mass/volume fraction in the buckypapers is higher than those of the evaporation-cast samples. This is supported by the difference in the surface morphology as observed in SEM images (Figure 6), i.e., the biopolymer coverage of the CNTs is more extensive for evaporation-cast films than for buckypapers. The lower degree of coverage can be attributed to the partial removal of KC and CNTs during the vacuum filtration process. These observations are supported by the difference in conductivity between casted (7.4 S/cm) and buckypaper (25.4 S/cm) SWNT composite films, with similar results for MWNT composite films. Hence, it is clear that the partial removal of KC results in an increase in the conductivity. The conductivity values of KC–SWNT buckypapers (25.4 ± 1.6 S/cm), were higher compared to those of the KC–MWNT buckypapers (16.4 ± 1.6 S/cm).

Incorporation of the hydrophilic plasticizer glycerin in the composite films reduced their conductivity and contact angle values. For example, the conductivity of a KC–SWNT film prepared by the evaporative-casting method decreased from

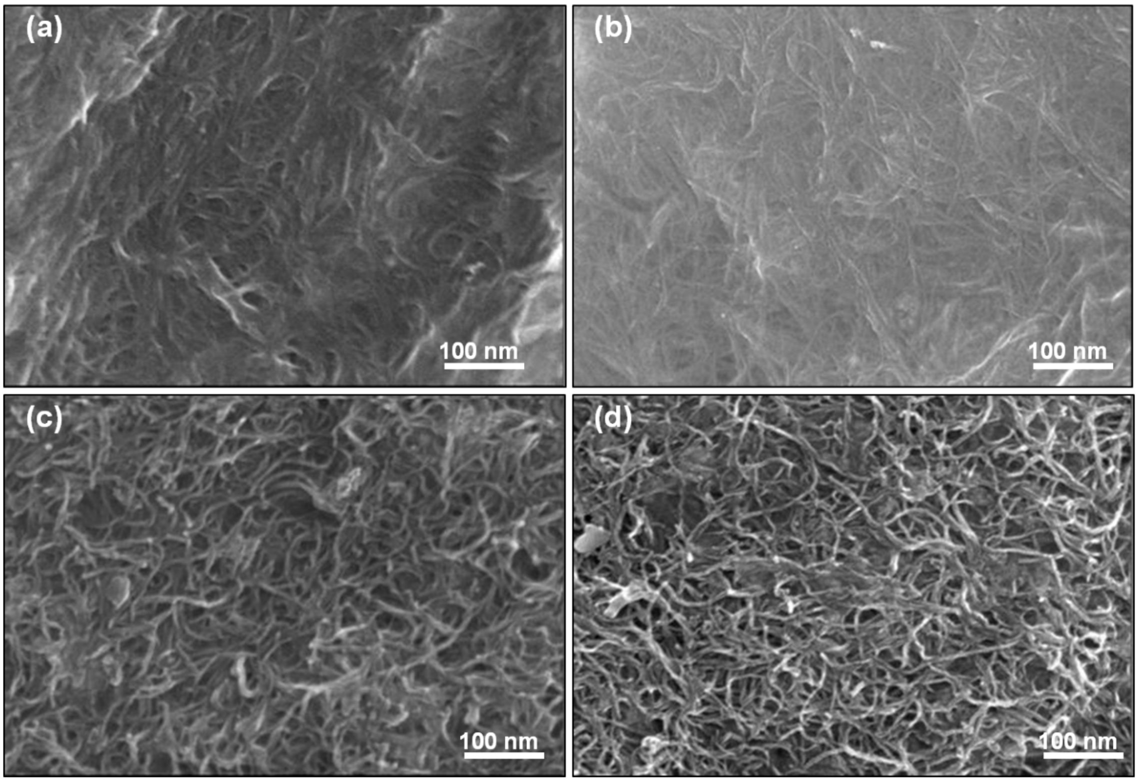

Figure 6: SEM image of (a) KC–CNT and (b) KC–CNT–G composite films prepared by the evaporative-casting method. (c) KC–CNT and (d) KC–CNT–G composite films prepared by the vacuum-filtration method. Contact angle values for (a–d) are 64°, 56°, 77° and 72°, respectively.

7.4 S/cm to 2.9 S/cm through the addition of glycerin. This lowering of the conductivity suggests that glycerin may affect the number of conducting pathways or junctions in the nanotube network.

Mechanical properties of films

The mechanical characteristics of the free-standing films prepared by evaporative casting and vacuum filtration of KC–CNT dispersions are shown in Figure 7. Sonication of the KC solution prior to film formation reduced the mechanical characteristics of these films. The sonication-induced reduction in the molecular weight resulted in films with reduced values of tensile strength (*TS* = 20 MPa), strain-at-break (γ = 2%) and Young’s modulus (*E* = 1165 MPa) (Table 4).

Table 4: Summary of the mechanical properties of composite films prepared by evaporative casting (E1–4) and vacuum filtration (B1–4). Young’s modulus (*E*), tensile strength (*TS*) and strain-at-break (γ). E1–4 and B1–4 refer to composite films listed in Table 3.

Film	*E* (MPa)	*TS* (MPa)	γ (%)
E1	1414 ± 43	32 ± 4	5.1 ± 0.7
E2	1031 ± 40	21 ± 2	7.1 ± 0.8
E3	1640 ± 45	27 ± 3	3.3 ± 0.5
E4	434 ± 29	18 ± 2	4.8 ± 0.6
B1	2184 ± 77	36 ± 3	2.5 ± 0.6
B2	1142 ± 61	32 ± 3	4.0 ± 1.0
B3	2848 ± 81	44 ± 4	2.3 ± 0.8
B4	1228 ± 49	39 ± 3	4.5 ± 1.0

The addition of CNTs resulted in increases in the *TS*, γ and *E* values for both MWNTs and SWNTs compared to the corresponding values for the sonicated KC film (Table 4). This can be attributed to the mechanical reinforcement effect of incorporating CNTs into the polymer matrix [32,50]. Films produced by the evaporative-casting method exhibited higher *E* and *TS* values compared to films produced by vacuum filtration. In contrast, films prepared by the evaporative-casting method exhibit higher strain-at-break values than do films produced by vacuum filtration. Hence, it is clear that films produced by vacuum filtration are more robust and less ductile compared to films prepared by the evaporative-casting method.

Incorporation of a plasticizer (glycerin) resulted in a reduction of the *E* and *TS* values but improved ductility. For example, the γ value for KC–MWNTs films with glycerin prepared by the evaporative-cast method is 7.1% compared to 5.1% for the same film without glycerin. This suggests that glycerin is a good material for improving the mechanical handleability of these CNT composite films.

Sensing properties of films

The sensitivity (*S*) of films against humidified air, and H_2 and CH_4 gases was investigated by monitoring the resistance as a function of time [51]:

$$S(\%) = \left(\frac{\left|R_g - R_a\right|}{R_a}\right) \times 100\%, \qquad (6)$$

where R_a and R_g represent the resistance of the film before and during exposure to the target gas (humidified air, H_2 and CH_4), respectively. The sensitivity of the films to humidity was investigated over a relative humidity change from 40% to 90%. All films responded to the change in humidity, but it was not possible to detect any response after exposure to H_2 and CH_4 gases at 25 °C (Figure 8). The KC–MWNT films displayed higher sensitivity to water vapour compared to the corres-

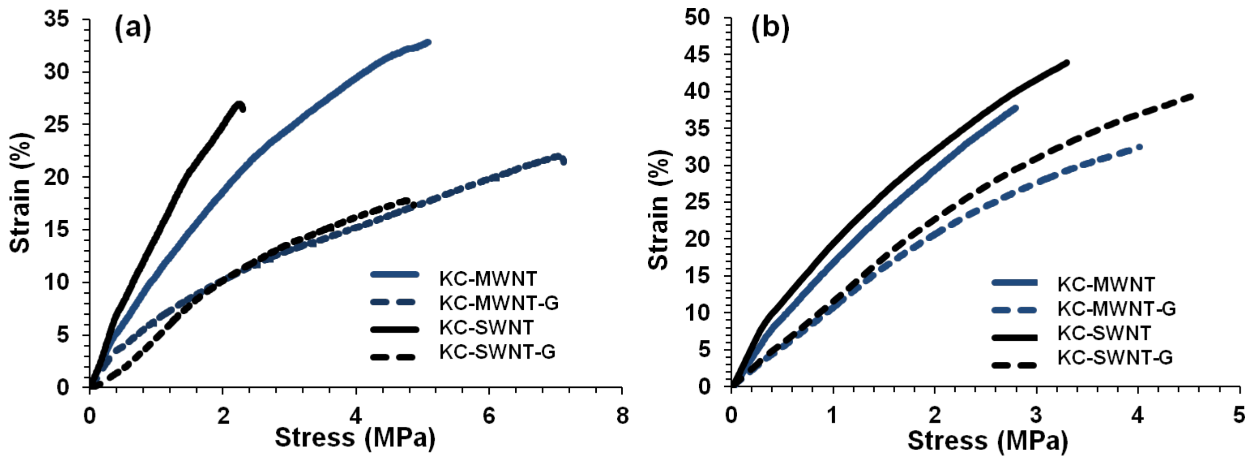

Figure 7: Stress–strain curves for films with and without glycerin prepared by (a) evaporative casting and (b) vacuum filtration methods.

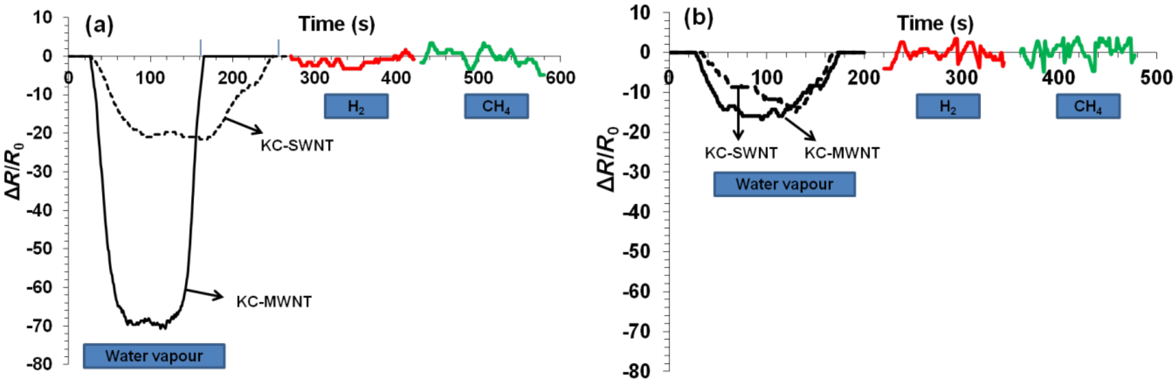

Figure 8: Response of KC–MWNT and KC–SWNT composite films to humidity change, H_2 and CH_4 gases (100 ppm in air) at operating temperature of 25 °C. Films prepared by (a) evaporative casting and (b) vacuum filtration.

ponding KC–SWNT films. For example, the sensitivity of MWNT films was $S = 70 \pm 10\%$ compared to $S = 25 \pm 5\%$ for SWNT films. However, the response/recovery times were faster for MWNT films (50 s) compared to SWNT films (70 s). The sensitivity was significantly reduced upon incorporation of glycerin, e.g., from $S = 70 \pm 10\%$ to $S = 20 \pm 5\%$ for MWNT composite films. Buckypaper films displayed lower sensitivity values of ~17% (MWNT) and ~15% (SWNT), respectively. It is likely that the observed differences in sensitivity can be attributed to the processing methods, i.e., the vacuum filtration process results in partial removal of KC, as discussed above. It is not clear at present why MWNT films prepared by evaporative casting are about three times more sensitive compared to SWNT films. Further research is necessary to fully understand this.

Conclusion

In this work, rheological analysis was used to determine the appropriate concentration (0.5% w/v) for dispersing SWNTs and MWNTs by using the biopolymer KC. It was shown that MWNTs required less sonication compared to SWNTs, i.e., a lower amount of energy input. Rheological analysis revealed that an increasing amount of sonolysis reduced the flow characteristics (viscosity) of KC solutions, while addition of CNTs increased viscosity.

KC–MWNT films prepared by an evaporative-casting process displayed higher conductivity compared to KC–SWNT films. As expected, the conductivity of all buckypaper films was higher than films prepared by evaporative casting. It was observed that the incorporation of CNTs in the polymer matrix resulted in an increase in the values of the mechanical properties. The addition of a plasticizer (glycerin) improved the mechanical handleability, but at the cost of electrical conductivity. Buckypaper films displayed superior electrical and mechanical characteristics (bar ductility) over evaporation-cast films, but they were less sensitive to changes in the humidity. MWNT films exhibited sensitivity to humidity as high as of 70%, easily outperforming SWNT films. This work contributes toward the development of conducting biopolymer composite materials.

Experimental

Materials

The biopolymer iota-carrageenan (KC, molecular weight range 350,000–800,000 g/mol, Genuvisco type CI-102, lot # SKS2500) was donated by CP Kelco (USA). Multiwalled carbon nanotubes (MWNTs) produced by catalytic chemical vapour deposition were obtained from Nanocyl S.A. (Belgium, lot # 090901). Single-walled carbon nanotubes (SWNTs), produced by high-pressure decomposition of carbon monoxide (HiPCO process), were purchased from Unidym Inc. (USA, lot # P0348). Glycerin was obtained from Sigma Aldrich (USA, lot # 033K0097). Methanol (CH_3OH, lot # 318-2.5L GL) was purchased from Ajax Finechem (Australia). Hydrophobic polytetrafluoroethylene (PTFE, pore size of 5 μm) filtration membranes were purchased from Micro Filtration Systems (USA). Milli-Q water was used in all experiments and prepared by using a Millipore filtration system (resistivity of 18.2 MΩ cm).

Preparation of solution and dispersion

Solutions of KC were prepared by adding appropriate amounts of KC to 15 mL of Milli-Q water under stirring for 3 h at ~70 °C (Figure 9a). Homogenous KC–CNT dispersions (CNT concentration = 0.1% w/v, Figure 9a) were prepared by using a digital sonicator horn (Branson 450, Ultrasonics Corp.) with a probe diameter of 10 mm, in pulse mode (0.5 s on/off) and a power output of 12 W. During sonication the sample vial was

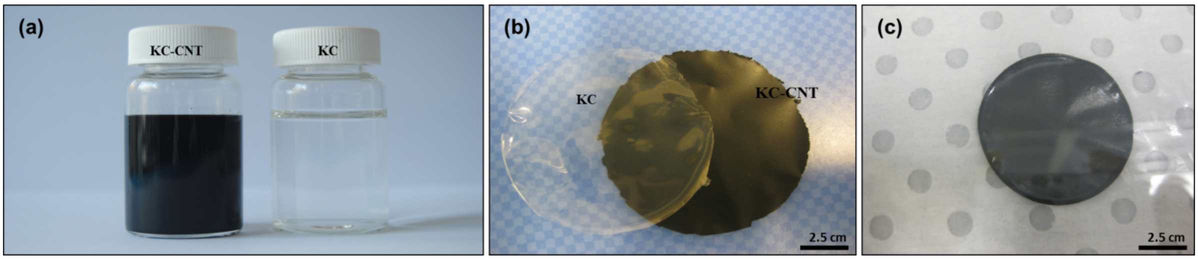

Figure 9: Photographs of (a) KC solution and KC–CNT dispersion, (b) films prepared by evaporative casting and (c) film prepared by vacuum-filtration method.

placed inside a water bath to keep the dispersion temperature constant. Glycerin (G) was added to KC–CNT dispersions at a concentration of 0.25% w/v.

Preparation of films by evaporative-casting method

Free-standing films were prepared by evaporative casting of KC solution and KC–CNT dispersions into the base of cylindrical plastic containers (polystyrene, diameter = 55 mm), which were then dried under controlled conditions (35 °C, relative humidity, RH = 45%) in a temperature–humidity chamber (Thermoline Scientific) for 24 h. The resulting films were peeled off the substrate to yield uniform free-standing films (Figure 9b).

Preparation of films by vacuum-filtration method

KC–CNT dispersions were processed into buckypapers by using a vacuum-filtration method. Prior to the filtration the KC–CNT dispersion was combined with 35 mL Milli-Q water and inverted to ensure complete mixing. The dispersions (50 mL) were drawn through a PTFE membrane filter (pore size = 5 μm) on a filtration unit (Millipore, diameter = 37 mm) by using a vacuum pump (Vacuubrand CVC2). Once all of the dispersion had been filtered, the films were washed with 50 mL of Milli-Q water followed by 5 mL of methanol (99.8%) and placed between absorbent paper sheets to dry under controlled conditions (21 °C, RH = 45%) for 24 h. The films were then peeled off from the filtration membrane (Figure 9c).

Characterization

UV–visible–NIR absorption spectra of KC solutions and KC–CNTs dispersions were obtained with a UV–vis–NIR spectrophotometer (Cary 500) by using a quartz cuvette (path length = 5 mm). All solutions and dispersions were diluted by a factor of 10. Dispersions were imaged by using an optical microscope (LEICA Z16 APO) fitted with a digital camera (LEICA DFC280) and Leica Application Suite (version 3.1.0 R1) software. Rheological testing was conducted by using a parallel-plate rheometer (Anton Paar–Physica MCR 301) with a 50 mm diameter probe head (cone angle 1°) at 21 °C. KC–CNT dispersions and KC solutions were analysed by using flow curves (viscosity and shear stress versus shear rate). The dynamic modulus was measured by using oscillatory strain sweeps at constant frequency.

For conductivity measurements, films were cut into strips 0.5 cm in width and 3 cm in length and contacted with copper electrodes (3M). Current (*I*)–voltage (*V*) characteristics were obtained by measuring the current using a digital multimeter (Agilent 34410A) under a cycling potential applied by a waveform generator (Agilent 33220A). *I*–*V* measurements were conducted under controlled ambient conditions (21 °C, RH = 45%) as a function of film length, by repeatedly cutting the end of the strip, contacting with the electrodes and remeasuring the *I*–*V* characteristics. Film thickness was determined with a Mitutoyo IP65 digital micrometer.

The mechanical properties of all films were obtained by using a dynamic mechanical analyser (DMA) Q800 (TA instruments). Measurements were carried out under ambient conditions (21 °C, RH = 45%) on rectangular strips (length = 10 mm) at a cross-head speed of 0.1 mm/min. Tensile strength, strain-at-break and Young's modulus were determined from the maximum stress, the strain at failure, and the slope of the initial linear part of the stress–strain curve, respectively.

Scanning electron microscope (SEM) images were acquired by using a JEOL JSM-7500FA. Samples were prepared by mounting small pieces of films onto a brass stub (11×5 mm^2) with double-sided, conductive carbon tape (Proscitech, Australia).

Contact-angle measurements were carried out by using the sessile drop method on a goniometer (Data Physics SCA20), which was fitted with a digital camera. The contact angles of 1 μL Milli-Q water droplets on the surface of the samples were calculated after 30 s by using the accompanying Data Physics software (version SCA20.1). The mean contact angle was calculated based on measurements performed on at least five water droplets.

The sensing properties of the films were investigated with a custom-built system [52]. The films are connected in series to a known resister (909 Ω) and a battery (4.91 V) to form a voltage–current–resistor (*V–I–R*) electrical circuit as a prototype sensor. The sensitivity of the sensors was characterised by using measurements of the voltage drop across the known resistor and film under different environmental conditions, i.e., as a function of temperature and humidity, and by exposure to different gases (H_2 and CH_4) at a concentration of 100 ppm in air. For all measurements, air was used as the carrier gas. The chamber volume (1000 mL) ensures that the change of gas concentration was instantaneous, which is a prerequisite condition for the accurate measurements of response and recovery time of the sensor.

Acknowledgments

This work was funded by King Saud University (A. Aldalbahi), University of Wollongong, Australian Research Council (ARC) Centre of Excellence Program, ARC Future Fellowship (M. in het Panhuis) and NSF EPSCoR program (P. Feng). We thank M. Collins, R. Clark and P. Jackson (all CP Kelco) for the provision of materials and T. Romeo (University of Wollongong) for assistance with SEM measurements.

References

1. Jorio, A.; Dresselhaus, G.; Dresselhaus, M. S., Eds. *Carbon Nanotubes: Advanced Topics in the Synthesis, Structure, Properties and Applications;* Topics in Applied Physics, Vol. 111; Springer-Verlag: Berlin, 2008. doi:10.1007/978-3-540-72865-8
2. in het Panhuis, M. *J. Mater. Chem.* **2006,** *16,* 3598–3605. doi:10.1039/B606959B
3. Dresselhaus, M. S.; Dresselhaus, G.; Eklund, P. C. *Science of Fullerenes and Carbon Nanotubes;* Academic Press: San Diego, 1996.
4. Saito, R.; Dresselhaus, G.; Dresselhaus, M. S. *Physical Properties of Carbon Nanotubes;* Imperial College Press: London, 1998. doi:10.1142/9781860943799
5. Hamon, M. A.; Chen, J.; Hu, H.; Chen, Y.; Itkis, M. E.; Rao, A. M.; Eklund, P. C.; Haddon, R. C. *Adv. Mater.* **1999,** *11,* 834–840. doi:10.1002/(SICI)1521-4095(199907)11:10<834::AID-ADMA834>3.0.CO;2-R
6. Nuriel, S.; Liu, L.; Barber, A. H.; Wagner, H. D. *Chem. Phys. Lett.* **2005,** *404,* 263–266. doi:10.1016/j.cplett.2005.01.072
7. Sainz, R.; Small, W. R.; Young, N. A.; Vallés, C.; Benito, A. M.; Maser, W. K.; in het Panhuis, M. *Macromolecules* **2006,** *39,* 7324–7332. doi:10.1021/ma061587q
8. Aldalbahi, A.; in het Panhuis, M. *Carbon* **2012,** *50,* 1197–1208. doi:10.1016/j.carbon.2011.10.034
9. Boge, J.; Sweetman, L. J.; in het Panhuis, M.; Ralph, S. F. *J. Mater. Chem.* **2009,** *19,* 9131–9140. doi:10.1039/B914824H
10. Ferris, C. F.; in het Panhuis, M. *Soft Matter* **2009,** *5,* 3430–3437. doi:10.1039/B909795C
11. Granero, A. J.; Razal, J. M.; Wallace, G. G.; in het Panhuis, M. *Adv. Funct. Mater.* **2008,** *18,* 3759–3764. doi:10.1002/adfm.200890097
12. Hrapovic, S.; Male, K. B.; Liu, Y.; Luong, J. H. T. *Anal. Lett.* **2008,** *41,* 278–288. doi:10.1080/00032710701792737
13. Moulton, S. E.; Minett, A. I.; Murphy, R.; Ryan, K. P.; McCarthy, D.; Coleman, J. N.; Blau, W. J.; Wallace, G. G. *Carbon* **2005,** *43,* 1879–1884. doi:10.1016/j.carbon.2005.02.036
14. Razal, J. M.; Gilmore, K. J.; Wallace, G. G. *Adv. Funct. Mater.* **2008,** *18,* 61–66. doi:10.1002/adfm.200700822
15. Vaisman, L.; Wagner, H. D.; Marom, G. *Adv. Colloid Interface Sci.* **2006,** *128–130,* 37–46. doi:10.1016/j.cis.2006.11.007
16. Wang, J.; Musameh, M.; Lin, Y. *J. Am. Chem. Soc.* **2003,** *125,* 2408–2409. doi:10.1021/ja028951v
17. Bystrzejewski, M.; Huczko, A.; Lange, H.; Gemming, T.; Büchner, B.; Rümmeli, M. H. *J. Colloid Interface Sci.* **2010,** *345,* 138–142. doi:10.1016/j.jcis.2010.01.081
18. Duro, R.; Souto, C.; Gómez-Amoza, J. L.; Martínez-Pacheco, R.; Concheiro, A. *Drug Dev. Ind. Pharm.* **1999,** *25,* 817–829. doi:10.1081/DDC-100102244
19. Grossiord, N.; Regev, O.; Loos, J.; Meuldijk, J.; Koning, C. E. *Anal. Chem.* **2005,** *77,* 5135–5139. doi:10.1021/ac050358j
20. Islam, M. F.; Rojas, E.; Bergey, D. M.; Johnson, A. T.; Yodh, A. G. *Nano Lett.* **2003,** *3,* 269–273. doi:10.1021/nl025924u
21. Lin, Y.; Taylor, S.; Li, H.; Shiral Fernando, K. A.; Qu, L.; Wang, W.; Gu, L.; Zhou, B.; Sun, Y.-P. *J. Mater. Chem.* **2004,** *14,* 527–541. doi:10.1039/B314481J
22. O'Connell, M. J.; Bachilo, S. M.; Huffman, C. B.; Moore, V. C.; Strano, M. S.; Haroz, E. H.; Rialon, K. L.; Boul, P. J.; Noon, W. H.; Kittrell, C.; Ma, J.; Hauge, R. H.; Weisman, R. B.; Smalley, R. E. *Science* **2002,** *297,* 593–596. doi:10.1126/science.1072631
23. O'Connell, M. J.; Boul, P.; Ericson, L. M.; Huffman, C.; Wang, Y.; Haroz, E.; Kuper, C.; Tour, J.; Ausman, K. D.; Smalley, R. E. *Chem. Phys. Lett.* **2001,** *342,* 265–271. doi:10.1016/S0009-2614(01)00490-0
24. Star, A.; Stoddart, J. F.; Steuerman, D.; Diehl, M.; Boukai, A.; Wong, E. W.; Yang, X.; Chung, S.-W.; Choi, H.; Heath, J. R. *Angew. Chem., Int. Ed.* **2001,** *40,* 1721–1725. doi:10.1002/1521-3773(20010504)40:9<1721::AID-ANIE17210>3.0.CO;2-F
25. Bandyopadhyaya, R.; Nativ-Roth, E.; Regev, O.; Yerushalmi-Rozen, R. *Nano Lett.* **2002,** *2,* 25–28. doi:10.1021/nl010065f
26. Polaczek, E.; Stobiński, L.; Mazurkiewicz, J.; Tomasik, P.; Kołoczek, H.; Lin, H.-M. *Polimery* **2007,** *52,* 34–38.
27. Ferris, C. J.; in het Panhuis, M. *Soft Matter* **2009,** *5,* 1466–1473. doi:10.1039/B818411A
28. Lu, L.; Chen, W. *ACS Nano* **2010,** *4,* 1042–1048. doi:10.1021/nn901326m
29. Songmee, N.; Singjai, P.; in het Panhuis, M. *Nanoscale* **2010,** *2,* 1740–1745. doi:10.1039/C0NR00259C
30. in het Panhuis, M.; Heurtematte, A.; Small, W. R.; Paunov, V. N. *Soft Matter* **2007,** *3,* 840–843. doi:10.1039/B704368F
31. Bauhofer, W.; Kovacs, J. Z. *Compos. Sci. Technol.* **2009,** *69,* 1486–1498. doi:10.1016/j.compscitech.2008.06.018
32. Coleman, J. N.; Khan, U.; Gun'ko, Y. K. *Adv. Mater.* **2006,** *18,* 689–706. doi:10.1002/adma.200501851
33. Kukovecz, Á.; Smajda, R.; Kónya, Z.; Kiricsi, I. *Carbon* **2007,** *45,* 1696–1698. doi:10.1016/j.carbon.2007.04.033
34. Whitby, R. L. D.; Fukuda, T.; Maekawa, T.; James, S. L.; Mikhalovsky, S. V. *Carbon* **2008,** *46,* 949–956. doi:10.1016/j.carbon.2008.02.028

35. Claye, A. S.; Fischer, J. E.; Huffman, C. B.; Rinzler, A. G.; Smalley, R. E. *J. Electrochem. Soc.* **2000,** *147,* 2845–2852. doi:10.1149/1.1393615
36. Liu, T.; Sreekumar, T. V.; Kumar, S.; Hauge, R. H.; Smalley, R. E. *Carbon* **2003,** *41,* 2440–2442. doi:10.1016/S0008-6223(03)00245-8
37. Prokudina, N. A.; Shishchenko, E. R.; Joo, O.-S.; Hyung, K.-H.; Han, S.-H. *Carbon* **2005,** *43,* 1815–1819. doi:10.1016/j.carbon.2005.02.012
38. Rein, M. D.; Breuer, O.; Wagner, H. D. *Compos. Sci. Technol.* **2011,** *71,* 373–381. doi:10.1016/j.compscitech.2010.12.008
39. Campo, V. L.; Kawano, D. F.; da Silva, D. B., Jr.; Carvalho, I. *Carbohydr. Polym.* **2009,** *77,* 167–180. doi:10.1016/j.carbpol.2009.01.020
40. van de Velde, F.; Lourenço, N. D.; Pinheiro, H. M.; Bakker, M. *Adv. Synth. Catal.* **2002,** *344,* 815–835. doi:10.1002/1615-4169(200209)344:8<815::AID-ADSC815>3.0.CO;2-H
41. Buck, C. B.; Thompson, C. D.; Roberts, J. N.; Müller, M.; Lowy, D. R.; Schiller, J. T. *PLoS Pathog.* **2006,** *2,* e69. doi:10.1371/journal.ppat.0020069
42. Grenha, A.; Gomes, M. E.; Rodrigues, M.; Santo, V. E.; Mano, J. F.; Neves, N. M.; Reis, R. L. *J. Biomed. Mater. Res., Part A* **2010,** *92A,* 1265–1272. doi:10.1002/jbm.a.32466
43. McHugh, T. H.; Krochta, J. M. *J. Agric. Food Chem.* **1994,** *42,* 841–845. doi:10.1021/jf00040a001
44. Barnes, H.; Hutton, J.; Walers, K. *An Introduction to Rheology;* Elsevier: Amsterdam, 1989.
45. Clasen, C.; Kulicke, W.-M. *Prog. Polym. Sci.* **2001,** *26,* 1838–1919. doi:10.1016/S0079-6700(01)00024-7
46. Iglauer, S.; Wu, Y.; Shuler, P.; Tang, Y.; Goddard, W. A., III. *J. Petrol. Sci. Eng.* **2011,** *75,* 304–311. doi:10.1016/j.petrol.2010.11.025
47. Elias, H. *An Introduction to Polymer Science;* VCH: Weinheim, 1997.
48. Benedict, B.; Pehrsson, P. E.; Zhao, W. *J. Phys. Chem. B* **2005,** *109,* 7778–7780. doi:10.1021/jp0406161
49. Tsaih, M. L.; Chen, R. H. *J. Appl. Polym. Sci.* **2003,** *90,* 3526–3531. doi:10.1002/app.13027
50. Coleman, J. N.; Cadek, M.; Ryan, K. P.; Fonseca, A.; Nagy, J. B.; Blau, W. J.; Ferreira, M. S. *Polymer* **2006,** *47,* 8556–8561. doi:10.1016/j.polymer.2006.10.014
51. Peng, X. Y.; Sajjad, M.; Chu, J.; Yang, B. Q.; Feng, P. X. *Appl. Surf. Sci.* **2011,** *257,* 4795–4800. doi:10.1016/j.apsusc.2010.12.041
52. Feng, P. X.; Zhang, H. X.; Peng, X. Y.; Sajjad, M.; Chu, J. *Rev. Sci. Instrum.* **2011,** *82,* 043303. doi:10.1063/1.3581207

License and Terms

The definitive version of this article is the electronic one which can be found at:
doi:10.3762/bjnano.3.48

Beilstein Journal
of Nanotechnology

FTIR nanobiosensors for *Escherichia coli* detection

Stefania Mura*[1,2,3,§], Gianfranco Greppi[1,4], Maria Laura Marongiu[4],
Pier Paolo Roggero[1], Sandeep P. Ravindranath[2], Lisa J. Mauer[5],
Nicoletta Schibeci[3], Francesco Perria[6], Massimo Piccinini[7], Plinio Innocenzi[8]
and Joseph Irudayaraj[2]

Full Research Paper

Open Access

Address:
[1]Nucleo Ricerca Desertificazione, Università degli Studi di Sassari, Viale Italia 57, 07100 Sassari, Italy, [2]Department of Agricultural and Biological Engineering and Bindley Bioscience Center, Purdue University, 225 S. University Street, West Lafayette, 47907, Indiana, [3]Lea Nanotech s.r.l. S.P. 55 Porto Conte/Capo Caccia, km 8.400 località Tramariglio, 07041 Alghero (SS), Italy, [4]Dipartimento di scienze zootecniche, Università degli Studi di Sassari, Via Enrico De Nicola 9, 07100 Sassari, Italy, [5]Department of Food Science, Purdue University, 745 Agriculture Mall Drive, West Lafayette, 47907, Indiana, [6]Biodiversity s.r.l. S.P. 55 Porto Conte/Capo Caccia, km 8.400 località Tramariglio, 07041 Alghero (SS), Italy, [7]Porto conte ricerche, SP 55 Porto Conte/Capo Caccia, km 8.400 località Tramariglio, 07041 Alghero (SS), Italy and [8]Materials Science and Nanotechnology Laboratory, D.A.P., CR-INSTM, Università di Sassari, Palazzo Pou Salit, Piazza Duomo 6, 07041 Alghero (SS), Italy

Email:
Stefania Mura* - mura.stefania@gmail.com

* Corresponding author
§ Tel: +39 079998441

Keywords:
biosensors; *E. coli*; FTIR spectroscopy; foodborne pathogens; nanomaterials

Beilstein J. Nanotechnol. **2012,** *3,* 485–492.
doi:10.3762/bjnano.3.55

Received: 06 March 2012
Accepted: 13 June 2012
Published: 03 July 2012

This article is part of the Thematic Series "Nanostructures for sensors, electronics, energy and environment".

Associate Editor: N. Motta

Abstract

Infections due to enterohaemorrhagic *E. coli* (*Escherichia coli*) have a low incidence but can have severe and sometimes fatal health consequences, and thus represent some of the most serious diseases due to the contamination of water and food. New, fast and simple devices that monitor these pathogens are necessary to improve the safety of our food supply chain. In this work we report on mesoporous titania thin-film substrates as sensors to detect *E. coli* O157:H7. Titania films treated with APTES ((3-aminopropyl)triethoxysilane) and GA (glutaraldehyde) were functionalized with specific antibodies and the absorption properties monitored. The film-based biosensors showed a detection limit for *E. coli* of 1×10^2 CFU/mL, constituting a simple and selective method for the effective screening of water samples.

Introduction

Foodborne illness is primarily caused by pathogenic microorganisms among which *Campylobacter, Salmonella, Listeria monocytogenes*, and *Escherichia coli* O157: H7 are responsible for the majority of foodborne outbreaks [1,2], and most of the recalls of food products have implicated these pathogens [3]. In particular *E. coli* is a typical inhabitant of the human intestinal tract; however, the strain *E. coli* O157:H7, one of the most dangerous foodborne pathogens [4], causes diseases that may lead to death [5]. Sensors to detect these pathogens, especially in ground beef and raw milk [6], are critical.

The conventional methods for the detection and identification of pathogens [7,8] are mostly based on (i) culture and colony counting methods (which involve counting of bacteria) [9]; (ii) immunology-based methods (which involve antigen–antibody interactions) [10]; and (iii) the polymerase chain reaction (PCR) method (which involves DNA analysis) [11,12]. While these methods are sensitive and can recognize pathogens, the type of organism and the number of colonies in a qualitative and quantitative manner, they are not efficient because of the enrichment step necessary to detect pathogens in low numbers, to comply with the safety regulations of the food and water supply chain. In addition, these methods are expensive, complicated, time-consuming, and require skilled personnel with expertise in molecular biology.

To overcome these problems, devices that can be used in situ, and that are simple, highly sensitive, inexpensive and rapid are attractive because they can be used for rapid screening of different samples for timely detection of these pathogenic agents. In fact monitoring food quality and safety attributes, by using new detection methods that have the potential to be sensitive and rapid [13], is important to prevent and identify problems related to health and safety. Lately, micro- and nanosystems for bacteria and food sample analysis have been developed as innovative tools for the detection of foodborne pathogens in the food and drink industries [14-21]. In particular, different optical biosensors were created for rapid detection of pathogenic bacteria, using fluorescence or surface plasmon resonance (SPR) because of their sensitivity [22,23].

For fluorescence analysis, antibodies (Ab) are conjugated with fluorescent compounds and used in combination with classical techniques (ELISA, PCR). With these biosensors overnight culture is required, leading to a long time for the analysis, while SPR is a powerful and complex technique, which unfortunately requires specialized staff, and costly and large equipment [24,25]. To overcome these limitations the aim of the present work is to develop a simple new nanodevice capable of detecting pathogens in low concentration and suitable for a fast real-time monitoring, using Fourier transform infrared (FTIR) spectroscopy as an optical transduction method.

Experimental

Chemicals

All commercially available solvents and reagents were used without further purification. Titanium tetrachloride ($TiCl_4$, >98%), anhydrous ethanol (EtOH, >99.9%), bidistilled water, acetone (>99.8%), and toluene (>99.5%), were purchased from Carlo Erba (Italy). Pluronic F-127 (cell culture test), (3-aminopropyl)triethoxysilane (APTES, >98%), glutaraldehyde (GA Grade I, 50% in H_2O, specially purified for use as an electron microscopy fixative or other sophisticated use) were purchased from Sigma Aldrich (Germany). *E. coli* O157:H7 and *E. coli* K12 were obtained from the bacteria collection at Purdue University (Agricultural and Biological Engineering). BHI agar, PCA, and LB were purchased from Teknova (Hollister, CA). Bac-trace affinity purified antibodies goat anti-*E. coli* O157:H7 were purchased from Kirkegaard and Perry Laboratories Inc. (Gaithersburg, MD). Silicon wafers (test grade, p-type boron doped, diameter 4″, thickness 475–575 μm, (100) oriented (one side polished and one side etched) were obtained from Jocam (Italy).

Film preparation

Titania (TiO_2) thin films were prepared by dipping silicon wafers in a solution composed of $TiCl_4$/Pluronic F127/H_2O/EtOH (1:0.005:10:40) under controlled conditions of temperature and RH (relative humidity). Films were deposited with a dip coater, aged at room temperature (RH 50% for 24 h) and, to increase the inorganic polycondensation and stabilize the mesophase, the films were submitted to different firing steps at 60, 120 and 200 °C for 24 h at each temperature in an oven at a heating rate of 10 $°C \cdot min^{-1}$. The final calcination process to remove the organic template of these stabilized coatings was conducted at 350 °C for 3.5 h in air under static conditions at a heating rate of 10 $°C \cdot min^{-1}$. In this way mesoporous titania thin films were obtained and characterized as described in a previous work of our group [26].

Film functionalization

The optimization of the functionalization with amino-groups was obtained by immersing the calcined films in a solution 0.2 M of APTES in toluene for 24 h at 25 °C. The amino grafted films were carefully washed with toluene over several washing cycles and finally dried in air. The following functionalization of TiO_2–APTES films with GA was obtained by immersing the films in GA 50% (v/v) in water for 24 h, washing with water and EtOH and drying at room temperature. Different experiments were realized, providing the immobilization of antibodies directly on titania thin films, on films functionalized with APTES, or on films functionalized with APTES and GA. Antibody solutions were prepared by dissolving 200 µL of anti-*E. coli* O157:H7 in 800 µL phosphate buffered saline (PBS) to achieve a final concentration of 50 µg/mL, after which the films were covered with this solution for 15 h at 4 °C. Finally the films were washed with PBS and water, and dried at room temperature. FTIR spectroscopy measurements were carried out for each step to monitor the chemical functionalization and the linking of antibodies to the films.

Bacteria preparation

E. coli O157:H7 and *E. coli* K12 were cultured on agar plates for 24 h then a single colony of each species was transferred into 10 culture tubes containing 5 mL each of Luria-Bertani medium (LB) and placed in an incubator at 37 °C, under shaking, for 18 h, at 120 rpm. Then the tubes were centrifuged at 3500 rpm for 10 min, to obtain a pellet. Finally LB was removed from the tube and the cells were washed three times with sterile PBS to remove residual medium and resuspended in 3 mL PBS for binding experiments.

Serial dilutions of bacteria were prepared for the detection step. To validate the data, a standard method for the counting of pathogens was also used: the culture and colony counting method. To revitalize the culture of *E. coli*, a single colony was transferred in a test tube containing a nutrient broth and placed in an incubator for 24 h at 37 °C. Then serial dilutions were carried out in sterile saline solution to a dilution of 10^{-7}. Then 1 mL of solutions at a dilution of 10^{-6} and 10^{-7} were plated in a petri plate with plate count agar (PCA) by the inclusion method (in duplicate for each dilution). Finally, after cooling, the four plates were incubated at 37 °C for 24 h and the colonies were counted.

Considering the dilution factor and the mean number of colonies counted in two plates at a dilution of 10^{-6}, the concentration of bacteria in the initial nutrient broth was obtained and estimated to be 1.13×10^8 colony-forming units (CFU)/mL. For DNA analysis a standard method was used to identify the pathogen: real-time PCR. The instrumentation BioRad IQ5 was used for the analysis. After DNA extraction with the boiling method, PCR was carried out with a blank sample, a reference sample and the DNA extracted from 1 mL of nutrient broth; 50 cycles were programmed and an amplification at the 17th cycle could be observed.

Determination of the detection limits of *E. coli* O157:H7

Functionalized titania thin films were incubated with freshly prepared anti-*E. coli* O157:H7 antibodies, and then different films were covered with 1 mL of *E. coli* O157:H7 suspension at concentrations ranging between 10^8 and 10 CFU/mL for 30 min, to allow the binding to take place. Finally these films were washed and dipped for 15 min in PBS solution, washed with PBS and water, dried in air at room temperature and finally analysed by FTIR spectroscopy to determine the sensitivity of the method. Colony micrographs of these films were collected. Some tests with *E. coli* K12 were carried out to monitor the selectivity of the device.

Film characterization

Mesoporous titania thin films were characterized with a Nicolet Nexus FTIR spectrophotometer equipped with a KBr–DTGS detector and a KBr beam splitter. The measurements were carried out in the range of 4000–700 cm^{-1} with 256 scans at 4 cm^{-1} resolution. The detector was cooled with liquid nitrogen for 60 min before data collection and also during the measurements.

The spectra of films deposited on silicon wafers were obtained in transmission mode. The background was recorded by using a silicon substrate. Atomic force microscopy (AFM) measurements were taken on titania films with an Asylum Research 3-D AFM in contact mode. An olympus BX-51 optical microscope with a 100× objective was used to collect microscopic images of films after pathogen immobilization.

Results and Discussion

An optical biosensor was developed for the detection of pathogenic *E. coli* O157:H7, by using FTIR spectroscopy to provide mid-infrared fingerprints of pathogens present in buffer. The spectroscopic fingerprint of pathogens originates from the various functional groups related to proteins, lipids, and carbohydrates, and their mid-infrared (MIR) spectra can be used for the identification and structural characterization of different pathogens and subspecies [27]. MIR spectra are additive and sensitive, and allow the fingerprinting and quantification of the pathogen of interest, transforming the traditional devices into biosensing systems with high sensitivity.

In particular, mesoporous titania thin films synthesized with the sol–gel method, were used to immobilize biomolecules (antibodies and pathogens) thanks to the high surface area due to their nano-organization, visible in a AFM image (Figure 1). This was possible due to a high control of the gelation process on the films and subsequent thermal treatments that avoided the denaturation of biomolecules in environments that have a high alcohol concentration and extreme pH values, hence obtaining ordered and reproducible substrates. With this objective, special attention was paid to the thermal treatments of films to completely remove the inorganic template, EtOH and HCl.

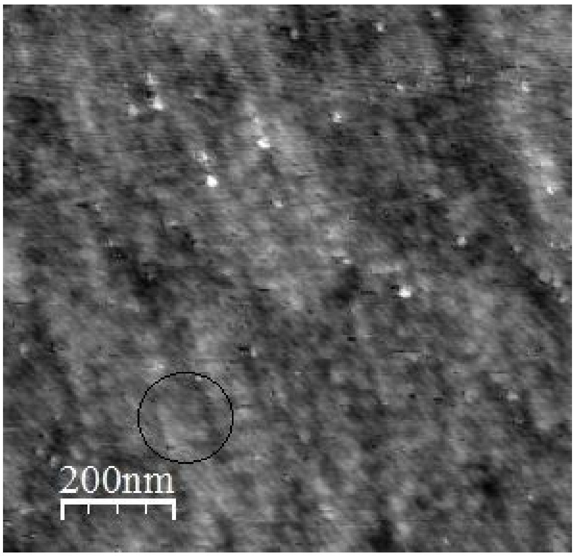

Figure 1: Microscopically ordered structure of a mesoporous titania film observed by AFM analysis.

Mesoporous titania was used as a substrate for the features described above, but also because it has excellent biocompatibility, stability (12 months at RT), and reproducibility, and can interact with biological molecules due to the formation of coordinated linkages between titania films, organic crosslinkers and amino or carboxyl groups of the antibodies or bacteria. In the present work the immobilization of bacteria was studied directly on titania films, on titania films functionalized with APTES and on titania films functionalized with APTES, GA and antibodies (Ab).

Detection of *E. coli* with TiO_2–APTES–GA–anti *E. coli* O157:H7-Ab

The first method used illustrates the detection of *E. coli* O157:H7 through the immobilization of antibodies on titania films functionalized with APTES and GA. In the first step (Figure 2a) titania thin films were functionalized with APTES; in particular the spectra of the films before and after the functionalization process were reported. The peaks due to APTES (inset spectrum) have been attributed to N–H stretching at 3300 cm^{-1}, N–CH_2 stretching around 2800 cm^{-1}, NH_2

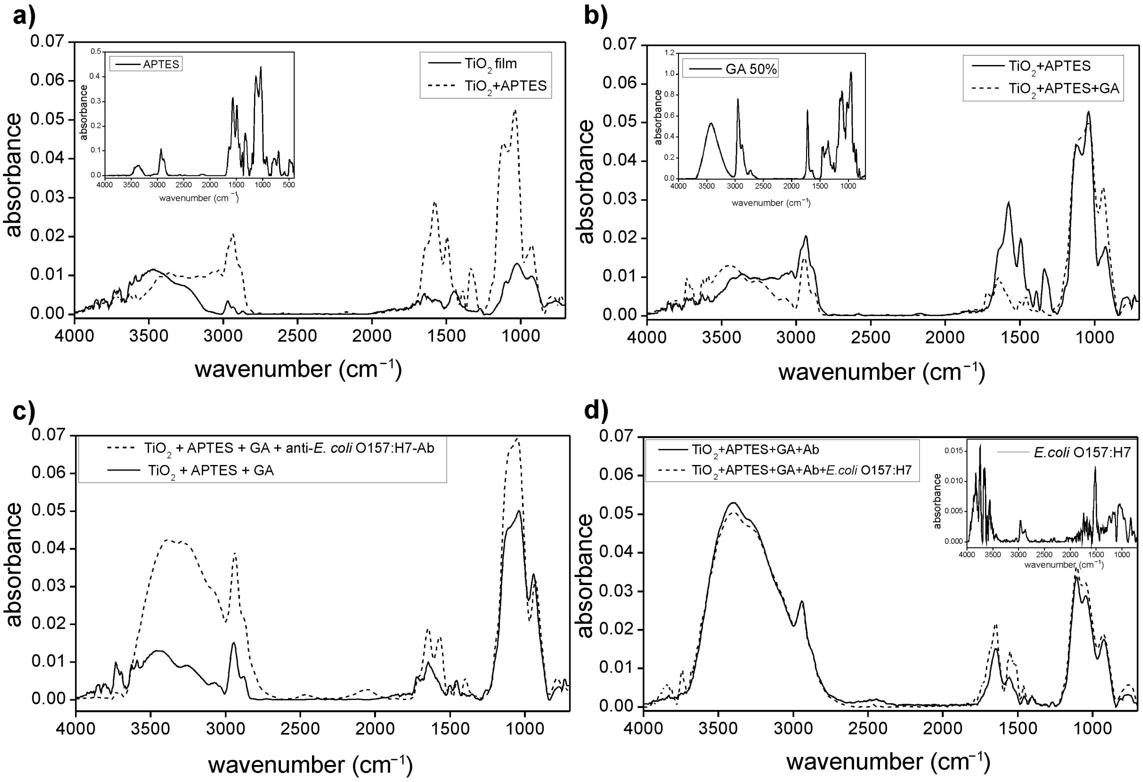

Figure 2: (a) FTIR spectrum of mesoporous titania thin films (solid line) and films functionalized with APTES (dashed line). The reference spectrum of APTES is reported in the inset. (b) FTIR spectrum of titania films functionalized with APTES (solid line) and after the linking of glutaraldehyde (dashed line); the spectrum of glutaraldehyde (GA) was reported in the inset for reference. (c) Spectrum of functionalized titania with APTES and GA (solid line) and after the linking of anti-*E. coli* O157:H7-antibody (dashed line). (d) FTIR spectrum of a titania film functionalized with APTES–GA–Ab (solid line) and after the immobilization of *E. coli* O157:H7 (dashed line); the reference spectrum of *E. coli* O157:H7 is provided in the inset.

scissoring and N–H bending at 1615 cm^{-1}, aliphatic C–N stretching at 1020–1220 cm^{-1}, NH_2 wagging and twisting at 850–750 cm^{-1} and N–H wagging at 715 cm^{-1}.

The second step was based on the reaction between APTES and GA, which was used to crosslink the APTES with antibodies due to the formation of an imine. Here, the terminal amino groups of APTES were changed to aldehydic groups that, in the following step, were covalently coupled with the amino groups of the antibody. The APTES–GA linking is shown in Figure 2b, in which the bands due to the formation of imines in the area between 1900 and 1600 cm^{-1}, and the bands related to the stretching of C–N, C–O, C–C groups in the range 1500–1200 cm^{-1} are visible. The GA spectrum is included as a reference in the inset.

The functionalization process was also visible on the film surface, as reported in Figure 3, due to the change in the colour of films. To complete the sensor fabrication, antibodies against *E. coli* O157:H7 were linked to the substrate as reported in Figure 2c and Figure 4. For the final detection of *E. coli* O157:H7 this chip was immersed in a PBS buffer with *E. coli* O157:H7 (10^8 CFU/mL) for 30 min, washed and analysed.

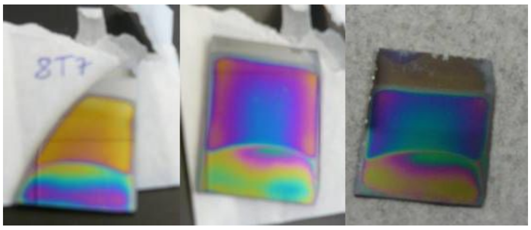

Figure 3: Titania films before functionalization (yellow), after APTES treatment (pink) and after the linking with GA (blue).

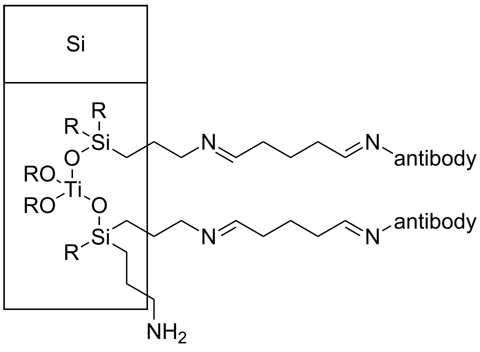

Figure 4: Structure of the chemical linking, TiO_2–APTES–GA–antibody.

The reported spectrum (Figure 2d) shows similar peaks for the film with the pathogen (dotted line) in comparison to films without the pathogen (solid line); however, new peaks appeared in particular in the regions 1300–2000 cm^{-1} (protein peaks of the bacterium), 3700–4000 cm^{-1} and 1200–800 cm^{-1} (signals of nucleic acids of the bacterium), which unfortunately in this region overlapped with the spectrum of the Ab and of the functionalized titania. The peaks in the 1630–1697 cm^{-1} region are due to amide I bands of the proteins in the cell and to their secondary structure. In the region 1402–1457 cm^{-1}, bands due to carbohydrates, glycoproteins, lipids and their characteristic C–O–H in-plane bending peaks and $C(CH_3)_2$ symmetric stretching were present. Finally, in the range 900–1100 cm^{-1}, peaks due to the DNA/RNA backbone and phosphate groups of nucleic acids due to the symmetric and asymmetric stretching of P=O and P–O–C groups were visible. The spectrum of *E. coli* deposited on Si is provided as a reference in the inset.

Detection of *E. coli* with other functionalization methods

To understand the best method for pathogen capture, the direct absorption of the pathogens (*E. coli* O157:H7 and K12) on a titania thin film (Figure 5a), on films with only the specific antibody for *E. coli* O157:H7, and on films with APTES and Ab (Figure 5c) were tested. Figure 5a shows the FTIR spectra of different strains of *E. coli* (O157:H7 and K12) adsorbed onto the film surface with electrostatic interactions, illustrating that the substrate cannot discriminate between different strains and the different spectra of the pathogens are clearly visible. In contrast, in films with specific antibodies, only the binding of *E. coli* O157:H7 was visible and is reported in Figure 5b and 5c, although in films with APTES the presence of pathogens is poor.

Comparing the different immobilization techniques of detection (Figure 2 and Figure 5), the best result was obtained with the method that provided the covalent binding of the Ab on the film surface with APTES and GA (Figure 2d, dotted line), as expected. The other methods allowed the immobilization of bacteria, although not selectively, or with a low sensitivity of the device. In fact only the device shown in Figure 2 is selective and does not allow the linking of other subspecies of *E. coli* (*E. coli* K12), while on titania films (Figure 5a) it was possible to entrap pathogens with electrostatic interactions not differentiating between pathogens.

Determination of the detection limits of *E. coli* O157:H7

Tests to establish the detection limit of the device were carried out using serial dilutions of *E. coli* ranging in concentration from 1 × 10^8 CFU/mL to 10 CFU/mL; the dilutions were valid-

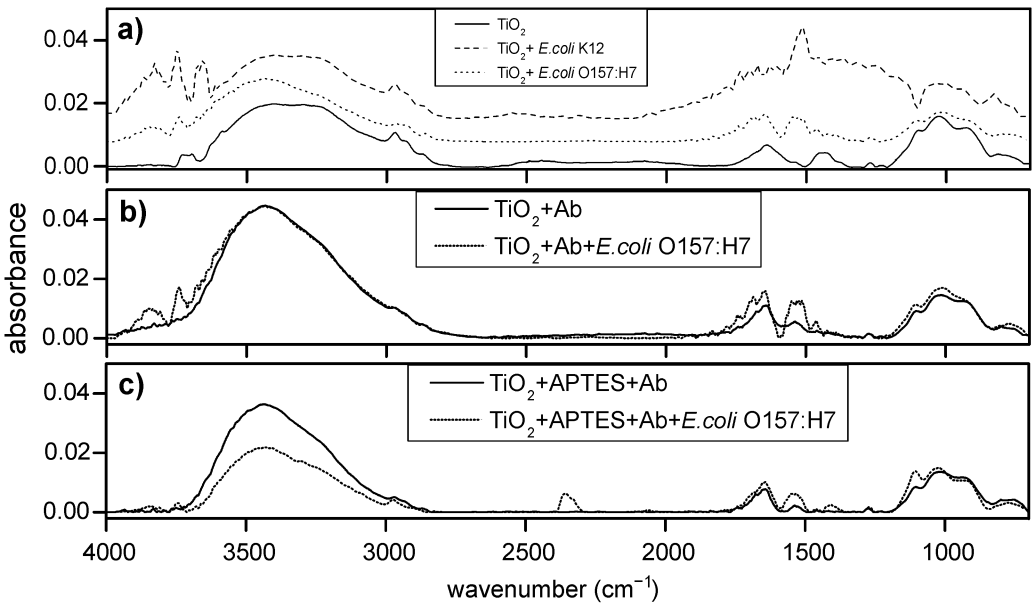

Figure 5: (a) FTIR spectrum of mesoporous titania films before (solid line) and after the immobilization of pathogens *E. coli* O157:H7 (dotted line) and *E. coli* K12 (dashed line). (b) FTIR spectrum of mesoporous titania films functionalized with anti-*E. coli* O157:H7-antibody (solid line) and after the immobilization of the pathogen (dotted line). (c) FTIR spectrum of titania films with APTES and antibody (solid line) and after the immobilization of *E. coli* (dotted line).

ated with the standard colony counting method (Figure 6) and DNA analysis was achieved by RT–PCR (Figure 7). These experiments were evaluated on mesoporous titania films functionalized with APTES–GA–anti-*E. coli* O157:H7-antibody, and a limit of detection of 1 × 10^2 CFU/mL (Figure 8) was achieved for *E. coli* O157:H7. A test with *E. coli* K12 was also carried out, but the spectrum of the functionalized chip did not show any peak due to this strain, because of the selectivity of the antibody, illustrating the specificity of the binding. Finally, colony micrographs of functionalized films after the immobilization of *E. coli* O157:H7 at different concentrations were collected with an optical microscope (Figure 9).

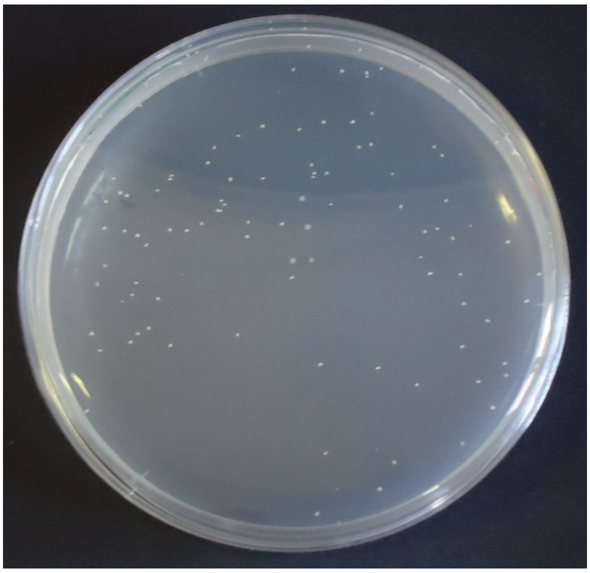

Figure 6: Colony counting method on a Petri plate with PCA and *E. coli* O157:H7 at a dilution of 10^{-6}.

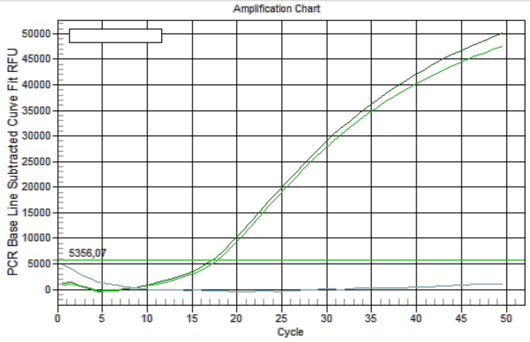

Figure 7: RT–PCR of DNA extracted from the nutrient broth. The blue line is the blank, the light green curve is the reference sample and the green curve is the DNA analysed.

Conclusion

The detection of *E. coli* O157:H7 by using an FTIR platform, through the linking of specific antibodies to mesoporous titania thin films was demonstrated. Cross-linking tethers were used to immobilize antibodies effectively through a chemical method. *E. coli* O157:H7 was identified and classified with standard methods and according to its infrared signature. Nanomaterials used for the immobilization and detection of pathogens, enabled

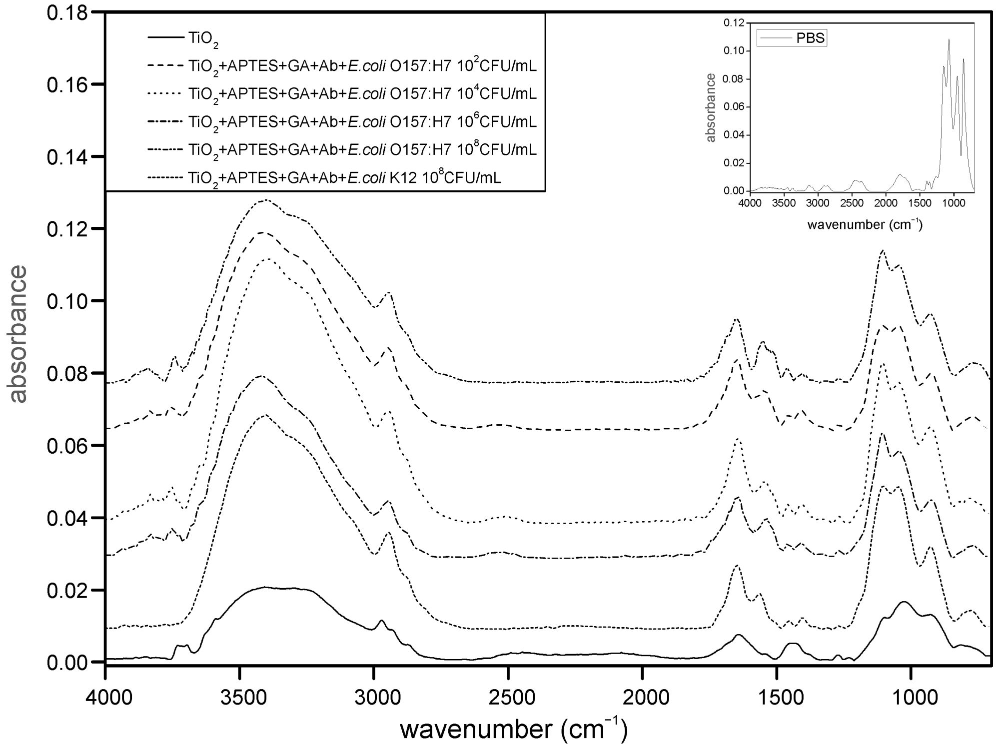

Figure 8: FTIR spectra of titania films alone (solid line) and functionalized with APTES–GA–anti-*E. coli* O157:H7-Ab after exposure to different concentrations of *E. coli* O157:H7 (10^8–10^2 CFU/mL) and *E. coli* K12 (10^8 CFU/mL) in order from the top to the bottom. The negative control of PBS is reported in the inset.

the possible capture of *E. coli* in less than 30 min. The benefit of this approach is specificity due to the antibodies and the characteristic fingerprint of the pathogens. In this way we demonstrated, as with the new biosensor, through a FTIR measurement and a short time for the analysis, that it is possible to discriminate in a selective manner whether a water sample is contaminated with *E. coli* O157:H7. This proposed device can also be adapted for in-field analysis if treated titania films, designed for specific pathogens, can be integrated with portable instruments for the direct assessment of pathogenic contaminants in food systems.

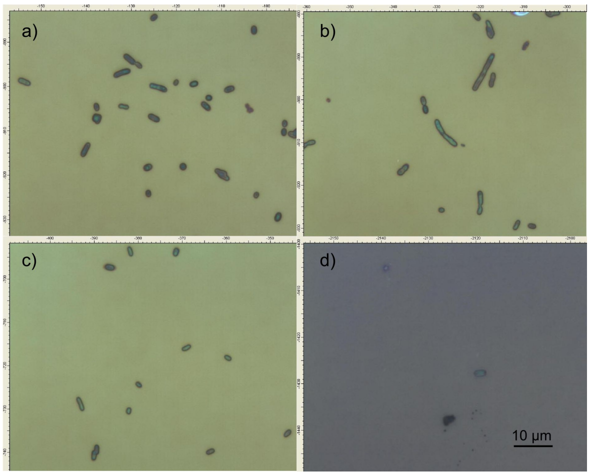

Figure 9: Colony micrographs of *E. coli* O157:H7 immobilized on mesoporous titania films functionalized with APTES–GA–anti-*E. coli* O157:H7-Ab, after exposure to different concentrations of *E. coli* O157:H7. (a) 10^6 CFU/mL; (b) 10^4 CFU/mL; (c) 10^2 CFU/mL; (d) 10 CFU/mL.

Acknowledgements

This work was a collaboration between the University of Sassari, the University of Milan and the Center for Food Safety Engineering at Purdue University. The project was financed by Legge 7, Regione autonoma della Sardegna, IDRISK Project. Thanks are given to Reeta Davis, Purdue University and Porto Conte ricerche for the use of instruments and to Dr. Lollai of the Istituto zooprofilattico Sassari.

References

1. Ivnitski, D.; Abdel-Hamid, I.; Atanasov, P.; Wilkins, E. *Biosens. Bioelectron.* **1999,** *14,* 599–624. doi:10.1016/S0956-5663(99)00039-1
2. Chemburu, S.; Wilkins, E.; Abdel-Hamid, I. *Biosens. Bioelectron.* **2005,** *21,* 491–499. doi:10.1016/j.bios.2004.11.025
3. Alocilja, E. C.; Radke, S. M. *Biosens. Bioelectron.* **2003,** *18,* 841–846. doi:10.1016/S0956-5663(03)00009-5

4. Buchanan, R. L.; Doly, M. P. *Food Technol.* **1997,** *51,* 69–76.
5. Rowe, P. C.; Orrbine, E.; Wells, G. A.; McLaine, P. N. *J. Pediatr.* **1991,** *119,* 218–224. doi:10.1016/S0022-3476(05)80730-9
6. Leonard, P.; Hearty, S.; Brennan, J.; Dunne, L.; Quinn, J.; Chakraborty, T.; O'Kennedy, R. *Enzyme Microb. Technol.* **2003,** *32,* 3–13. doi:10.1016/S0141-0229(02)00232-6
7. de Boer, E.; Beumer, R. R. *Int. J. Food Microbiol.* **1999,** *50,* 119–130. doi:10.1016/S0168-1605(99)00081-1
8. Velusamy, V.; Arshak, K.; Korostynska, O.; Oliwa, K.; Adley, C. *Biotechnol. Adv.* **2010,** *28,* 232–254. doi:10.1016/j.biotechadv.2009.12.004
9. Iqbal, S. S.; Mayo, M. W.; Bruno, J. G.; Bronk, B. V.; Batt, C. A.; Chambers, J. P. *Biosens. Bioelectron.* **2000,** *15,* 549–578. doi:10.1016/S0956-5663(00)00108-1
10. Brooks, B. W.; Devenish, J.; Lutze-Wallace, C. L.; Milnes, D.; Robertson, R. H.; Berlie-Surujballi, G. *Vet. Microbiol.* **2004,** *103,* 77–84. doi:10.1016/j.vetmic.2004.07.008
11. Touron, A.; Berthe, T.; Pawlak, B.; Petit, F. *Res. Microbiol.* **2005,** *156,* 541–553. doi:10.1016/j.resmic.2005.01.001
12. Murphy, N. M.; McLauchlin, J.; Ohai, C.; Grant, K. A. *Int. J. Food Microbiol.* **2007,** *120,* 110–119. doi:10.1016/j.ijfoodmicro.2007.06.006
13. Ravindranath, S. P.; Mauer, L. J.; Deb-Roy, C.; Irudayaraj, J. *Anal. Chem.* **2009,** *81,* 2840–2846. doi:10.1021/ac802158y
14. Schemberg, J.; Grodrian, A.; Römer, R.; Gastrock, G.; Lemke, K. *Phys. Status Solidi A* **2010,** *207,* 904–912. doi:10.1002/pssa.200983315
15. Varshney, M.; Li, Y.; Srinivasan, B.; Tung, S. *Sens. Actuators, B* **2007,** *128,* 99–107. doi:10.1016/j.snb.2007.03.045
16. Zhu, Y.; Koh, W. C. A.; Shim, Y.-B. *Electroanalysis* **2010,** *22,* 2908–2914. doi:10.1002/elan.201000394
17. Mello, L. D.; Kubota, L. T. *Food Chem.* **2002,** *77,* 237–256. doi:10.1016/S0308-8146(02)00104-8
18. Pérez-López, B.; Merkoçi, A. *Trends Food Sci. Technol.* **2011,** *22,* 625–639. doi:10.1016/j.tifs.2011.04.001
19. Arora, P.; Sindhu, A.; Dilbaghi, N.; Chaudhury, A. *Biosens. Bioelectron.* **2011,** *28,* 1–12. doi:10.1016/j.bios.2011.06.002
20. Su, L.; Jia, W.; Hou, C.; Lei, Y. *Biosens. Bioelectron.* **2011,** *26,* 1788–1799. doi:10.1016/j.bios.2010.09.005
21. Sakamoto, C.; Yamaguchi, N.; Yamada, M.; Nagase, H.; Seki, M.; Nasu, M. *J. Microbiol. Methods* **2007,** *68,* 643–647. doi:10.1016/j.mimet.2006.11.003
22. Lazcka, O.; Del Campo, F. J.; Muñoz, F. X. *Biosens. Bioelectron.* **2007,** *22,* 1205–1217. doi:10.1016/j.bios.2006.06.036
23. Liu, Y.; Li, Y. *Anal. Chem.* **2001,** *73,* 5180–5183. doi:10.1021/ac0104936
24. Wolter, A.; Niessner, R.; Seidel, M. *Anal. Chem.* **2008,** *80,* 5854–5863. doi:10.1021/ac800318b
25. Acharya, G.; Chang, C.-L.; Savran, C. *J. Am. Chem. Soc.* **2006,** *128,* 3862–3863. doi:10.1021/ja057490l
26. Mura, S.; Greppi, G. F.; Roggio, A. M.; Malfatti, L.; Innocenzi, P. *Microporous Mesoporous Mater.* **2011,** *142,* 1–6. doi:10.1016/j.micromeso.2010.10.047
27. Sivakesava, S.; Irudayaraj, J.; DebRoy, C. *Trans. ASABE* **2004,** *7,* 951–957.

License and Terms

Beilstein Journal
of Nanotechnology

Low-temperature synthesis of carbon nanotubes on indium tin oxide electrodes for organic solar cells

Andrea Capasso*[1], Luigi Salamandra[2], Aldo Di Carlo[2], John M. Bell[1]
and Nunzio Motta[1]

Full Research Paper

Address:
[1]School of Chemistry Physics and Mechanical Engineering, Queensland University of Technology, George St, 4000 Brisbane, Australia and [2]CHOSE (Centre for Hybrid and Organic Solar Energy), Department of Electronic Engineering, University of Rome Tor Vergata, Via del Politecnico 1, 00133 Rome, Italy

Email:
Andrea Capasso* - a.capasso@qut.edu.au

* Corresponding author

Keywords:
carbon nanotubes; electrode; indium tin oxide; Kelvin probe; organic photovoltaics

Beilstein J. Nanotechnol. **2012,** *3,* 524–532.
doi:10.3762/bjnano.3.60

Received: 10 April 2012
Accepted: 03 July 2012
Published: 19 July 2012

This article is part of the Thematic Series "Nanostructures for sensors, electronics, energy and environment".

Associate Editor: A. Gölzhäuser

Abstract

The electrical performance of indium tin oxide (ITO) coated glass was improved by including a controlled layer of carbon nanotubes directly on top of the ITO film. Multiwall carbon nanotubes (MWCNTs) were synthesized by chemical vapor deposition, using ultrathin Fe layers as catalyst. The process parameters (temperature, gas flow and duration) were carefully refined to obtain the appropriate size and density of MWCNTs with a minimum decrease of the light harvesting in the cell. When used as anodes for organic solar cells based on poly(3-hexylthiophene) (P3HT) and phenyl-C61-butyric acid methyl ester (PCBM), the MWCNT-enhanced electrodes are found to improve the charge-carrier extraction from the photoactive blend, thanks to the additional percolation paths provided by the CNTs. The work function of as-modified ITO surfaces was measured by the Kelvin probe method to be 4.95 eV, resulting in an improved matching to the highest occupied molecular orbital level of the P3HT. This is in turn expected to increase the hole transport and collection at the anode, contributing to the significant increase of current density and open-circuit voltage observed in test cells created with such MWCNT-enhanced electrodes.

Introduction

Following the original proposal for the creation of plastic solar cells [1], many research efforts have been recently directed to improve their power-conversion efficiency (PCE), in order to make these cells commercially viable [2]. The most promising active materials for organic cells are semiconducting polymers and fullerene derivatives, whose mixtures result in the formation of an interpenetrated phase consisting of nanoscaled bulk heterojunctions [1]. High performance has been predicted theoretically for these devices, which are characterized by low processing costs and mechanical flexibility [3], making them particularly attractive in comparison to those based on crystalline silicon and on other expensive inorganic semiconductors.

At present, the most successful and widespread blend for organic photovoltaics is based on a composite of poly(3-hexylthiophene) (P3HT) and phenyl-C_{61}-butyric acid methyl (PCBM) [4,5]. In this cell architecture the polymer acts as an electron donor and the fullerene derivative acts as an electron acceptor [6]. The holes move in the polymeric phase towards the anode, while the electrons hop along the fullerenes and eventually reach the cathode. Since the diffusion length of the exciton in the polymers is very low, recombination is highly probable, unless the electron is quickly injected into the carbon (acceptor) phase. Unfortunately, the concurrence of a low electrical mobility (due to the hopping mechanism) with a small exciton diffusion length increases the likelihood of charge recombination, ultimately affecting the overall PCE of the cells [7]. Many approaches have been proposed in order to overcome such fundamental issues and to improve the performances of P3HT:PCBM solar cells. In particular, very promising advances can be gained by increasing the nanoscale ordering of the polymer/fullerene composite. Different means have been proposed, such as thermal [8] and solvent annealing [9], or the use of additives in the blend preparation [10].

Along with fullerenes, carbon nanotubes (CNTs) have also been suggested as promising materials to boost solar cell PCE, thanks to their excellent electrical properties and to a favorable aspect ratio [11]. In fact, CNTs were initially suggested as a replacement for fullerene [12], because of their ability to create percolation paths through the heterostructure, while providing electron–hole dissociation sites. Being that the electron mobility in fullerenes is rather low [13-15], the initial motivation for the replacement of PCBM with CNTs was an expected increase in electron mobility due to ballistic transport in the CNT phase. Besides, microscopic studies proved that in a mixture of P3HT and CNTs, the polymer self-assembles and wraps the carbon nanostructure, generating a bulk heterojunction with a large interface area over which a strong electric field would lead to a high probability of exciton dissociation [16]. However, the lack of control over the selection of the CNTs has made their integration with polymers quite unsuccessful so far [17], as recently suggested by photoluminescence studies [18]. In fact, when P3HT is mixed with both semiconducting and metallic CNTs, the latter tend to create Schottky barriers [16,19] at the polymer–CNT interface, which can favor the electron–hole recombination and thus decrease the short-circuit current. This has been also confirmed by Valentini et al. [20], who were able to attain a marked increase in the short-circuit current of the cell by depositing only semiconducting CNTs on the ITO surface. Nevertheless, this situation is still under debate, since efficient electron–hole separation has been recently observed in P3HT mixed with metallic and semiconducting CNTs [21], suggesting that both kinds of nanotubes could ultimately act as hole acceptors.

Whatever the solution to this puzzle is, including MWCNTs in a blend of P3HT and PCBM matches the key objective of achieving large interfacial areas within a bulk donor–acceptor heterojunction mixture, as proposed by Berson et al. [22]. As metallic conductors, MWCNTs are expected to lower the electrical percolation threshold even at minimal concentrations, due to their high electron conductivity and their shape. Following this line, Sun [2] proposed the assembly of a cell containing a network of vertically aligned CNTs separated by vertical polymer layers. The realization of this idea would grant a major increase in conductivity at the electrode (thanks to the interpenetrating structure of vertically aligned nanotubes), but it has not been completely exploited so far, because of its intrinsic complexity. Nonetheless, as a first attempt in this direction, Miller et al. [23] reported the synthesis of CNTs directly on ITO–glass by chemical vapor deposition (CVD). Although successful in terms of CNT yield, their method did not provide a specific control over the assembly of the CNTs, whose high density rendered the ITO electrode almost opaque. Conversely, in this paper we present the first evidence of the controlled growth of MWCNTs on ITO electrodes, obtained by a fine tuning of the CVD parameters, such as temperature, gas flow, and duration. By selecting the optimal combination of these parameters it is possible to create MWCNT mats with the required size and density on the ITO-coated glass surface. Such CNT-enhanced electrodes are found to show advantages in terms of work-function (WF) matching and electrical properties in comparison with pristine ITO electrodes, contributing to the significant advancement of the overall PCE of the solar cell.

Results and Discussion

After preliminary tests in CVD, SEM and EDX analysis indicated that the range of temperature of 550–600 °C has to be avoided for the application of the ITO-substrates as electrodes, since the ITO layer undergoes severe disruption at such high temperatures, becoming no longer conductive. The growth time was also inspected, determining an optimal CNT synthesis time of 30 min. Successful growth of MWCNTs was obtained on Samples A, B and C, treated in CVD for 30 min at 550, 525 and 500 °C respectively (Figure 1).

The transmittance and the resistivity of each electrode were measured and are reported in Table 1. The density distribution of the tubes is found to scale considerably with the deposition temperature. On Sample A (550 °C), a dense and thick layer of MWCNTs covers the entire ITO area. Due to the CNT density,

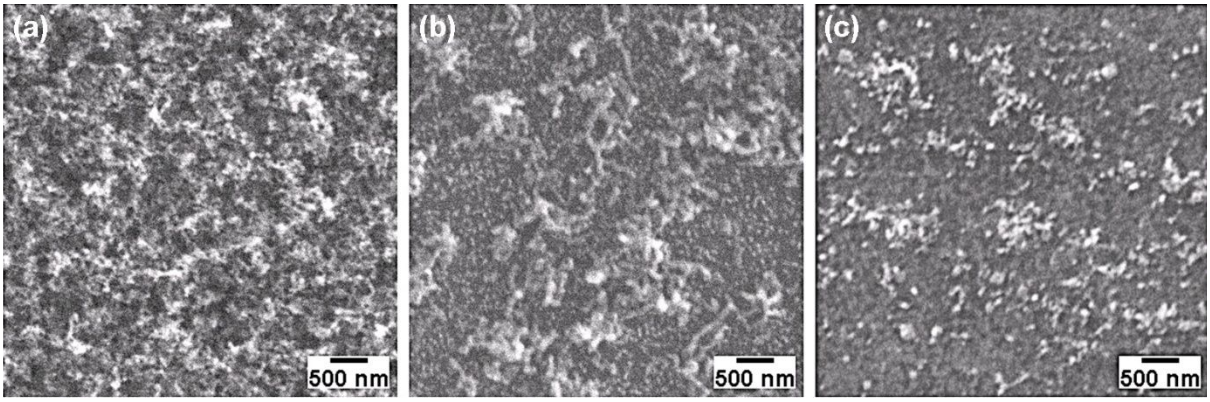

Figure 1: SEM images of MWCNTs grown on ITO-coated glass by CVD at: (a) 550 °C, (b) 525 °C, (c) 500 °C.

Table 1: Growth parameters and properties for the three CNT-enhanced electrodes compared to pure glass and to ITO/glass sample.

sample	growth *T* [°C]	R [Ω/sq] ITO film	transmittance at 510 nm [%]
glass	—	—	89
glass/ITO	—	15	81
Sample C (glass/ITO+CNT)	500	25	75
Sample B (glass/ITO+CNT)	525	33	45
Sample A (glass/ITO+CNT)	550	40	0

the substrate looks almost black and is therefore no longer transparent. In addition, the sheet resistance of the ITO layer increased to 40 Ω/sq (almost three times higher than that for pristine ITO). When heated in air at 550 °C, the polycrystalline ITO layer is known to degrade, leading to the segregation of Sn into clusters hundreds of nanometers in diameter [24], and also to increased inter-diffusion between the substrate and film [25]. Both effects can reduce the film conductivity by up to 50%, as reported elsewhere [26].

In our case, the interaction of the ITO film with the CVD process gases at 550 °C is expected to deteriorate the conductivity of the electrode even more strongly. This is partly supported by the formation of microspheres of indium on the ITO film, as observed by SEM and EDX (not shown). Similarly to what was reported by Lan et al. [27], we suggest that the exposure of the ITO film to a hydrogen atmosphere at 550 °C (and the probable creation of atomic hydrogen coming from the dissociation of either H_2 or C_2H_2, perhaps enabled by the metal catalyst layer) enables the formation of small clusters of metallic indium, which coalesce during the CVD to form spherical particles with a typical size of >2 µm. As a consequence, the film surface would segregate and change its chemical ratio. The film conductivity will in turn significantly decrease, as will the optical transmittance, on account of a stronger light absorption and scattering caused by those metallic microspheres.

In contrast, at 525 °C (Sample B) and 500 °C (Sample C), the degradation is not as severe and the conductivity of the film is still acceptable (25–30 Ω/sq). In these two cases the nanotubes nucleate with a lower density, and the substrates show a transmittance at 515 nm of 45 and 75%, respectively. Figure 2 illustrates the optical transmittance of these two samples in the wavelength range of 350–750 nm, taking also into consideration the absorption spectrum of the P3HT:PCBM blend.

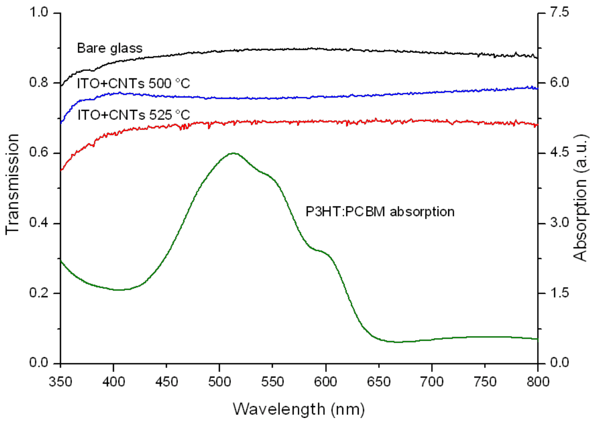

Figure 2: Transmittance spectra of the electrodes (left Y axis), compared to the absorption spectrum of the P3HT:PCBM blend (right Y axis).

Although on Sample B the density of the CNT carpet is much higher than on Sample C, for the present purpose, an optimal condition is reached with the latter sample. When a temperature of 500 °C is used, the short sparse tubes (average density of 10 tubes/µm^2) that grow do not form bundles or thick aggregates, allowing more light to pass through the electrode and to reach the active layer of the cell. SEM images taken in various sites of Sample C (as the one in Figure 3a) were analyzed to calculate the average dimensions of the grown MWCNTs. The average length of the tubes is 100 nm and the diameter 40 nm, as confirmed by TEM analysis (Figure 3b). Due to the low synthesis temperature the tube structure is very defective and residual allotropes of carbon, such as diamond-like and amorphous carbon, are found around the nanotube walls (confirmed also by Raman spectroscopy, not shown).

In our context, the presence of defects in the tubular structure could be an advantage in terms of conductivity, because it can induce cross linking between the inner shells (walls) of the tubes through sp^3 bond formation, facilitating charge-carrier hopping to inner shells [28]. Such intershell bridging provides additional charge-carrier transport pathways, offsetting the effect of a conductivity decrease induced by defect scattering.

By measuring various areas of the sample, a mean distribution of 10 MWCNT/µm^2 has been estimated, being that the average dimensions of nanotubes are 100 nm in length, 30 nm in diameter, and 58 m^2/g for the specific surface area [29]. Such values would entail an increase of 10% in the overall surface area of the CNT/ITO electrode in comparison with the planar ITO film. We believe that such three-dimensional and nanostructured electrodes, made of metallic nanotubes [30], will be able to penetrate the P3HT:PCBM blend and ease the extraction of holes to the external circuit.

Using Sample C, we measured the WF of the as-created electrode. Kelvin probe and ultraviolet photoelectron spectroscopy (UPS) are the techniques usually employed for this purpose; however, there are substantial differences in how the WF is measured. The Kelvin probe method measures, in air, the difference in WF between a millimetric probe and the sample, which can undergo surface reactions with species adsorbed from the environment. Conversely, UPS measures, in ultrahigh vacuum, the lowest WF of a small portion of the surface, usually a few microns in diameter. WF values measured by the Kelvin probe method are often higher than those measured by UPS [31], due to the influence of the ambient gases and to the fact that the probe size typically covers an area of few millimeters squared. Therefore, we chose to use the Kelvin probe method as it is able to measure the electrode WF in its working environment, just before the cell is built.

After a fine calibration with a reference tantalum foil, the WF of an untreated and clean ITO substrate was found to be 4.80 eV. We then measured a value of 4.95 eV in the case of our CNT-enhanced electrode, that is, an increase of 0.15 eV. Although this value is in good agreement with the WF of MWCNTs reported by Shiraishi et al. [32], we have to make two considerations: (i) our substrate is not fully covered by a continuous, dense mat of nanotubes; (ii) when measuring by Kelvin probe method, the electrode under test is the whole structure CNT/ITO, not only the CNT overlayer; (iii) a thin layer of Fe is also present between the ITO and the CNT layer, even if during the CVD it should become segregated into small particles, giving rise to the nucleation of the tubes.

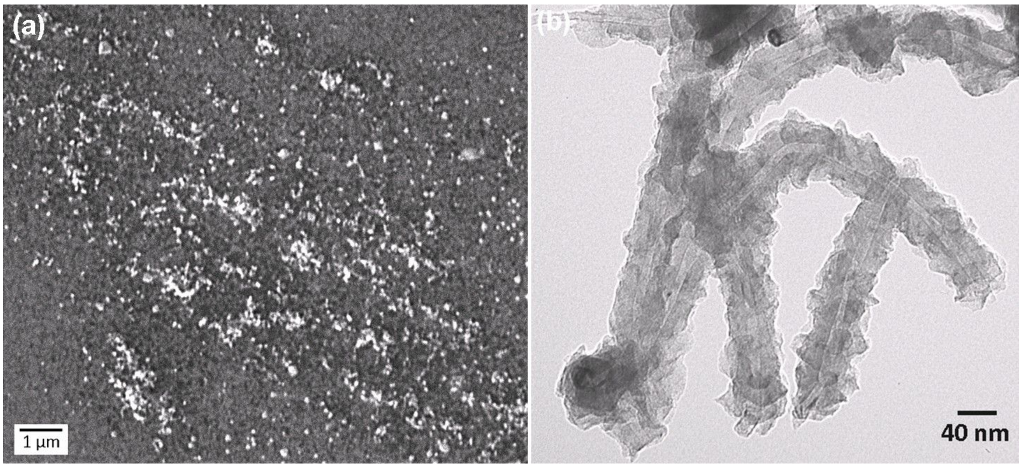

Figure 3: (a) SEM image showing the surface of Sample C, on which a low density mat of MWCNTs is grown after CVD at 500 °C for 30 min. (b) TEM image of CNTs from Sample B (grown in CVD for 30 min at 525 °C).

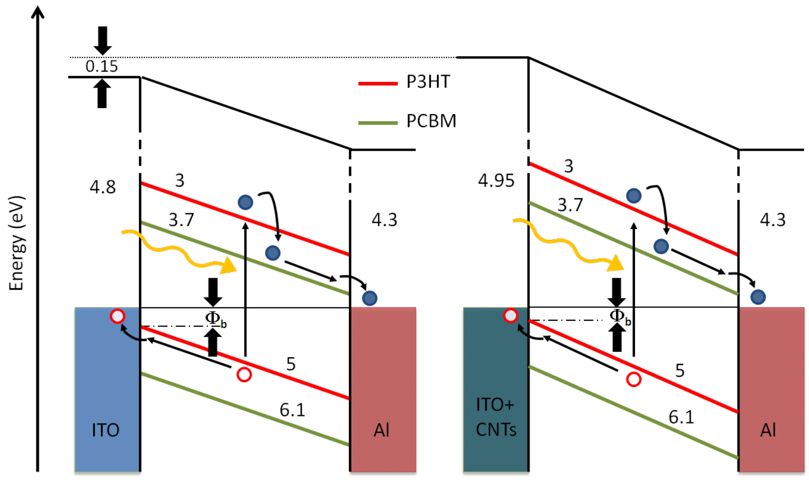

Figure 4: WF levels for cells with ITO (left) and ITO–CNT (right) electrode. (All reported values are in eV and negative).

All of these occurrences, instead of the sole CNT contribution, would partake in establishing the WF measured for the ITO–CNT electrode (as depicted in Figure 4). Nevertheless, this increase in WF is strongly beneficial because it brings the electrode WF closer to that of the photoactive blend. Thus we anticipate a reduction in the hole–injection barrier at the anode interface, as a result of the highest occupied states of ITO–CNT lying lower than those of ITO.

A similar kind of band alignment is almost achieved in the standard cell architecture by the insertion of a layer of poly(3,4-ethylene dioxythiophene):(polystyrene sulfonic acid) (PEDOT:PSS). This polymer is used to improve the contact (and reduce the mismatch in energy level) between the ITO and the P3HT, although it is also known to shorten the device lifetime [33]. Being slightly acidic, the PEDOT:PSS is in fact able to etch the ITO and causes interface instability through indium diffusion into the polymer active layer. In our case instead, we believe that using a mat of MWCNTs as a functional buffer layer for ITO should guarantee an increase in both the charge collection and in the lifetime of the device.

In order to test the last statement, test organic solar cells were built with two of our CNT-enhanced anodes: sample C (whose characterization have been presented and discussed above) for cell C, and sample C1 (treated with the same CVD conditions of sample C but for a shorter time of 15 min instead of 30 min) for cell C1. The *I–V* curve and the output power generated by the cells made with our electrodes are reported in Figure 5a, in comparison with the data obtained for a reference cell made with a standard ITO-coated glass anode (i.e., without the addition of PEDOT:PSS). The *I–V* characteristic of a standard ITO/PEDOT:PSS/P3HT:PCBM/Al cell is also reported in Figure 5b, for a full understanding of the experimental results. All the numeric values are reported in Table 2, along with the respective PCEs.

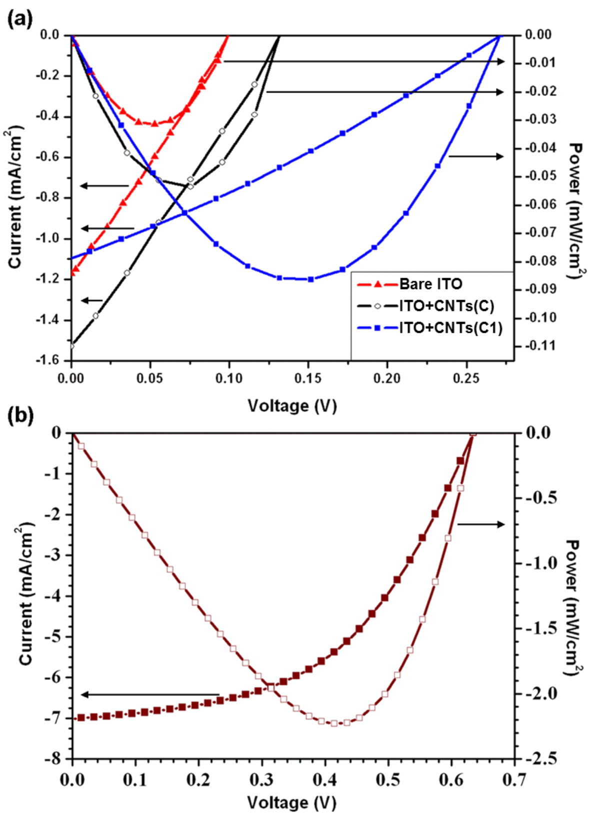

Figure 5: Current–voltage characteristic and output power of P3HT:PCBM solar cells: (a) Cell C and cell C1, compared to a reference cell made with bare ITO-coated glass; (b) classic ITO/PEDOT:PSS/P3HT:PCBM/Al cell manufactured in our labs.

As a preliminary remark, it has to be pointed out that the overall PCE of the experimental cells suffers from the lack of those beneficial effects that are acknowledged by the inclusion of a PEDOT:PSS layer between the ITO and active blend, particularly an advantageous interface morphology [34] that enables higher J_{sc} and fill factor (FF). On the other hand, the comparison between experimental devices made with pristine and CNT-enhanced ITO–glass demonstrates the substantial improvement that the addition of CNTs affords to the electrical properties of the electrode.

By analyzing the I–V graphs, one readily notices how the two CNT-enhanced electrodes dramatically contribute to an increase of the open-circuit voltage (V_{oc}) of the cell. Remarkably, in the case of cell C1, V_{oc} reached 272 mV, which is almost three times higher than the value measured for the reference cell made with bare ITO (~100 mV). Such a consistent improvement in V_{oc} is due to the optimal alignment of the energy levels between the CNT-modified ITO WF (~4.95 eV) and the P3HT HOMO (~5 eV), on the account of a fostered hole collection at the anode/polymer interface. Besides, by taking into consideration an equivalent-circuit diagram for a bulk heterojunction solar cell (Figure 6), we highlight that the CNTs could be also responsible of a quenched recombination both at the dissociation sites (e.g., donor/acceptor interfaces) and near the anode (as a result of an increase of the shunt resistor R_{sh}), with a further positive effect on the V_{oc}.

Moreover, we propose that our electrode could contribute to the reduction of the series resistance R_s of the cell by means of the addition of shorter and direct paths for charge collection, which are on average provided by the MWCNTs (having intrinsically a very high aspect ratio). This helps in overcoming the low mobility of the holes, now able to travel more quickly than in the pure P3HT phase, and implies a corresponding increase in J_{sc}. In particular, the J_{sc} is expected to benefit from the numerous percolation paths created by the CNTs, which can effectively drive away the free carriers generated from the dissociation of the excitons at the dispersed heterojunctions.

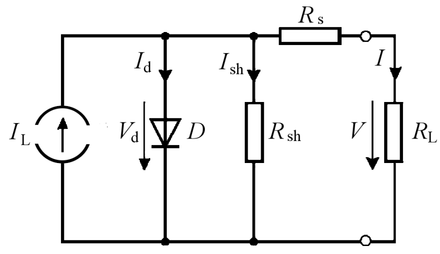

Figure 6: Equivalent circuit of the ideal organic solar cell.

We observe, however, that the J_{sc} exhibits a noteworthy 40% increase in the case of cell C, but it does not vary much for sample C1. This different behavior for two electrodes prepared with the same procedure must be explained in terms of the only parameter varied, i.e., the CVD time. Consistently with the widely known CNT growth mechanism, the shorter CVD time used for sample C1 (15 min) leads to a shorter length of the grown CNTs: as a result, we speculate that the occurrence of short circuits between the two electrodes should be less likely in this case. Hence, the V_{oc} is expected to augment correspondingly, while the charge collection and hence the J_{sc} are less enhanced by the shorter transport paths.

Conversely, the formation of an extra blocking contact (e.g., for holes at the ITO electrode) can be the reason for the small FF values found, which increases only by ~5% in the case of sample C1. This could be considered in the equivalent circuit with the insertion of a counter diode D2 or by another shunt R_{sh} that directly connects the two electrodes.

As already stated, the absolute efficiency of our cell is not as relevant in the present work as the comparison with the bare ITO cell is. Even without the good ohmic contact provided by PEDOT:PSS, our devices show major improvement in electric performance. In fact, the overall increase in PCE is still more noticeable when considering the lower transparency (due to the CNTs layer) and the higher resistivity (due to thermal and chemical degradation) of the treated ITO film. Nonetheless, CNT-enhanced electrodes may be used in conjunction with a layer of PEDOT:PSS to further advance the PCE of OSCs; or, once the process would be refined, they could become a suitable replacement for PEDOT:PSS, with the aim of improving the interface morphology without compromising the long-term

Table 2: Characteristics of the organic solar cells: open-circuit voltage (V_{oc}), short-circuit current density (J_{sc}), fill factor (FF) and power conversion efficiency (η).

cell	V_{oc} [mV]	J_{sc} [mA/cm^2]	FF [%]	η [%]
ITO/P3HT:PCBM/Al	100	−1.2	23	0.03
ITO–MWCNTs/P3HT:PCBM/Al (cell C)	140	−1.7	24	0.06
ITO–MWCNTs/P3HT:PCBM/Al (cell C1)	272	−1.1	29	0.09

stability of the cell. To this end, more research should be devoted to obtain a more uniform and ohmic contact between the CNTs and the P3HT. Our method could be further improved by exploring very low CVD temperatures (down to 350 °C), which have been reported as being unexpectedly suitable for CNT synthesis from Fe films [35].

Conclusion

We presented experimental evidence of the superior electrical behavior of CNT-enhanced ITO–glass electrodes in comparison to pristine ITO ones. When implemented in experimental P3HT:PCBM solar cells, such electrodes provide a 40% increase in PCE, in spite of the slight reduction of the cell transparency. We have grown a low density carpet of MWCNTs by using a very thin film of Fe catalyst on ITO-coated glass. By investigating the effect of the growth temperature on the nanotube yield and on the ITO layer, we have selected the optimal CVD conditions for the use of such substrates as anodes for P3HT:PCBM solar cells. These process conditions address three of the biggest hindrances that affected the PCE of polymer cells made from similarly treated electrodes, because in our case (i) the sheet resistance of the electrode undergoes a limited increase during the low temperature CVD; (ii) the light transmittance of the ITO–glass does not reduce much, thanks to the low nanotube density obtained with an ultrathin (2 nm) layer of catalyst; and (iii) the occurrence of short circuits with the counter electrode is limited by the short length of the CNTs. By using this set of parameters, we built a 3D nanostructured electrode that improved the performance of the cell both in terms of V_{oc} (40%) and J_{sc} (30%).

Experimental

MWCNTs were grown by CVD on borosilicate glass substrates coated by ITO stripes (Kintec Company, 15 Ω/sq, 100 nm thick). The substrates were cleaned by ultrasonic baths in acetone, ethanol and deionized water. Thin layers of Fe (~3 nm) were deposited as a catalyst by thermal evaporation. After the metal deposition, the substrates were loaded into a ceramic furnace for ambient-pressure CVD. The synthesis occurred in a temperature range of 500–600 °C, while a constant flow of 10% C_2H_2 in H_2 (15:150 sccm) was maintained. After CVD, the substrates were analyzed by SEM and EDX (FEI - Quanta 3D 200). Transmittance values of the as-prepared electrodes were acquired with a UV–vis spectrophotometer (Shimadzu UV-2550). Nanotube morphology was also investigated by TEM (Jeol 1011 TEM).

Bulk-heterojunction solar cells were built in a nitrogen atmosphere glovebox by using two of our CNT-enhanced ITO substrates as anodes (Figure 7). A solution (1:0.7) of regioregular poly(3-hexylthiophene) (P3HT, from Sigma-Aldrich) and phenyl-C_{61}-butyric acid methyl ester (PCBM, from Solenne BV) was diluted in ortho-dichlorobenzene and spin coated at 400 rpm onto CNT-enhanced ITO-coated glass, which had been previously cleaned with acetone and isopropyl alcohol in ultrasonic baths. A 100 nm thick Al cathode was then thermally

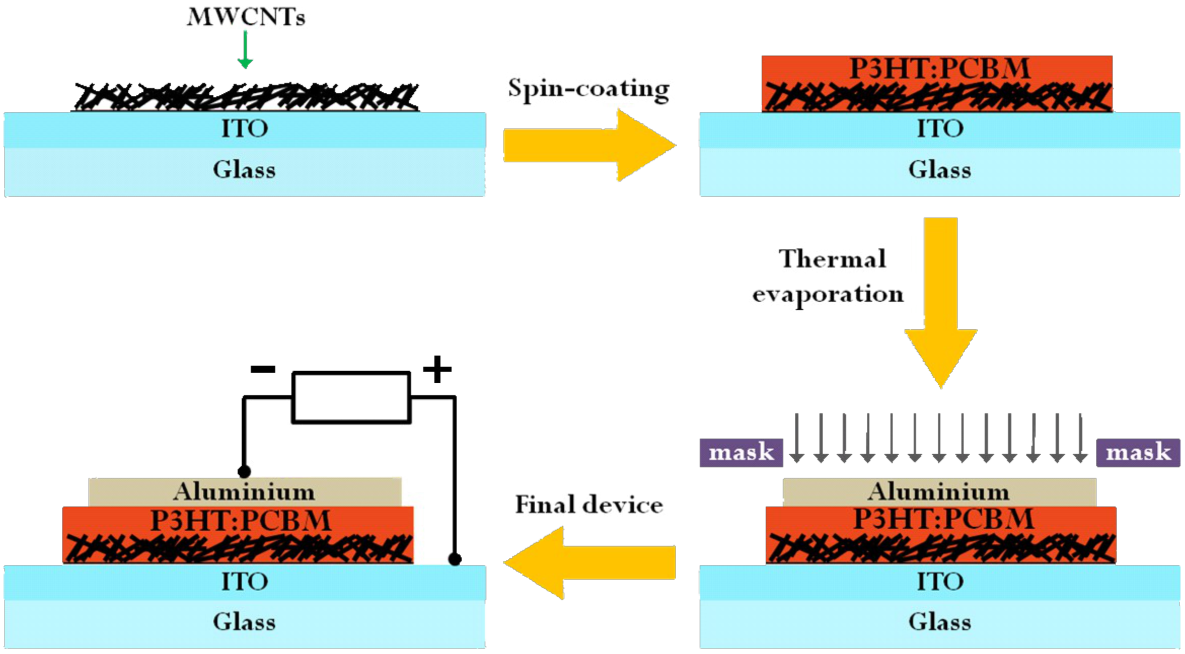

Figure 7: Schematics of the preparation of a P3HT:PCBM solar cell with CNT-enhanced ITO.

evaporated in high vacuum ($\sim 2 \times 10^{-6}$mbar), by using a shadow mask with 3 mm wide stripes. The final device had an active area of 25 mm^2. Reference cells with bare ITO-coated glass were also made for comparison with the same procedure. The current–voltage (I–V) characteristics under 1 sun (AM1.5G) were measured with an Agilent E5262A source meter.

Acknowledgements

The authors acknowledge the financial support of the Queensland State Government through the NIRAP Project “Solar powered nanosensors” and the Project “Polo Solare Organico - Regione Lazio”. One of the authors (A.C.) would like to thank Dr. Gianlorenzo Bussetti for his help and significant considerations to the work-function measurements, and Mr. Paul Moonie for critical reading of the manuscript.

References

1. Brabec, C. J.; Sariciftci, N. S.; Hummelen, J. C. *Adv. Funct. Mater.* **2001,** *11,* 15–26. doi:10.1002/1616-3028(200102)11:1<15::AID-ADFM15>3.0.CO;2-A
2. Sun, S.-S.; Sariciftci, N. S. *Organic photovoltaics: Mechanism, Materials and Devices;* Taylor & Francis: Boca Raton, FL, USA, 2005.
3. Abdou, M. S. A.; Holdcroft, S. *Chem. Mater.* **1994,** *6,* 962–968. doi:10.1021/cm00043a017
4. Li, G.; Shrotriya, V.; Huang, J.; Yao, Y.; Moriarty, T.; Emery, K.; Yang, Y. *Nat. Mater.* **2005,** *4,* 864–868. doi:10.1038/nmat1500
5. Dennler, G.; Scharber, M. C.; Brabec, C. J. *Adv. Mater.* **2009,** *21,* 1323–1338. doi:10.1002/adma.200801283
6. Umnov, A. G.; Korovyanko, O. J. *Appl. Phys. Lett.* **2005,** *87,* 113506. doi:10.1063/1.2048817
7. Mihailetchi, V. D.; Xie, H. X.; deBoer, B.; Koster, L. J. A.; Blom, P. W. M. *Adv. Funct. Mater.* **2006,** *16,* 699–708. doi:10.1002/adfm.200500420
8. Chu, C.-W.; Yang, H.; Hou, W.-J.; Huang, J.; Li, G.; Yang, Y. *Appl. Phys. Lett.* **2008,** *92,* 103306. doi:10.1063/1.2891884
9. Li, G.; Yao, Y.; Yang, H.; Shrotriya, V.; Yang, G.; Yang, Y. *Adv. Funct. Mater.* **2007,** *17,* 1636–1644. doi:10.1002/adfm.200600624
10. Ouyang, J.; Xia, Y. *Sol. Energy Mater. Sol. Cells* **2009,** *93,* 1592–1597. doi:10.1016/j.solmat.2009.04.015
11. Avouris, P. *Chem. Phys.* **2002,** *281,* 429–445. doi:10.1016/S0301-0104(02)00376-2
12. Kymakis, E.; Amaratunga, G. A. J. *Appl. Phys. Lett.* **2002,** *80,* 112–114. doi:10.1063/1.1428416
13. Kryszewski, M.; Jeszka, J. *Macromol. Symp.* **2003,** *194,* 75–86. doi:10.1002/masy.200390107
14. Adamopoulos, G.; Heiser, T.; Giovanella, U.; Ould-Saad, S.; van de Wetering, K. I.; Brochon, C.; Zorba, T.; Paraskevopoulos, K. M.; Hadziioannou, G. *Thin Solid Films* **2006,** *511–512,* 371–376. doi:10.1016/j.tsf.2005.12.029
15. Trznadel, M.; Pron, A.; Zagorska, M.; Chrzaszcz, R.; Pielichowski, J. *Macromolecules* **1998,** *31,* 5051–5058. doi:10.1021/ma970627a
16. Giulianini, M.; Waclawik, E. R.; Bell, J. M.; De Crescenzi, M.; Castrucci, P.; Scarselli, M.; Motta, N. *Appl. Phys. Lett.* **2009,** *95,* 013304. doi:10.1063/1.3173825
17. Kymakis, E.; Koudoumas, E.; Franghiadakis, I.; Amaratunga, G. A. J. *J. Phys. D: Appl. Phys.* **2006,** *39,* 1058–1062. doi:10.1088/0022-3727/39/6/010
18. Schuettfort, T.; Snaith, H. J.; Nish, A.; Nicholas, R. J. *Nanotechnology* **2010,** *21,* 025201. doi:10.1088/0957-4484/21/2/025201
19. Kanai, Y.; Grossman, J. C. *Nano Lett.* **2008,** *8,* 908–912. doi:10.1021/nl0732777
20. Valentini, L.; Cardinali, M.; Kenny, J. M. *Carbon* **2010,** *48,* 861–867. doi:10.1016/j.carbon.2009.10.040
21. Dissanayake, N. M.; Zhong, Z. *Nano Lett.* **2011,** *11,* 286–290. doi:10.1021/nl103879b
22. Berson, S.; de Bettignies, R.; Bailly, S.; Guillerez, S.; Jousselme, B. *Adv. Funct. Mater.* **2007,** *17,* 3363–3370. doi:10.1002/adfm.200700438
23. Miller, A. J.; Hatton, R. A.; Chen, G. Y.; Silva, S. R. P. *Appl. Phys. Lett.* **2007,** *90,* 023105. doi:10.1063/1.2431437
24. Hsu, W.-L.; Lin, C.-T.; Cheng, T.-H.; Yen, S.-C.; Liu, C.-W.; Tsai, D. P.; Lin, G.-R. *Chin. Opt. Lett.* **2009,** *7,* 263–265. doi:10.3788/COL20090703.0263
25. Bell, J. M.; Matthews, J. P. *Mater. Forum* **1998,** *22,* 1–24.
26. Zardetto, V.; Brown, T. M.; Reale, A.; Di Carlo, A. *J. Polym. Sci., Part B: Polym. Phys.* **2011,** *49,* 638–648. doi:10.1002/polb.22227
27. Lan, J.-H.; Kanicki, J. *Thin Solid Films* **1997,** *304,* 123–129. doi:10.1016/S0040-6090(97)00173-9
28. Agrawal, S.; Raghuveer, M. S.; Li, H.; Ramanath, G. *Appl. Phys. Lett.* **2007,** *90,* 193104. doi:10.1063/1.2737127
29. Peigney, A.; Laurent, C.; Flahaut, E.; Bacsa, R. R.; Rousset, A. *Carbon* **2001,** *39,* 507–514. doi:10.1016/S0008-6223(00)00155-X
30. Conductance in multiwall carbon nanotubes occurs by charge-carrier transport in the outermost shell. MWCNTs are metallic, because their large wall diameters ensure that even if the outermost shell is semiconducting, the band gap would be negligibly low (about 5 meV for a 50 nm diameter shell) to cause rectification. Defects and inner contacts are also so common among the walls that a conductive path for the charges would be on average always assured.
31. Kim, J. S.; Lägel, B.; Moons, E.; Johansson, N.; Baikie, I. D.; Salaneck, W. R.; Friend, R. H.; Cacialli, F. *Synth. Met.* **2000,** *111–112,* 311–314. doi:10.1016/S0379-6779(99)00354-9
32. Shiraishi, M.; Ata, M. *Carbon* **2001,** *39,* 1913–1917. doi:10.1016/S0008-6223(00)00322-5
33. Chen, L.-M.; Hong, Z.; Li, G.; Yang, Y. *Adv. Mater.* **2009,** *21,* 1434–1449. doi:10.1002/adma.200802854
34. de Kok, M. M.; Buechel, M.; Vulto, S. I. E.; van de Weijer, P.; Meulenkamp, E. A.; de Winter, S. H. P. M.; Mank, A. J. G.; Vorstenbosch, H. J. M.; Weijtens, C. H. L.; van Elsbergen, V. Modification of PEDOT:PSS As Hole Injection Layer in Polymer LEDs. In *Physics of Organic Semiconductors;* Brütting, W., Ed.; Wiley-VCH: Weinheim, Germany, 2005. doi:10.1002/3527606637.ch16
35. Cantoro, M.; Hofmann, S.; Pisana, S.; Scardaci, V.; Parvez, A.; Ducati, C.; Ferrari, A. C.; Blackburn, A. M.; Wang, K. Y.; Robertson, J. *Nano Lett.* **2006,** *6,* 1107–1112. doi:10.1021/nl060068y

License and Terms

Beilstein Journal
of Nanotechnology

A highly pH-sensitive nanowire field-effect transistor based on silicon on insulator

Denis E. Presnov[1,2], Sergey V. Amitonov[2], Pavel A. Krutitskii[3],
Valentina V. Kolybasova[2], Igor A. Devyatov[1], Vladimir A. Krupenin[2]
and Igor I. Soloviev*[1]

Full Research Paper

Open Access

Address:
[1]Lomonosov Moscow State University Skobeltsyn Institute of Nuclear Physics, Moscow 119991, Russia, [2]Laboratory of Cryoelectronics, Lomonosov Moscow State University, Moscow 119991, Russia and [3]Keldysh Institute of Applied Mathematics, Moscow 125047, Russia

Email:
Igor I. Soloviev* - igor.soloviev@gmail.com

* Corresponding author

Keywords:
charge/field sensor; field-effect transistor; nanowire; pH sensor; silicon-on-insulator

Beilstein J. Nanotechnol. **2013,** *4,* 330–335.
doi:10.3762/bjnano.4.38

Received: 08 February 2013
Accepted: 06 May 2013
Published: 28 May 2013

This article is part of the Thematic Series "Nanostructures for sensors, electronics, energy and environment".

Guest Editor: N. Motta

Abstract

Background: An experimental and theoretical study of a silicon-nanowire field-effect transistor made of silicon on insulator by CMOS-compatible methods is presented.

Results: A maximum Nernstian sensitivity to pH change of 59 mV/pH was obtained experimentally. The maximum charge sensitivity of the sensor was estimated to be on the order of a thousandth of the electron charge in subthreshold mode.

Conclusion: The sensitivity obtained for our sensor built in the CMOS-compatible top-down approach does not yield to the one of sensors built in bottom-up approaches. This provides a good background for the development of CMOS-compatible probes with primary signal processing on-chip.

Introduction

Over the past decade experimental and theoretical studies of semiconductor nanowire field-effect transistors (NW FET) made of silicon on insulator (SOI) have been of great interest to researchers. The large surface-to-volume ratio of the nanowire allows one to create extremely sensitive charge/field sensors in chemical and biological systems for the detection of charged particles and molecules at low concentrations [1-4]. It was shown [5] that the charge sensitivity of NW FET can reach a value of $60 \cdot 10^{-6} e/\sqrt{\text{Hz}}$ at 198 K (e is the electron charge), which is orders of magnitude better than conventional FET and nanomechanical systems. This extremely high sensitivity gives an opportunity to construct local potential probes with nanoscale lateral resolution based on NW FET. In comparison with single-electron transistors [6], it is easy to fabricate a device operating at room temperature, which can be useful for biological and medical applications. A demonstration of such a local probe based on a vapour–liquid–solid-method (VLS) grown silicon-nanowire (SiNW) FET was given in [7]. The sensitivity of this bioprobe to pH change near its maximum value of 59 mV per unit pH was reached and the intracellular electrical recording from beating cardiomyocytes was demonstrated. It was shown that this sensor charge sensitivity in subthreshold mode was around several tens of *e*. These outstanding results were obtained by methods incompatible with traditional semiconductor electronics.

In this work we present SiNW FET fabricated [8] by traditional methods from silicon-on-insulator (SOI) with a pH sensitivity equal to VLS-grown NW FET [7]. The maximum sensitivity in subthreshold mode is estimated to be on the order of $10^{-3}e/\sqrt{\mathrm{Hz}}$.

Results and Discussion

In Figure 1 a NW FET with a channel length of 5 µm and a width of 100 nm is presented. We used Soitec SOI wafers with a device layer of 55 nm and a buried oxide layer of 145 nm. The device layer is boron doped with a concentration of about 10^{15} cm^{-3}. The fabrication steps included [9]

1. Electron-beam lithography in positive resist to pattern the image of the NW and contact pads.
2. Aluminium mask e-beam vapour deposition.
3. Anisotropic reactive ion etching of the device layer through the Al mask and mask removal.
4. Magnetron sputtering of titanium electrodes and their isolation with silica to allow measurements in liquids.

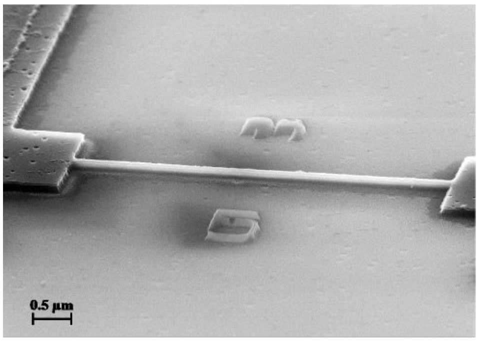

Figure 1: SEM image of the nanowire and the contact pads. The length of the nanowire is 5 µm, the width is 100 nm.

Both optical and electron-beam lithography was used to pattern electrodes and for isolation. The thickness of the Ti and SiO_2 layers was 50 and 200 nm, respectively. Schottky barriers are formed between silicon contact pads and Ti electrodes. Fabricated transistors were studied in air and in buffer solutions with different pH values. The sensitivity of a semiconductor sensor strongly depends on the charge carrier density, which can be changed by the gate voltage V_g applied to the SOI handle layer. During pH measurements, the liquid itself serves as a second gate with a voltage V_{ref}. The measured transistor characteristics were strongly asymmetric. The hole conductivity of the transistor was very low down to gate voltages of $V_g = -10$ V. For positive voltages at the gate (when an inverse electron channel formed), typical *I*–*V*-curves with ohmic and saturation regions were measured. Such characteristic asymmetry is induced by a Schottky barrier. Its height is different for electrons and holes [10]. For p-type silicon (p-Si) with a doping level of about 10^{15} cm^{-3} and Ti electrodes, the barrier height for holes is about three times higher than for electrons. Measurements of the pH sensitivity of the transistor were carried out at positive voltages V_g at the gate. The measurements were carried out by applying fixed source–drain and source–gate voltages $V_{sd} = -0.5$ V and $V_g = 8$ V, respectively, and measuring the resulting transport current. The inversion channel that forms under these conditions in p-Si is optimal for pH measurements in liquids [11]. An AgCl electrode dipped in a buffer solution was used as a reference electrode. The pH measurements were carried out statically in droplets without a flux of liquid. Large amounts of buffer solution with the target pH were pumped through the droplet volume to change the pH level.

In Figure 2 the transport current of the SiNW FET at different pH values of the buffer solution and at different reference-electrode potentials is shown.

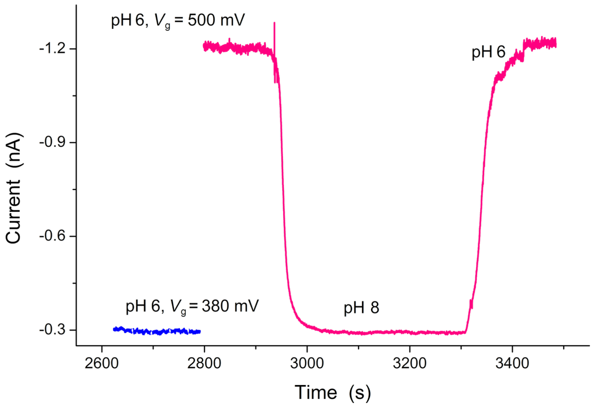

Figure 2: SiNW FET response to the change of the pH value of the buffer solution.

One can see that the current level for a transistor in buffer solution at pH 8 and $V_{\mathrm{ref}} = 0.5$ V coincides with the current for a buffer solution at pH 6 and $V_{\mathrm{ref}} = 0.38$ V. Accordingly, the pH sensitivity of the SiNW FET (i.e., the change of the insulator–electrolyte potential, Ψ_0, to a change of the bulk pH [12]) can be estimated as:

$$\frac{\delta\Psi_0}{\delta\mathrm{pH}} = \frac{\Delta V_{\mathrm{ref}}}{\Delta\mathrm{pH}} \approx 59\ \mathrm{mV/pH}\,. \tag{1}$$

This is an extremely high value for an ion-sensitive FET (ISFET) with silica as a gate dielectric. It is comparable with the sensitivity of ISFETs with special gate dielectrics such as Ta_2O_5. Moreover this sensitivity is comparable to the theoretical limitation at room temperature [12].

Field/charge sensors are traditionally characterized by a maximum charge sensitivity. To estimate this, we measured the NW FET conductivity dependence on the charge at the surface of the NW native oxide layer and calculated the spectral density of transport current fluctuations. We used linearised Poisson–Boltzmann equations to define the electrical potential in the NW and in the electrolyte together with the Poisson equation for the electrical potential in the NW oxide layer. The exact solution of this three-layer problem, as opposed to the estimations of Gao et al. [13], allows us to explore the potential profile explicitly. A linearisation of the Poisson–Boltzmann equations is possible in the case of weak potentials applied to the reference electrode and a small bending of semiconductor bands, so that $|e\varphi_{\mathrm{s/ox}}|,|e\varphi_{\mathrm{ox/el}}| < k_{\mathrm{B}}T$, where $\varphi_{\mathrm{s/ox}}$ and $\varphi_{\mathrm{ox/el}}$ are the potentials at the nanowire–oxide and oxide–electrolyte boundaries, respectively, k_{B} is the Boltzmann constant and T is the temperature. Numerical methods used by several authors previously [11,14-16] for solving the Poisson–Boltzmann equation do not allows one to clearly demonstrate the behaviour of the studied system in different modes.

In our calculations we assumed the absence of charges inside the oxide layer and a uniformity of the dopant density in the NW as in [13]. Moreover, we assumed that the electric field, which is directed normally to the NW surface, is much larger than the longitudinal one so that the latter does not influence the modulation of the NW conductivity [11]. This assumption is correct because the NW length is much larger than its lateral dimensions and the voltage at the contacts is low. As in previous reports [11,13,14], we assumed that electrolyte ions can come directly to the oxide layer surface. Using a cylindrical coordinate system $\boldsymbol{r} = \boldsymbol{r}(\rho, \alpha, z)$ with the z axis directed along the NW axis, the equations become [17]

$$\left(\nabla^2 - \lambda_1^{-2}\right)\varphi_1(\boldsymbol{r}) = 0\,, \tag{2}$$

$$-\nabla\left(\varepsilon_2\nabla\varphi_2(\boldsymbol{r})\right) = 0\,, \tag{3}$$

$$\left(\nabla^2 - \lambda_3^{-2}\right)\varphi_3(\boldsymbol{r}) = 0\,, \tag{4}$$

where φ_1, φ_2, and φ_3 are the potentials in the nanowire, oxide layer, and electrolyte, respectively (regions 1, 2, 3). The parameters λ_1 and λ_3 are the Debye lengths of screening in the NW and electrolyte, respectively. The boundary conditions of the problem are the equality of the potentials and electric displacement fields at the nanowire–oxide interface and the equality of the leap in potentials and electric-displacement fields due to charges at the oxide–electrolyte interface. The potential at infinity approaches zero. Taking into account the axial symmetry of the nanowire, we obtain as the solution for the potential inside the nanowire

$$\varphi_1(\rho) = -4\pi\sigma\frac{I_0(\rho/\lambda_1)}{I_0(\rho_1/\lambda_1)}C^{-1}\,, \tag{5}$$

where σ is the surface charge density at the oxide–electrolyte interface, ρ_1 is the nanowire radius, I_0 the modified Bessel function of the first kind to zeroth order, and C is the off-diagonal coefficient of the capacitance matrix [18] that is responsible for the change in potential at the nanowire–oxide interface due to the variation in surface charge density at the oxide–electrolyte interface. This capacitance is defined by geometrical and electrical parameters of the system:

$$C = \frac{\varepsilon_1}{\lambda_1}J\frac{\rho_1}{\rho_2} + \frac{\varepsilon_3}{\lambda_3}K + \frac{\varepsilon_1\varepsilon_3\rho_1}{\varepsilon_2\lambda_1\lambda_3}JK\ln\left(\frac{\rho_2}{\rho_1}\right), \tag{6}$$

where ε_1, ε_2, and ε_3 are the relative permittivities in regions 1, 2, and 3, respectively, $\rho_2 = \rho_1 + \delta\rho$ with $\delta\rho$ being the oxide-layer thickness, and

$$J = \frac{I_1(\rho_1/\lambda_1)}{I_0(\rho_1/\lambda_1)}\,, \quad K = \frac{K_1(\rho_2/\lambda_3)}{K_0(\rho_2/\lambda_3)}\,,$$

where $I_{0,1}$ and $K_{0,1}$ are modified Bessel functions of the first and second kind, respectively.

In Equation 6, the two first terms are responsible for the capacitance of the NW and electrolyte. It is seen that for $\rho_1 \approx \rho_2$ the last term in Equation 6 becomes a product of the two first term multiplied by $\approx\delta\rho/\varepsilon_2$ and is responsible for the oxide layer. With real coefficient values substituted in Equation 6, the second term becomes 10 times greater than the first one. The response of the NW FET to the variation of surface charge can be found by inserting Equation 5 in the equation for the relative NW conductivity modulation [17]

$$\frac{\Delta G}{G_0} = e^{-\beta\Delta\varphi_1} - 1\,, \tag{7}$$

where $\beta = e/k_BT$. The linearisation of Equation 7 by $\Delta\varphi_1$ (such that $\Delta G/G_0 \approx -\beta\int\varphi_1 dV/V$, where V is the NW volume) allows one to obtain a simple expression for the response of the transistor in the linear mode:

$$\frac{\Delta G}{G_0} \approx 8\pi\sigma\beta\frac{\lambda_1}{\rho_1}JC^{-1}\,. \tag{8}$$

Under transition to the subthreshold mode, the concentration of charge carriers in the NW decreases by orders of magnitude and the screening length in the NW, λ_1, increases accordingly. Simultaneously, the dependence of the potential on the coordinate in Equation 5 disappears ($I_0(x) \approx 1$, $x \to 0$), the NW capacitance decreases and only the second term remains in Equation 6 ($\lambda_1 >> \rho_1$, $J \to \rho_1/2\lambda_1$) so that the potential in the NW does not depend on the electrical parameters of the NW and the oxide layer:

$$\varphi_{1s-th} \approx -4\pi\sigma\left(\frac{\varepsilon_3}{\lambda_3}K\right)^{-1}\,. \tag{9}$$

The product in the brackets of Equation 9, which corresponds to Equation 6, is the self-capacitance of the studied system in the subthreshold mode. This capacitance coincides with the capacitance of the electrolyte double-layer. This result corresponds to the expression for the full capacitance of the system from [13] for the considered mode. To estimate the NW FET response in subthreshold mode, one should substitute Equation 9 into Equation 7. It should be noted that the response of the transistor to variation of the surface charge density in this mode is exponential [17]. Considering the estimation for the mobility of charge carriers in the inversion channel from [10] for our measurements (Figure 2) we get $\lambda_1 >> \rho_I$, so our approximation in Equation 9 is appropriate in this case. Using Equation 9, we get an estimation of the charge variation at the NW surface $\Delta Q \approx 5 \times 10^4\, e$ for a change of the pH value from 8 to 6. This value is one order of magnitude larger than the one in the report of Gao et al. [13]. The difference can be explained by the NW surface area. In our case the NW radius was ≈100 nm, while in Gao's case [13] it was only 5 nm. Moreover, the pH sensitivity of our sample is two times higher.

In the case of the application of NW FET to biosensors it is necessary to consider the large dimensions of the molecules. The detected charge will be located not on the surface but in the electrolyte double-layer. This region can be modeled [19] as an ion-permeable membrane with the accordingly changed Poisson–Boltzmann equation for it. While the exact solution of this problem can be found by numerical methods, one often resorts to a simplified model [20], which qualitatively correctly describes the system under study. To take into account the dipole moment of the detected molecules one should reformulate the boundary conditions [14] by adding the leap of the potential at the oxide–electrolyte interface. This will lead to the following correction of Equation 6:

$$C_{\text{bio}} = C\left(1 + \varepsilon_3\frac{l_{\text{bio}}}{\lambda_3}K\right), \tag{10}$$

where l_{bio} is the effective thickness of the layer, and the dipole moment can be represented by $\tau_{\text{bio}} = \sigma l_{\text{bio}}$.

The charge sensitivity of the NW FET is

$$\delta Q = \frac{\sqrt{S_I * \Delta f}}{\{\delta I/\delta Q\}}\,, \tag{11}$$

here S_I is the spectral density of the NW current fluctuations, Δf is the output frequency band of the device and is assumed to be 1 Hz, $\delta I/\delta Q$ is the NW current response on the surface–charge variation. In general, the spectral density of current fluctuations S_I is determined by noncoherent contributions of the substrate and electrolyte noise and intrinsic current fluctuations of the NW FET [21]. It was shown [22] experimentally that the fluctuation of electrolyte ions can be neglected. The substrate noise is $1/f$ noise and it is important to take it into account in a direct low-frequency readout from the NW FET [21,22]. However, the $1/f$-noise intensity rapidly decreases with the readout frequency increasing and it plateaus out at $f \approx 2$ kHz in [5] or $f \approx 80$ Hz in [21]. Therefore the lock-in technique [5] and the correlation analysis (simultaneous measurement by several equal devices) that we used allow us to eliminate $1/f$-noise. Thus, the maximum NW FET sensitivity is defined by the frequency-independent component of the spectral density S_I.

The spectral density of NW current fluctuations at an angular frequency $\omega = 2\pi f$, so that $\hbar\omega << k_BT$, is determined by the thermal fluctuation $S_{In} = 4k_BTG$. The spectral density of current fluctuations at Schottky barriers formed at contact regions is described by [23] as $S_{\mathrm{IB}} = (2eV/R_{\mathrm{B}}) \coth (eV/2k_{\mathrm{B}}T_{\mathrm{B}})$, where T_{B} is the temperature of the barrier, R_{B} is the barrier resistance, and V the voltage drop across it. At $eV \ll k_{\mathrm{B}}T_{\mathrm{B}}$ this equation turns into the thermal fluctuation equation $S_{\mathrm{IB}} = 4k_{\mathrm{B}}T/R_{\mathrm{B}}$; at $eV \gg k_{\mathrm{B}}T$, it turns into shot noise equation $S_{\mathrm{IB}} = 2eI$. Since the distance between the NW and the Schottky barriers in our design is about several microns, which is far larger than the phase-breaking length [24], current fluctuations in the NW and in the Schottky barrier were uncorrelated. According to this, one can calculate the spectral density of the transport-current fluctuations S_{I} by considering an equivalent scheme with a series connection of resistors modelling NW and Schottky barriers with uncorrelated fluctuation generators:

$$S_{\mathrm{I}} = \frac{S_{\mathrm{I,n}} \cdot R^2 + S_{\mathrm{IB}} \cdot R_{\mathrm{B}}^2}{(R + R_{\mathrm{B}})^2}. \tag{12}$$

Our four-probe measurements of the NW resistance R and Schottky barrier resistance R_{B} at room temperature show that $R \gg R_{\mathrm{B}} \approx 1$ kΩ (applied voltage $V_{\mathrm{d}} = 0.5$ V). Rough estimates at the values of the parameters show that the spectral density of the current fluctuations at the Schottky barriers is described by the thermal-fluctuation equation and its contribution to S_{I} in Equation 12 is negligibly small in comparison with the NW current fluctuations. Considering this, from Equation 11 and Equation 12 it follows that the charge sensitivity of NW FET is

$$\delta Q \approx \frac{\Xi}{I}\sqrt{\frac{4k_{\mathrm{B}}T}{R}}, \tag{13}$$

where $\Xi = \rho_2 L K \varepsilon_3 / 2\beta\lambda_3$, L is the NW length, and I the direct current through the barriers. As opposed to the respective expression in [5] there is no shot-noise contribution proportional to the current in our estimation of the fluctuation. The derived Equation 13 is more correct since it is known [24] that in diffused resistors shot noise does not sum up to the thermal fluctuation and exists only for resistors of small size at low temperature. Equation 13 gives an estimation of the maximum NW FET charge-sensitivity in subthreshold mode $\delta Q \approx 5 \times 10^{-3} e/\sqrt{\mathrm{Hz}}$ for our measurements. This derived value is better than the results obtained in [13], which can be explained by a better pH sensitivity of our transistor.

Conclusion

In this work we demonstrated experimentally the possibility of the fabrication of a highly sensitive pH sensor and charge sensor based on NW FET made from SOI using traditional semiconductor technology. The conducted analysis of the model allows us to estimate the value of the NW relative-conductivity modulation due to the variation of the charge density on the oxide–electrolyte interface as well as the variation of this charge density due to the pH variation for a known pH sensitivity of the NW FET. The calculated maximum charge sensitivity in subthreshold mode is estimated to be $5 \times 10^{-3} e/\sqrt{\mathrm{Hz}}$. The pH sensitivity of our experimental samples is close to the theoretical limit of 59 mV/pH and is not inferior to VLS-grown nanowires [7,13]. It was shown that the simplified fabrication technology with Schottky barriers in contact regions allows one to avoid processes of doping and dopant activation and has no effect on the NW transport-current fluctuation density.

Acknowledgements

We wish to acknowledge M. Yu. Kupriyanov and A. V. Semenov for helpful discussions of the problem. The work is partly sponsored by grants from the Russian Foundation for Basic Research (11-02-12122-ofi-m-2011, 11-07-00748) and Ministry of education and science of Russia (GK 16.513.11.3063).

References

1. Patolsky, F.; Zheng, G.; Lieber, C. M. *Anal. Chem.* **2006,** *78,* 4260–4269. doi:10.1021/ac069419j
2. Penner, R. M. *Annu. Rev. Anal. Chem.* **2012,** *5,* 461–485. doi:10.1146/annurev-anchem-062011-143007
3. Waclawik, E. R.; Chang, J.; Ponzoni, A.; Concina, I.; Zappa, D.; Comini, E.; Motta, N.; Faglia, G.; Sberveglieri, G. *Beilstein J. Nanotechnol.* **2012,** *3,* 368–377. doi:10.3762/bjnano.3.43
4. Naumova, O. V.; Fomin, B. I.; Nasimov, D. A.; Dudchenko, N. V.; Devyatova, S. F.; Zhanaev, E. D.; Popov, V. P.; Latyshev, A. V.; Aseev, A. L.; Ivanov, Yu. D.; Archakov, A. I. *Semicond. Sci. Technol.* **2010,** *25,* 055004. doi:10.1088/0268-1242/25/5/055004
5. Salfi, J.; Savelyev, I. G.; Blumin, M.; Nair, S. V.; Ruda, H. E. *Nat. Nanotechnol.* **2010,** *5,* 737–741. doi:10.1038/nnano.2010.180
6. Brenning, H.; Kafanov, S.; Duty, T.; Kubatkin, S. I.; Delsing, P. *J. Appl. Phys.* **2006,** *100,* 114321. doi:10.1063/1.2388134
7. Tian, B.; Cohen-Karni, T.; Qing, Q.; Duan, X.; Xie, P.; Lieber, C. M. *Science* **2010,** *329,* 830–834. doi:10.1126/science.1192033
8. Soloviev, I. I.; Devyatov, I. A.; Krutitskiy, P. A.; Amitonov, S. V.; Presnov, D. E.; Krupenin, V. A. Experimental and theoretical study of nanowire FET based on SOI. In *International Conference “Micro- and Nanoelectronics–2012” Book of Abstracts,* 2012; P1–P41.
9. Presnov, D. E.; Amitonov, S. V.; Krupenin, V. A. *Russ. Microelectron.* **2012,** *41,* 310–313. doi:10.1134/S1063739712050034
10. Koo, S.-M.; Edelstein, M. D.; Li, Q.; Richter, C. A.; Vogel, E. M. *Nanotechnology* **2005,** *16,* 1482. doi:10.1088/0957-4484/16/9/011
11. Nair, P. R.; Alam, M. A. *IEEE Trans. Electron Devices* **2007,** *54,* 3400–3408. doi:10.1109/TED.2007.909059
12. van Hal, R. E. G.; Eijkel, J. C. T.; Bergveld, P. *Sens. Actuators, B* **1995,** *24,* 201–205. doi:10.1016/0925-4005(95)85043-0
13. Gao, X. P. A.; Zheng, G.; Lieber, C. M. *Nano Lett.* **2009,** *10,* 547–552. doi:10.1021/nl9034219

14. Windbacher, T.; Sverdlov, V.; Selberherr, S.; Heitzinger, C.; Mauser, N.; Ringhofer, C. Simulation of Field-Effect Biosensors (BioFETs). In *International Conference on Simulation of Semiconductor Processes and Devices, SISPAD 2008*; pp 193–196.
15. Heitzinger, C.; Kennel, R.; Klimeck, G.; Mauser, N.; McLennan, M.; Ringhofer, C. *J. Phys.: Conf. Ser.* **2008,** *107,* 012004. doi:10.1088/1742-6596/107/1/012004
16. Ringhofer, C.; Heitzinger, C. *ECS Trans.* **2008,** *14,* 11–19. doi:10.1149/1.2956012
17. Sze, S. M.; Ng, K. K. *Physics of semiconductor devices;* Wiley-Interscience: Hoboken, NJ, USA, 2007.
18. Maxwell, J. C. *A treatise on electricity, magnetism;* Clarendon Press: Wotton-under-Edge, Gloucestershire, UK, 1873.
19. Landheer, D.; Aers, G.; McKinnon, W. R.; Deen, M. J.; Ranuarez, J. C. *J. Appl. Phys.* **2005,** *98,* 044701. doi:10.1063/1.2008354
20. Shinwari, M. W.; Deen, M. J.; Landheer, D. *Microelectron. Reliab.* **2007,** *47,* 2025–2057. doi:10.1016/j.microrel.2006.10.003
21. Clément, N.; Nishiguchi, K.; Dufreche, J. F.; Guerin, D.; Fujiwara, A.; Vuillaume, D. *Appl. Phys. Lett.* **2011,** *98,* 014104. doi:10.1063/1.3535958
22. Rajan, N. K.; Routenberg, D. A.; Reed, M. A. *Appl. Phys. Lett.* **2011,** *98,* 264107. doi:10.1063/1.3608155
23. Rogovin, D.; Scalapino, D. J. *Ann. Phys. (Amsterdam, Neth.)* **1974,** *86,* 1–90. doi:10.1016/0003-4916(74)90430-8
24. Steinbach, A. H.; Martinis, J. M.; Devoret, M. H. *Phys. Rev. Lett.* **1996,** *76,* 3806–3809. doi:10.1103/PhysRevLett.76.3806

License and Terms

The definitive version of this article is the electronic one which can be found at:
doi:10.3762/bjnano.4.38

Beilstein Journal
of Nanotechnology

Template based precursor route for the synthesis of $CuInSe_2$ nanorod arrays for potential solar cell applications

Mikhail Pashchanka, Jonas Bang‡, Niklas S. A. Gora‡, Ildiko Balog,
Rudolf C. Hoffmann and Jörg J. Schneider*§

Full Research Paper

Open Access

Address:
Fachbereich Chemie, Eduard-Zintl-Institut, Fachgebiet Anorganische
Chemie, Technische Universität Darmstadt, Petersenstraße 18,
64287 Darmstadt, Germany

Email:
Jörg J. Schneider* - joerg.schneider@ac.chemie.tu-darmstadt.de

* Corresponding author ‡ Equal contributors
§ Fax: +49 6151 163470; Tel: +49 6151 163225

Keywords:
CIS; light absorption; nanocasting; nanorod arrays; precursor
synthesis

Beilstein J. Nanotechnol. **2013,** *4,* 868–874.
doi:10.3762/bjnano.4.98

Received: 28 August 2013
Accepted: 01 December 2013
Published: 10 December 2013

This article is part of the Thematic Series "Nanostructures for sensors, electronics, energy and environment".

Guest Editor: N. Motta

Abstract

Polycrystalline $CuInSe_2$ (CISe) nanorods are promising for the fabrication of highly efficient active layers in solar cells. In this work we report on a nanocasting approach, which uses track-etched polycarbonate films as hard templates for obtaining three-dimensionally (3D) arranged CISe nanorod arrays. Copper and indium ketoacidoximato complexes and selenourea were employed as molecular precursors. Arrays of parallel isolated cylindrical pores of 100 nm nominal diameter and 5 µm length were used for the infiltration of the precursor solution under inert atmosphere, followed by drying, thermal conversion into a preceramic ‘green body’, a subsequent dissolution of the template, and a final thermal treatment at 450 °C. The nanorods that where synthesised in this way have dimensions equal to the pore sizes of the template. Investigation of the $CuInSe_2$ nanorod samples by spectroscopic and diffraction methods confirmed a high purity and crystallinity, and a stoichiometric composition of the CISe ternary semiconductor compound.

Introduction

Polycrystalline heterojunction solar cells with a columnar morphology of the photovoltaic active layer that are based on the chalcopyrite compound $CuInSe_2$ (CISe) have been intensively studied [1]. The basic advantages of $CuInSe_2$ as a light absorbing material are its high photovoltaic efficiency and the stability of its properties over time. Apparently, the conversion efficiency can be improved by the increase of the effective absorbing area, and this gave rise to the study of thin film solar cells that are composed of finely divided nanocrystals [2,3]. In this respect, quasi one dimensional (Q1D) nanostructures, such as nanorods and nanowires, have received considerable interest because of their unique ability for independent adjustment of light absorption (by nanowire length) and charge separation (by nanowire diameter). Nanowire-based photovoltaic layers will allow the fabrication of low-cost small size energy devices with economical use of materials. Very recently, Schoen et al. reported the VLS synthesis of $CuInSe_2$ nanowires (by Cu impregnation of In_2Se_3 nanowires) and the construction of a single-nanowire CIS/CdS core–shell device [4]. However, the authors estimated the efficiency of their solar cell to be below 1%, and the construction of a larger scale device with this approach still remains questionable. Earlier, template-based solution precursor routes were demonstrated to be useful as a fully controllable, simple and inexpensive alternative to vacuum techniques that operate in the VLS growth mode. Large arrays of vertically aligned CISe nanowires were fabricated by electrodeposition into porous alumina templates [5,6]. The nanowires were composed of 5 nm grains and had a noticeable spread in diameter values (10–30 or 25–40 nm, depending on the pore size of the used template) and lengths (0.6–5 μm). Interestingly, authors reported a preferential growth in the [112] direction, whereas the template-based method is commonly known for producing nanowires that are composed of smaller and randomly oriented crystal units [7]. In a similar work, Hernández-Pagán et al. switched between p-type Cu-rich and n-type In-rich CISe by changing the electrodeposition potential [8]. Thus, they indirectly confirmed the flexibility of the solution route in preparation of semiconductors with controlled elemental composition.

We recently successfully demonstrated electroless deposition of molecular precursors (Cu- and In-oximato complexes and thiourea) into track-etched polycarbonate templates and the synthesis of stoichiometric ternary $CuInS_2$ nanorod arrays [9]. In the present work, we extend our method to the photochemically even more active $CuInSe_2$ material and demonstrate the synthesis of uniform polycrystalline $CuInSe_2$ nanorod arrays. Selenourea was used as a Se source analogous to thiourea in our previous investigation. The facile precursor method provides many benefits over currently used selenization techniques [10-12], or the impregnation of a third metal cation into a binary selenide compound [4,13]. Firstly, it achieves mixing at the atomic level by forming a solid 'green body', in which the elements are present in the correct stoichiometry [14]. Secondly, the method allows to lower the conversion temperature and to reduce the particle size. Thus, the products usually contain small particles of large surface area, which is favourable for visible light absorption. Finally, the precursor solution route does not employ the highly toxic gaseous hydrogen selenide as a Se-source. However, suitable precursors are not always available for a desired functional material, but nevertheless there are already several reports on different single source molecular precursors for chalcopyrite type $CuInSe_2$ in the current literature [15-17]. It has to be mentioned that the morphologies accessible by the liquid precursor route are not restricted to only Q1D nanostructures. Such stable 'inks' can also find application in printable photovoltaics or film deposition onto various standard substrates, e.g., polycrystalline alumina, low-cost glass or even flexible polymeric films [18,19].

Experimental

In- and Cu-oximato complexes were synthesised as reported earlier and were used as metal cation sources [20,21]. A solution of Cu-oximato and In-oximato precursors, and selenourea in 1:1:3 molar ratio was prepared in 2-methoxyethanol under inert atmosphere (all steps employing selenourea were performed in an Ar glovebox). It was found during our previous study on the ternary $CuInS_2$ system that the stoichiometric 1:1:2 molar ratio of molecular precursors in the solution yields chalcogen-deficient products with a minor content of secondary phases, which can be completely avoided by providing an excess of the chalcogen-containing component [9]. Hence, excess selenourea (1.5 times) was taken for the present work. After adding the solvent to the mixture of precursor powders, the solution gains an intensive dark-brown colour. A porous polycarbonate film (Whatman Nuclepore™ track-etch membrane, nominal pore size 0.1 μm) was immersed into the solution, ultrasonicated for 5 min for gas removal and complete pore infiltration (in a sealed flask under inert gas), and dried at ambient temperature (in the glovebox). After that, the membranes were cleaned from the excess of precursors with a lint-free tissue. The first solidification step of the nanorods (formation of 'green body') was performed in a quartz tube under Ar flow at 180 °C for 2 h. The filled templates were then immersed in CH_2Cl_2 to remove the polymeric film completely and the obtained powder was dried in air (the solidified green body nanorods were stable in the air conditions). Finally, the dry solid residue was placed in a quartz tube under Ar flow at 450 °C for another 2 h. The temperature at this stage should not exceed 450 °C, since a brick-red deposit (poly-selenide) covered the colder parts of the quartz tube outside the furnace (the entire process is shown in Scheme 1).

The final ceramic $CuInSe_2$ nanowires had a deep black colour. The samples were characterised by scanning electron microscopy (SEM) by using a Philips XL-30 FEG electron-scan microscope coupled with an energy-dispersive X-ray (EDX) analyser that was operated at 20–25 kV. The samples were mounted on conductive carbon-rich polymer films and sputtered with a Pt/Pd alloy. Transmission electron microscopy (TEM) images were taken by using a Tecnai G2 F20 microscope operated at 200 kV, the samples were dispersed in

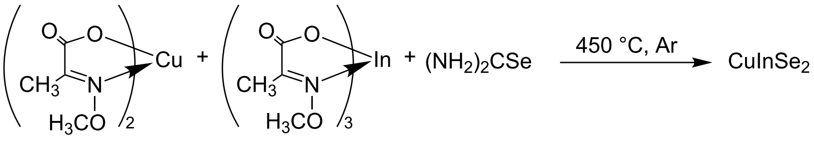

Scheme 1: Reaction scheme of the ternary $CuInSe_2$ compound obtained by the precursor synthesis method employing Cu(II) and In(III) oximato complexes.

ethanol by ultrasonication and then deposited on copper TEM grids. X-ray analysis (XRD) of the species was carried out on a Stoe&Cie StadiP diffractometer in Debye–Scherrer geometry while using Cu Kα_1 radiation (λ = 1.541 Å) with a Ge(111) monochromator. Raman spectra were recorded from 50 to 2000 cm^{-1} with a micro-Raman HR800 spectrometer (Horiba Jobin Yvon, Bensheim, Germany) while using laser wavelength of 514 nm. For the recording of absorption spectra the remission method was used. With a UV–vis–NIR spectrometer Lambda 900 from Perkin Elmer the remission was recorded and automatically converted to an absorption spectrum via the Kubelka–Munk-relation ($(1-R)^2/(2R)$, R is the normalized remission).

Results and Discussion

The morphology of the material after the final conversion step was examined by using SEM (Figure 1). The product consisted of separated parallel nanorod bundles. The nanorod diameter was about 100 nm and the length 5 µm, which is in full agreement with the pore sizes of the utilized polycarbonate templates.

The material demonstrated good stability after calcination at 450 °C, all nanorods had a smooth surface and uniform length and showed no cracks along the rod length. The EDX-analysis (Figure 2) showed a high purity of the product, as well as a homogeneous distribution and nearly ideal stoichiometric ratio of the constituting elements. According to the standardless

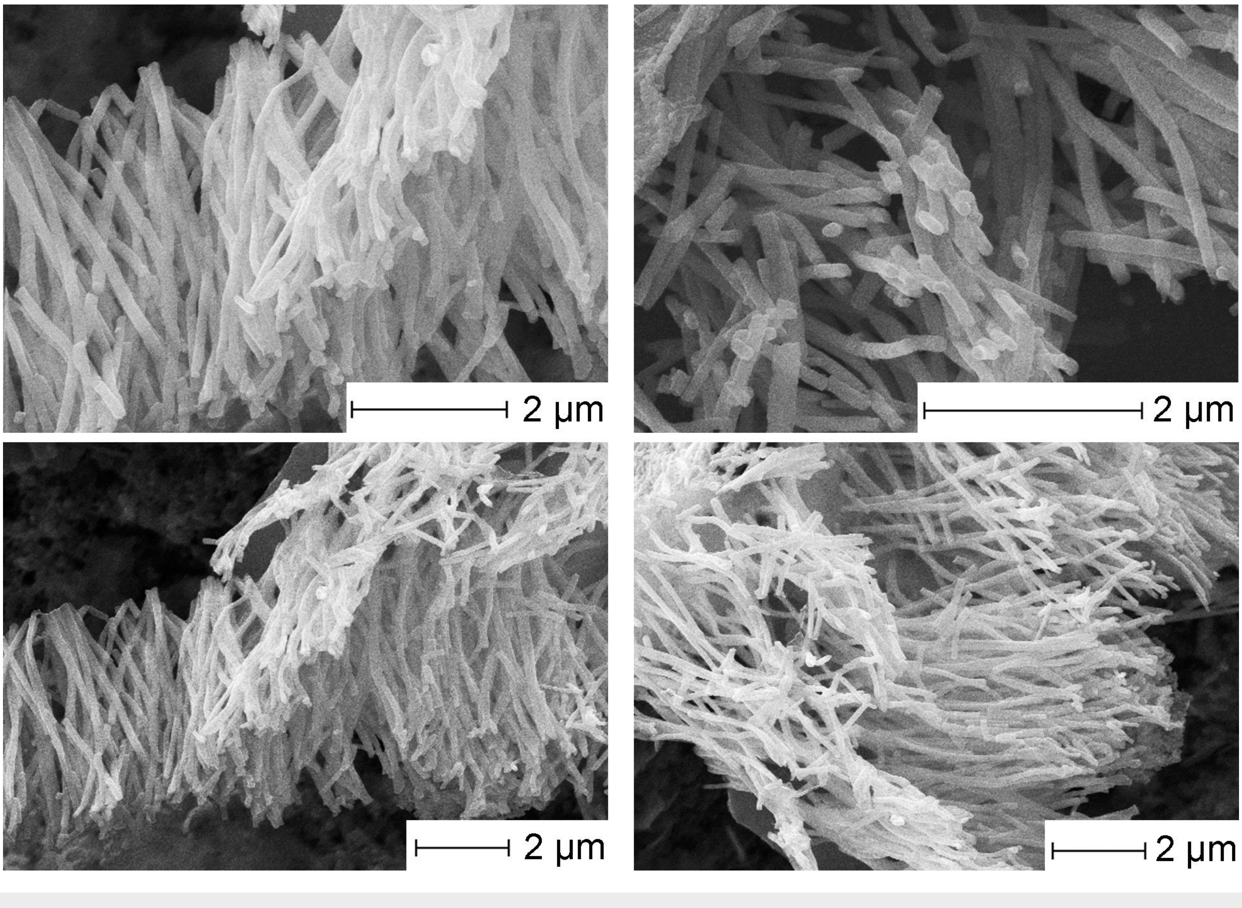

Figure 1: SEM micrographs of $CuInSe_2$ nanorod arrays after the final conversion step at 450 °C.

quantification method, the nanorods contain 19.0 wt % of Cu, 36.5 wt % of In, and 44.5 wt % of Se (the theoretical contents are 18.9, 34.1, and 47.0 wt %, correspondingly). The deviation from theoretically calculated values towards indium enriched $CuInSe_2$ is practically within the limits of the error of the individual method. The atomic Cu:In ratio is approximately 0.95, and the measured selenium deficiency is only around 2 at %.

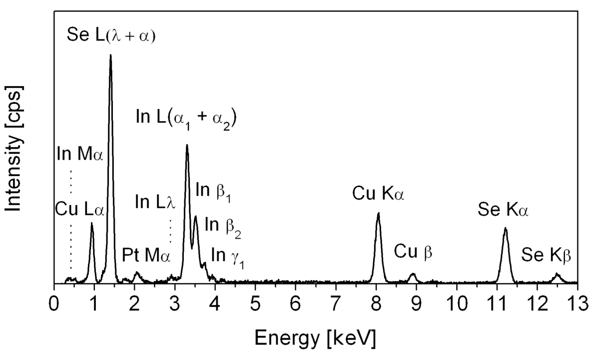

Figure 2: EDX analysis of $CuInSe_2$ nanorod arrays; Pt-signal originates from the sputtered Pt/Pd alloy.

Thus, if the formation of secondary phases occurs, only minor concentrations of indium selenide binaries are possible, which nevertheless has to be confirmed by other analysis methods. The purity of the sample was thus further characterised by powder X-ray diffractometry. The XRD analysis (Figure 3) demonstrated no secondary selenide phases or other impurities in the crystalline product. All of the reflections correspond solely to copper indium selenide (JCPDS-file 80-535). All signals are visibly broadened, which is due to the nanocrystallinity of the particles that compose the rod morphology. The mean crystallite size calculated from the most intense (112) peak by using the Scherrer equation is about 30 nm, which is approximately three times smaller than the nanorod diameter.

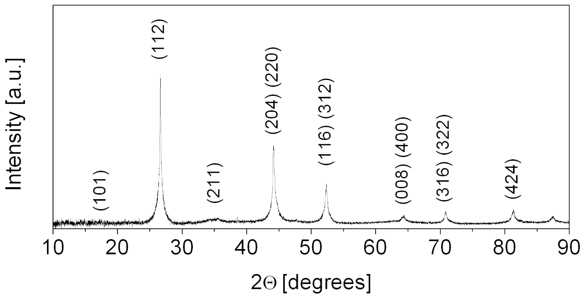

Figure 3: Powder X-ray diffraction pattern of polycrystalline $CuInSe_2$ nanorods after final conversion at 450 °C.

The polycrystalline nature of the product was also confirmed by TEM and SAED (Figure 4). Diffuse rings in the electron diffraction pattern (see inset in the upper left corner in Figure 4) suggest a random crystallite orientation and no preferential crystal growth direction. At a higher magnification it can be recognized that the rods are composed of nanocrystals of approximately 5–10 nm in size, which is in contrast to the determined mean crystallite size as obtained from the Scherrer equation. However, it can be seen that if one moves across an individual rod, the individual crystallites mostly overlap, thus their exact individual size cannot be determined. Possibly, smaller crystallites are distributed at the surface, and a crystal size enlargement takes place near the rod core, so that the average size equals to 30 nm. It has to be mentioned that the samples for TEM/SAED were dispersed in ethanol by ultrasonication before their deposition onto a copper grid, hence, the nanorod bundles can be partially disassemble and individual nanorods unhinge from the structures.

The phase and purity of the $CuInSe_2$ material were further confirmed by Raman scattering (a typical micro Raman spectrum is presented in Figure 5). Copper indium selenide is characterised by a large absorption coefficient, and incident light can reach penetration depths only up to 100–200 nm, which results in a low signal intensity [22,23]. However, the penetration depth corresponds well with the nanorod diameter, and reliable information about the structural properties can be thus obtained. The most intensive peak at 172 cm^{-1} results from the Γ_1 chalcopyrite phonon mode (selenium anion vibration) [24]. This signal is commonly observed in $CuInSe_2$ thin films and nanoparticles, and its intensity is associated with the crystalline quality [25-27]. A moderate shift of this peak to lower wavenumbers may result from structural defects like grain boundaries, and confirms the nanocrystalline composition of the nanorods [27]. The broad structureless signal centred at 226 cm^{-1} is also in good agreement with previous studies of $CuInSe_2$ lattice dynamics (multiple signals in the range between 198 and 260 cm^{-1}) [24,28,29]. It is also important to note, that there are no prominent peaks with Raman shifts corresponding to secondary indium or copper selenides, which denotes a higher homogeneity of the material than can be achieved by selenisation of metallic precursors or the electrodeposition technique [11,23].

To characterize the light absorbing properties of nanorods, the UV–vis–NIR spectrometry was employed (Figure 6; note that the absorption is given in arbitrary units). The absorption starts in the UV region at λ = 210–220 nm and reaches the maximum at 395 nm. The maximal absorption covers practically the whole visible region and begins to decrease slowly at approximately 575–590 nm; a little broad peak is observed at 522–525 nm,

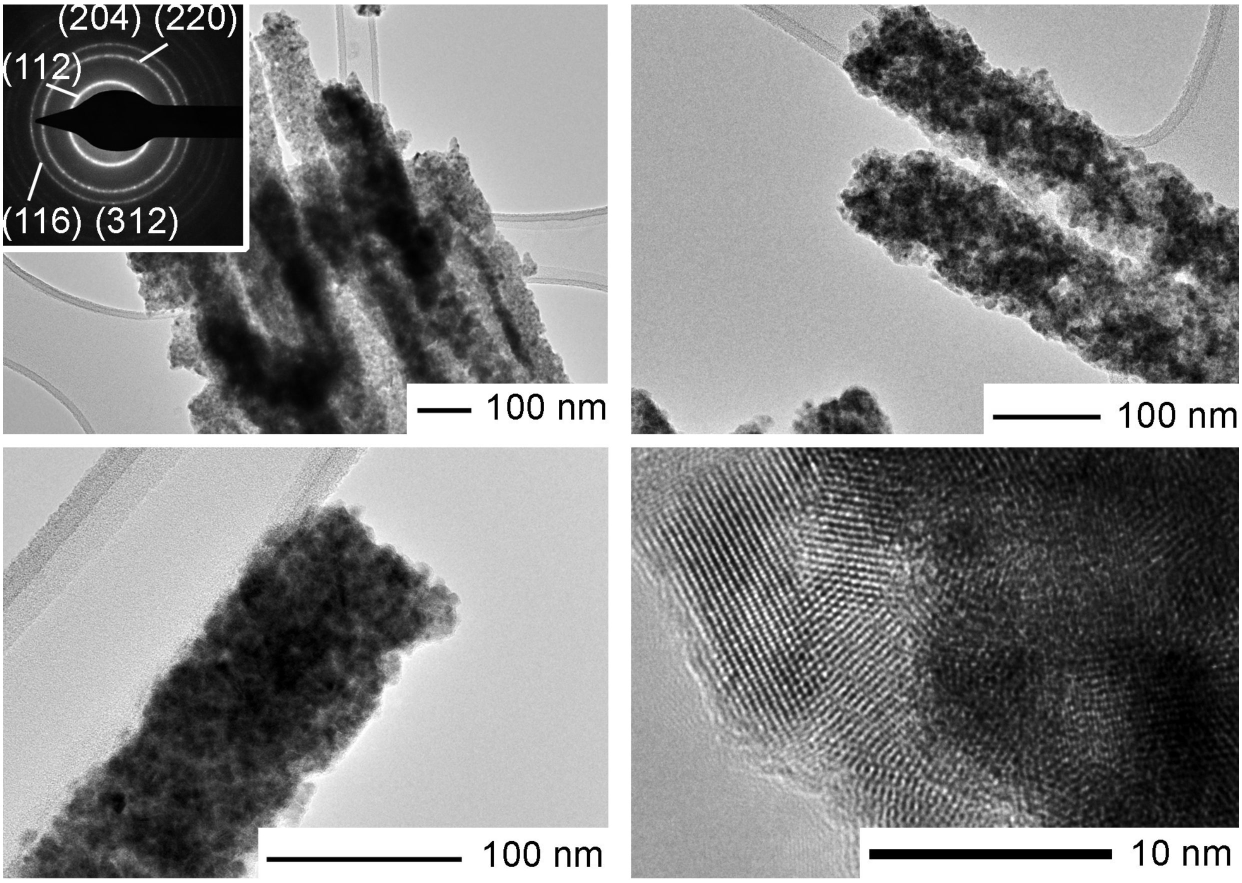

Figure 4: TEM images and SAED micrograph of polycrystalline $CuInSe_2$ nanorods.

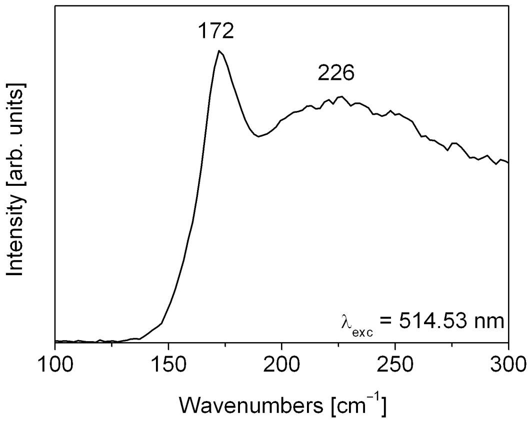

Figure 5: Raman spectrum of $CuInSe_2$ nanorod arrays.

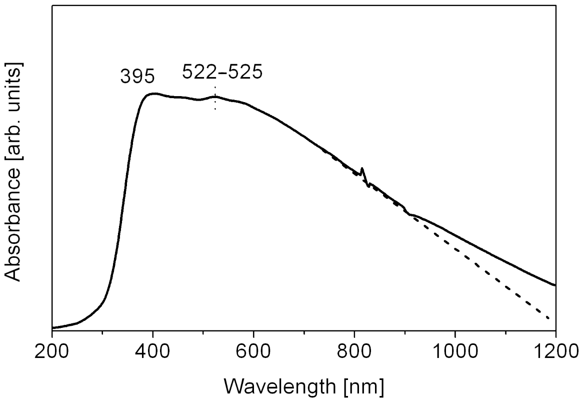

Figure 6: The absorption spectrum of polycrystalline $CuInSe_2$ nanorods.

which corresponds to 2.36–2.38 eV. The artifact between 800 and 900 nm is due to the grating change of the two monochromators, which has gratings for each the NIR- and for the UV–vis-range. Some distinctive features can be observed in comparison with earlier reports on nanostructured CISe materials. As a rule, $CuInSe_2$ CISe nanostructures of different shapes demonstrate a high absorption in the UV region, a maximum peak at 440–540 nm (which corresponds to a band gap of 2.8–2.3 eV) within the visible range, and the absorption spectrum threshold at around 550–900 nm [25,30,31]. In contrast to these examples, our material shows only a moderate absorption in the near ultraviolet region, and practically does not absorb at wavelengths of 200–300 nm. Instead, it shows superior performance compared to previously reported CISe nanomaterials in the whole visible region, with a remarkable value of absorption extending to the NIR region as well. This could be a benefit for a potential application in solar cells, since the amount of UV light is not constant during the course of the day. Distinctive in the spectrum in Figure 6 is the abnormally high threshold (where the dashed line in Figure 6 meets the wavelength axis); it surely goes beyond the range of measured wavelengths, but even at 1200 nm it would correspond to an absorption band gap of 1.03 eV, which perfectly matches the red edge of the solar spectrum (0.8–1.1 eV). The reason for this 'red shift' according to the previous reports on CISe nanostructures is not entirely clear, because the nanorods are composed of small 10–30 nm particles (as follows from the XRD and TEM analysis data). The UV–vis–NIR absorption results may count in favour of the mean crystallite size calculated by Scherrer formula (30 nm), and indirectly confirm that smaller 10 nm nanoparticles, which are visible in TEM images, are mainly distributed on nanorod surface and in the surface region.

Conclusions

In conclusion, we successfully synthesised aligned arrays of $CuInSe_2$, CISe, nanorods with controllable composition and high purity and homogeneity of the material. The CISe nanorods are composed of smaller randomly oriented nanocrystals of 30 nm mean size. As follows from the diffraction analysis and TEM examination, smaller 5–10 nm crystallites are mainly concentrated on the surface and in the surface region of the rods, while the rod core presumably consists of larger nanocrystals. The crystalline chalcopyrite phase was also confirmed by Raman spectroscopy, which suggested that there are no secondary binary selenides in the synthesised ternary compound. The light absorbing properties showed some distinctive characteristics in comparison with previously reported CISe nanomaterials; the nanorods moderately absorb in the near-UV region, and a good level of absorption covers the whole visible range and a part of the near infrared diapason as well (with a threshold that corresponds to a bandgap energy of 1.03 eV). A future challenge would be the incorporation of the 3D aligned CISe nanorod arrays as absorber material in a solar cell. Obviously, one of the main challenges towards this end is to achieve a transfer of the aligned nanorods onto a conductive substrate. A possible way to achieve that could be a direct placement of the polycarbonate template after infiltration with the precursor molecules onto a Mo-coated glass substrate, followed by thermal conversion into $CuInSe_2$ nanorod arrays. Another possibility could be a direct deposition of the as-prepared $CuInSe_2$ nanorods from dispersions in organic solvents directly onto the appropriate substrate. Both routes are currently studied in our laboratories.

Acknowledgements

TEM studies were done at the Ernst-Ruska Centre (ERC) Jülich under contract ERC-TUD1. We thank Dr. J. Engstler (TU Darmstadt) for measurements.

References

1. Mickelsen, R. A.; Chen, W. S.; Hsiao, Y. R.; Lowe, V. E. *IEEE Trans. Electron Devices* **1984,** *31,* 542–546. doi:10.1109/T-ED.1984.21566
2. Kar, M.; Agrawal, R.; Hillhouse, H. W. *J. Am. Chem. Soc.* **2011,** *133,* 17239–17247. doi:10.1021/ja204230d
3. de Kergommeaux, A.; Fiore, A.; Bruyant, N.; Chandezon, F.; Reiss, P.; Pron, A.; de Bettignies, R.; Faure-Vincent, J. *Sol. Energy Mater. Sol. Cells* **2011,** *95,* S39–S43. doi:10.1016/j.solmat.2010.12.054
4. Schoen, D. T.; Peng, H.; Cui, Y. *ACS Nano* **2013,** *7,* 3205–3211. doi:10.1021/nn3058533
5. Phok, S.; Rajaputra, S.; Singh, V. P. *Nanotechnology* **2007,** *18,* 475601. doi:10.1088/0957-4484/18/47/475601
6. Liu, P.; Singh, V. P.; Rajaputra, S.; Phok, S.; Chen, Z. *J. Mater. Res.* **2010,** *25,* 207–212. doi:10.1557/JMR.2010.0030
7. Cao, G. Z. *Nanostructures and Nanomaterials, Synthesis Properties and Applications;* Imperial College Press: London, 2004.
8. Hernández-Pagán, E. A.; Wang, W.; Mallouk, T. E. *ACS Nano* **2011,** *5,* 3237–3241. doi:10.1021/nn200373k
9. Pashchanka, M.; Hoffmann, R. C.; Schneider, J. J. *Eur. J. Inorg. Chem.* **2012,** 5621–5624. doi:10.1002/ejic.201200886
10. Moon, D. G.; Ahn, S.; Yun, J. H.; Cho, A.; Gwak, J.; Ahn, S.; Shin, K.; Yoon, K.; Lee, H.-D.; Pak, H.; Kwon, S. *Sol. Energy Mater. Sol. Cells* **2011,** *95,* 2786–2794. doi:10.1016/j.solmat.2011.05.028
11. Li, X.; Liu, W.; Jiang, G.; Wang, D.; Zhu, C. *Mater. Lett.* **2012,** *70,* 116–118. doi:10.1016/j.matlet.2011.11.110
12. Jiang, F.; Feng, J. *Thin Solid Films* **2006,** *515,* 1950–1955. doi:10.1016/j.tsf.2006.07.154
13. Kou, H.; Jiang, Y.; Li, J.; Yu, S.; Wang, C. *J. Mater. Chem.* **2012,** *22,* 1950–1956. doi:10.1039/c1jm14507j
14. Smart, L. E.; Moore, E. A. *Solid state chemistry: an introduction,* 4th ed.; CRC Press, Taylor and Francis Group: Boca Raton, 2012.
15. Castro, S. L.; Bailey, S. G.; Raffaelle, R. P.; Banger, K. K.; Hepp, A. F. *Chem. Mater.* **2003,** *15,* 3142–3147. doi:10.1021/cm034161o
16. Malik, M. A.; O'Brien, P.; Revaprasadu, N. *Adv. Mater.* **1999,** *11,* 1441–1444. doi:10.1002/(SICI)1521-4095(199912)11:17<1441::AID-ADMA1441>3.0.CO;2-Z
17. Banger, K. K.; Jin, M. H.-C.; Harris, J. D.; Fanwick, P. E.; Hepp, A. F. *Inorg. Chem.* **2003,** *42,* 7713–7715. doi:10.1021/ic034802h
18. Panthani, M. G.; Akhavan, V.; Goodfellow, B.; Schmidtke, J. P.; Dunn, L.; Dodabalapur, A.; Barbara, P. F.; Korgel, B. A. *J. Am. Chem. Soc.* **2008,** *130,* 16770–16777. doi:10.1021/ja805845q
19. Basol, B. M.; Kapur, V. K.; Leidholm, C. R.; Halani, A.; Gledhill, K. *Sol. Energy Mater. Sol. Cells* **1996,** *43,* 93–98. doi:10.1016/0927-0248(95)00171-9
20. Zhang, Z.; Liu, R.; Zhao, M.; Qian, Y. *Mater. Chem. Phys.* **2001,** *71,* 161–164. doi:10.1016/S0254-0584(01)00277-2
21. Pashchanka, M.; Hoffmann, R. C.; Gurlo, A.; Schneider, J. J. *J. Mater. Chem.* **2010,** *20,* 8311–8319. doi:10.1039/c0jm01490g
22. Tanino, H.; Fujikake, H.; Maeda, T.; Nakanishi, H. *J. Appl. Phys.* **1993,** *74,* 2114–2116. doi:10.1063/1.354735

23. Ramdani, O.; Guillemoles, J. F.; Lincot, D.; Grand, P. P.; Chassaing, E.; Kerrec, O.; Rzepka, E. *Thin Solid Films* **2007,** *515,* 5909–5912. doi:10.1016/j.tsf.2007.02.109
24. Tanino, H.; Maeda, T.; Fujikake, H.; Nakanishi, H.; Endo, S.; Irie, T. *Phys. Rev. B* **1992,** *45,* 13323–13330. doi:10.1103/PhysRevB.45.13323
25. Chen, H.; Yu, S.-M.; Shin, D.-W.; Yoo, J.-B. *Nanoscale Res. Lett.* **2009,** *5,* 217–223. doi:10.1007/s11671-009-9468-6
26. Kang, F.; Ao, J. P.; Sun, G. Z.; He, Q.; Sun, Y. *Mater. Chem. Phys.* **2009,** *115,* 516–520. doi:10.1016/j.matchemphys.2009.02.006
27. Fan, P.; Liang, G.-X.; Cai, X.-M.; Zheng, Z.-H.; Zhang, D.-P. *Thin Solid Films* **2011,** *519,* 5348–5352. doi:10.1016/j.tsf.2011.02.036
28. Rincón, C.; Ramírez, F. J. *J. Appl. Phys.* **1992,** *72,* 4321–4324. doi:10.1063/1.352195
29. Deepa, K. G.; Vijayakumar, K. P.; Sudhakartha, C. *Mater. Sci. Semicond. Process.* **2012,** *15,* 120–124. doi:10.1016/j.mssp.2011.07.005
30. Zhou, W.; Yin, Z.; Sim, D. H.; Zhang, H.; Ma, J.; Hng, H. H.; Yan, Q. *Nanotechnology* **2011,** *22,* 195607. doi:10.1088/0957-4484/22/19/195607
31. Shen, F.; Que, W.; Zhong, P.; Zhang, J.; Yin, X. *Colloids Surf., A* **2011,** *392,* 1–6. doi:10.1016/j.colsurfa.2011.08.020

License and Terms

The definitive version of this article is the electronic one which can be found at:
doi:10.3762/bjnano.4.98